DETERMINATION OF THE INTERFACIAL HEAT TRANSFER COEFFICIENT IN HOT STAMPING OF ALUMINIUM ALLOYS

By

Xiaochuan Liu

Department of Mechanical Engineering

South Kensington Campus

Imperial College London

London SW7 2AZ

U. K.

A thesis submitted for the degree of Doctor of Philosophy of Imperial College London

2019

Declaration of originality

I declare that this thesis has been composed solely by myself and that it has not been submitted, in whole or in part, in any previous application for a degree. Except where stated otherwise by reference or acknowledgement, the work presented is entirely my own.

Xiaochuan Liu

October 2019

Copyright declaration

Acknowledgements

First and foremost, I would like to express my sincerest gratitude to my supervisor Dr Liliang Wang, who has been supported and encouraged me with patient, enthusiasm, motivation and immense knowledge for many years. My sincere thank also goes to my second supervisor Prof. Jianguo Lin for guiding me to reach more achievements and encouraging me to insist on my work and goals.

My sincere appreciation also goes to Dr Omer El Fakir for teaching me sufficient valuable knowledge and skills. I would not reach such achievement without you. Meanwhile, it is my great pleasure and fortune to receive much kindly help from my brotherhood F4. As F4 saying goes, ‘Ren Sheng Wu Chang, Ji Shi Xing Le’, which means Don’t worry, Be happy.

I would also like to thank the support by the China Scholarship Council (Grant CSC no. 201608060261): A non-profit institution enabling talented Chinese students to undertake a PhD programme overseas. Much appreciated is the strong support received from the CRRC Qingdao Sifang Co., Ltd (CRRC Sifang) to perform my research at the CRRC Sifang Centre for Rail Transportation Manufacturing Technologies at Imperial College London.

Last but not the least, I appreciate my parents and my wife for your consistent support, encourage and trust without complaint or regret. The higher achievement will be reached under your witness. You are always my eternal source of power!

This article is dedicated to my dear wife Jiayi Qu and daughter Fuer Liu.

谨以此文献与我挚爱的妻子曲佳祎和女儿刘芙儿。

Xiaochuan Liu

October 2019

Abstract

The characteristic properties of aluminium alloys, e.g. their high strength-weight ratio, high thermal conductance, excellent corrosion resistance and good recyclability, render them ideal materials to reduce air pollution and improve the fuel economy of vehicles. However, their low formability at room temperature limits their application in industry. In recent years, hot stamping was developed as a promising technology to form sheet metal components from aluminium alloys at elevated temperatures to increase their formability.

The interfacial heat transfer coefficient (IHTC), an essential thermophysical parameter in hot stamping processes, should therefore be identified not only to retain the full mechanical strength of the formed components by achieving the critical quenching rates for different aluminium alloys, but also to optimise the production rate by controlling the quenching process.

The present research aims to determine the IHTC values for 7075 and 6082 aluminium alloys under different experimental conditions. A dedicated IHTC test facility, IHTC-mate, was developed to precisely measure the temperature evolutions of the specimens and thus accurately determine their IHTC values with high stability and repeatability. Subsequently, the effects of the contact pressure, tool material, coating material, specimen thickness, lubricant and initial blank temperature on the IHTC were identified. It was found that the IHTC increased logarithmically with increasing contact pressure. In addition, the applications of tools, coatings and lubricants with higher thermal conductivities, as well as specimens with larger thickness and higher initial blank temperature could raise the IHTC values. Furthermore, a mechanism-based IHTC model was developed to predict the IHTC evolutions as a function of those influential factors, and enable the interaction between the IHTC evolutions and lubricant layer thickness diminution with sliding distance at different contact pressures and sliding speeds.

Hemispherical dome and B-pillar forming tests were conducted to form 7075 and 6082 aluminium alloys. The good agreements between the experimental and simulated temperature evolutions of the components being formed validated the determined IHTC results and developed IHTC model. Consequently, the temperature evolutions and cooling rates of the components being formed in hot stamping processes could be predicted. Furthermore, the processing window and tool design could be optimised to achieve the critical cooling rates and thus retain the full mechanical strength of the formed components.

Nomenclature

Mathematical symbols are listed in alphabetical order

English alphabet

A	Contact area (mm^2)
A_0	Material Coefficient
C	Model coefficient
C_f	Constriction parameter correction factor
D	Model coefficient
E	Model coefficient
F	Model coefficient
H	Hardness of the specimen (HV)
$H^{'}$	Effective hardness of the coated substrate (HV)
K_{st}	Harmonic mean thermal conductivity of two contact mediums (kW/mK)
K_{slt}	Harmonic mean thermal conductivity of three contact mediums (kW/mK)
N_P	Pressure-dependent parameter
$N_\delta(t)$	Instantaneous lubricant thickness-dependent parameter
P	Contact pressure (MPa)
$Q^{t}{}_{s}$	Instantaneous heat flux of specimen (W/m^2)
$Q^{t}{}_{t}$	Instantaneous heat flux of tool (W/m^2)
$\overline{Q}^{t}$	Instantaneous average heat flux (W/m^2)
Q_φ	Activation energy of φ (J/mol)
Q_σ	Activation energy of σ_U (J/mol)

R	Molar gas constant (J/molK)
R_s	Average surface roughness of specimen (nm)
R_t	Average surface roughness of tool (nm)
R_{st}	Root mean square of surface roughness of two contact solids (nm)
T^{t}_{s}	Instantaneous temperature of specimen (˚C)
T^{t}_{t}	Instantaneous temperature of tool (˚C)

b	Model parameter
c	Heat capacity (J/K)
h	Overall IHTC (kW/m^{2}K)
h^t	Instantaneous IHTC (kW/m^{2}K)
h_a	Air-contact IHTC (kW/m^{2}K)
h_c	Coating-contact IHTC (kW/m^{2}K)
h_l	Lubricant-contact IHTC (kW/m^{2}K)
h_s	Solid-contact IHTC (kW/m^{2}K)
k_c	Thermal conductivity of coating (kW/mK)
k_l	Thermal conductivity of lubricant (kW/mK)
k_s	Thermal conductivities of specimen (kW/mK)
k_t	Thermal conductivities of tool (kW/mK)
m	Model parameter
m_0	Material Coefficient
n	Model parameter
n_0	Material Coefficient

t	Time (s)
v	Sliding speed (mm/s)

Greek alphabet

α_l	Specimen thickness-dependent parameter
β	Model parameter
γ	Model parameter
δ_c	Coating thickness (μm)
δ_l	Lubricant thickness (μm)
$\delta_l(t)$	Instantaneous lubricant layer thickness (μm)
δ_0	Initial lubricant layer thickness (μm)
$\varphi(T)$	Temperature-dependent parameter
φ_0	Pre-exponential factor of the temperature-dependent parameter
η	Lubricant viscosity (mm^2/s)
θ	Model parameter
ϑ	Mean of the absolute slope of the surface profile
λ_1	Model parameter
λ_2	Model parameter
ρ	Density (kg/m^3)
σ	Standard deviation of the profile heights
σ_0	Pre-exponential factor of σ_U (MPa)
$\sigma_U(T)$	Ultimate strength of specimen at elevated temperatures (MPa)
ω	Model parameter

Contents

Figure list

Table list

Publication list

Journal articles :

Liu, X., Fakir, O. El, Zheng, Y., Gharbi, M. M., Wang, L., 2019. Effect of tool coatings on the interfacial heat transfer coefficient in hot stamping of aluminium alloys under variable contact pressure conditions. Int. Heat Mass Tranf. 137, 74–83.

Liu, X., Fakir, O. El, Cai, Z., Gharbi, M. M., Dalkaya, B., Wang, L., 2019. Development of an interfacial heat transfer coefficient model for the hot and warm aluminium stamping processes under different initial blank temperature conditions. J. Mater. Process. Technol. 273, 116245.

Liu, X., Fakir, O. El, Meng, L., Sun, X., Li, X., Wang, L., 2018. Effects of lubricant on the IHTC during the hot stamping of AA6082 aluminium alloy: experimental and modelling studies. J. Mater. Process. Technol. 255, 175–183. doi:10.1016/j.jmatprotec.2017.12.013

Liu, X., Ji, K., Fakir, O. El, Fang, H., Gharbi, M. M., Wang, L., 2017. Determination of interfacial heat transfer coefficient for a hot aluminium stamping process. J. Mater. Process. Technol. 247, 158–170. doi:10.1016/j.jmatprotec.2017.04.005

Ji, K., **Liu, X.**, Fakir, O. El, Liu, J., Zhang, Q., Wang, L., 2016. Determination of the interfacial heat transfer coefficient in the hot stamping of AA7075. Manuf. Rev. 3, 16. doi:10.1051/mfreview/2016017

Conference articles:

Liu, X., Zheng, Y., Fakir, O. El, Said, R., Wang, L., 2018. Characterisation of the contact pressure dependent interfacial heat transfer coefficient for a hot stamping process following a data driven approach, in: 4th International Conference on New Forming Technology (ICNFT 2018) doi.org/10.1051/matecconf/201819008005

Liu, X., Fakir, O. El, Gharbi,. M. M., Wang, L., 2018. Effect of tool coating on interfacial heat transfer coefficient in hot stamping of AA7075 aluminium alloys. Procedia Manuf. 15, 1127-1133. doi:10.1016/j.promfg.2018.07.378

Liu, X., Gharbi, M.M., Manassib, O., El, O., Wang, L., 2017. Determination of the interfacial heat transfer coefficient between AA7075 and different forming tools in hot stamping processes. Procedia Eng. 0, 17–22. doi:10.1016/j.proeng.2017.10.818

Liu, X., Ji, K., Fakir, O. El, Liu, J., Zhang, Q., Wang, L., 2015. Determination of the interfacial heat transfer coefficient in the hot stamping of AA7075, in: 4th International Conference on New Forming Technology (ICNFT 2015). doi:10.1051/matecconf/20152105003

Fakir, O. El, Wang, A., Zhang, Q., **Liu, X.**, Liu, J., Wang, L., 2018. Multi-objective sheet metal forming simulations using a software agnostic platform. IOP Conf. Ser. Mater. Sci. Eng. 418, 012122. doi:10.1088/1757-899X/418/1/012122

Zheng, Y., Wang, A., **Liu, X.**, Ji, K., Wang, L., Rajab, S., Knowledge based cloud FE simulation: data-driven material characterization guidelines for hot stamping of aluminium alloys, in: China Society for Technology of Plasticity 2017.

Liu, J., Wang, A., Zheng, Y., **Liu, X.,** Gandra, J., Beamish, K., 2017. Hot stamping of AA6082 tailor welded blanks for automotive applications. Procedia Eng. 0, 17–22. doi:10.1016/j.proeng.2017.10.820

Luan, X., **Liu, X.**, Fang, H., Ji, K., Fakir, O. El, 2016. Characterization of the interfacial heat transfer coefficient for hot stamping processes, in: Journal of Physics Conference Series. p. 734(3)032079. doi:10.1088/1742-6596/734/3/032079

Zhang, Q., Ji, K., Fakir, O. El, **Liu, X.**, Wang, L., 2016. Determination of processing windows for the hot stamping of AA7075, in: 16th International Conference Metal Forming 2016. p. (716)402-412. doi:10.4028/www.scientific.net/KEM.716.402

Patents:

Cai, Z., **Liu, X.**, Dhawan, D., Fakir, O. El, Wang, L., Lin, J., 2019. A compact automatic simulating facility for non-isothermal forming processes. *Filed.*

Wang, L., Sun, Y., Ji, K., Luan, X., Fakir, O. El, Cai, Z., **Liu, X.**, 2017. Fast warm stamping of ultra-high strength steel sheets. *Filed.*

Industrial project reports:

El Fakir, O., **Liu, X.**, Wang, L., 2015. Hot stamping of high strength aluminium panel components with complex structures – Stage I. Report No: CRRC-Sifang-2015-12-23-FAKIR-LIU. *Confidential.*

El Fakir, O., **Liu, X.**, Wang, L., 2016. Hot stamping of high strength aluminium panel components with complex structures – Stage II. Report No: CRRC-Sifang-2016-08-15-FAKIR-LIU. *Confidential.*

El Fakir, O., **Liu, X.**, Wang, L., 2017. Hot stamping of high strength aluminium panel components with complex structures – Final report. Report No: CRRC-Sifang-2017-12-18-FAKIR-LIU. *Confidential.*

Chapter 1

Introduction

1.1 Background

The demand for light-weight materials to improve vehicle fuel economy and reduce air pollution has been rapidly growing in recent years [1]. In 2010, materials used most commonly in major vehicle structural components were mild steels and high-strength low-alloy steels (HSLA), followed by high strength steels, aluminium alloys, composites, boron steels and advanced high strength steels, as shown in Fig. 1.1 [2]. The usage of mild steels is predicted to decrease from its value of 55% of a vehicle structure in 2010 to 5% in 2040, while that of high strength low alloys is set to decrease during this period as well. In contrast, the usage of aluminium alloys (AL 5000/6000 plus Aluminium/High Strength) will increase rapidly from 4% in 2010 to 25% in 2040. The characteristic properties of aluminium alloys, e.g. their high strength to weight ratio, high thermal conductivity, excellent corrosion resistance and good recyclability, render them ideal materials in vehicles in the upcoming twenty years. Furthermore, it was estimated that a vehicle structure made of aluminium alloys could save approximately 9% of carbon dioxide (CO_2) emissions over the lifetime of the vehicle compared to steel, as shown in Fig. 1.2 [3]. Among aluminium alloys, 6xxx series, e.g. AA6082, have been widely used in vehicles. In order to meet higher expectation on the mechanical strength of structural components, the application of 7xxx aluminium alloys, e.g. AA7075, is being studied as a potential solution. Therefore, 6xxx and 7xxx series are currently of great interest to industry.

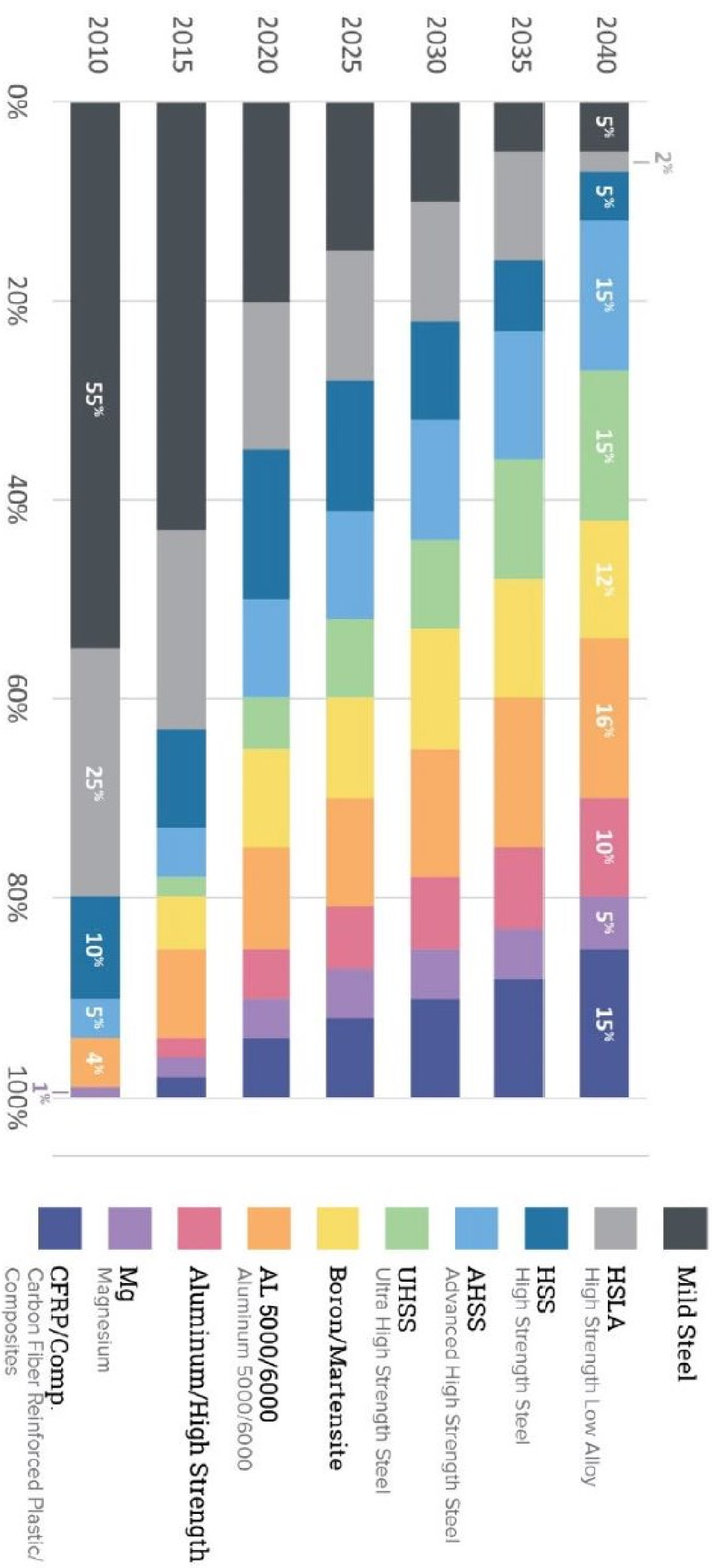

Fig. 1.1. Materials distribution in vehicles from 2010 to 2040 [2].

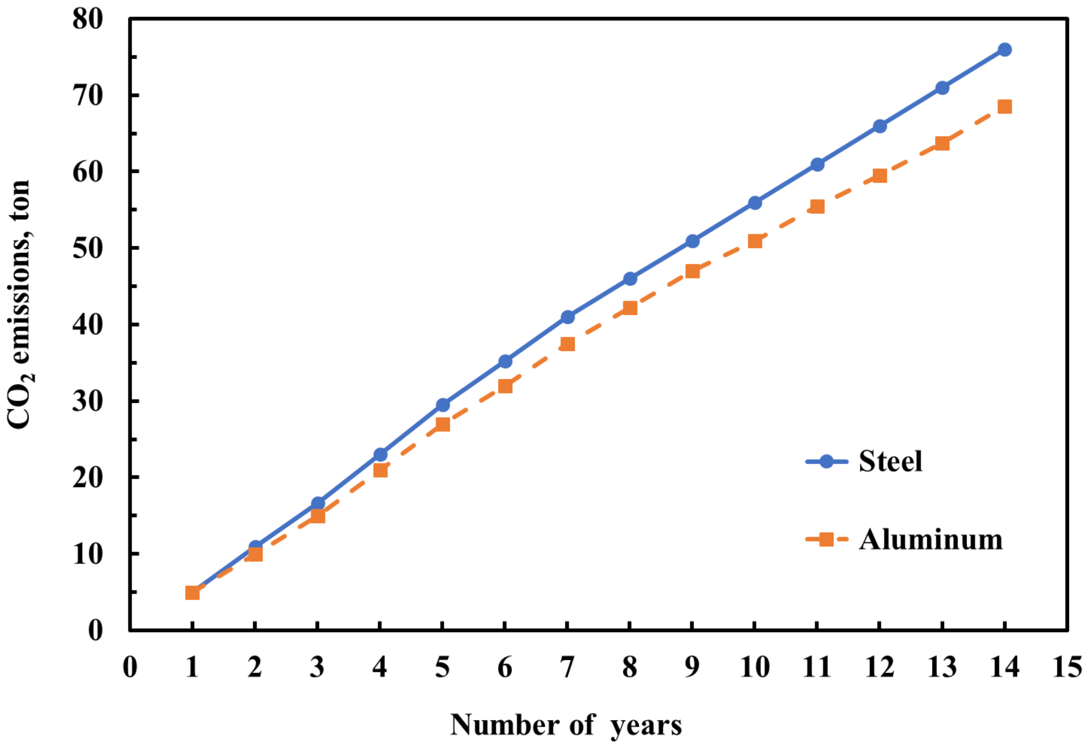

Fig. 1.2. Carbon dioxide emissions over the lifetime of a vehicle [3].

Components with relatively simple shapes, e.g. roofs and hoods shown in Fig. 1.3 [2], can be formed under room temperature conditions. However, the forming of components with complex shapes, e.g. door inners and A-pillars, requires a high formability of the material, which cannot be achieved at room temperature. In order to increase the formability of aluminium alloys, hot aluminium stamping was developed to form sheet aluminium components at elevated temperatures. Generally, a sheet metal blank is firstly heated up to an elevated temperature, and then formed and quenched simultaneously by cold dies at a high forming speed to obtain a supersaturated solid solution (SSSS), which provides a high post-form strength after an artificial ageing process [4]. In order to attain the desirable SSSS state, the quenching rate during the hot stamping process must be above the critical cooling rate such that no solute elements precipitate out as coarse particles [5]. Various elevated temperatures, either lower or higher than the solution heat treatment (SHT) temperature of the material, were used in the hot stamping to meet different requirements [6]–[8]. Fig. 1.4 shows the schematic process of a promising hot stamping technology, i.e. solution heat treatment, forming and in-die quenching (HFQ[1]) [9], in which the material has to be heated up to its SHT temperature. In contrast, the warm stamping applied an elevated temperature around 300˚C, which was much

---

[1] HFQ® is a registered trademark of Impression Technologies Ltd.

lower than that in the hot stamping [10]–[12], while the forging applied an extremely high temperature around 1000˚C, which was significantly higher than that in the hot stamping, to deform high-strength steels and titanium alloys [13]–[15]. Forming tools had to be heated as well prior to forming in both warm stamping and forging. By comparison, hot stamping technology is beneficial for saving fuel consumption and increasing tool life as a result of maintaining the forming tools at room temperature. In such a non-isothermal hot stamping process, the prediction of the heat transfer and temperature field is prerequisite to the accurate simulation results.

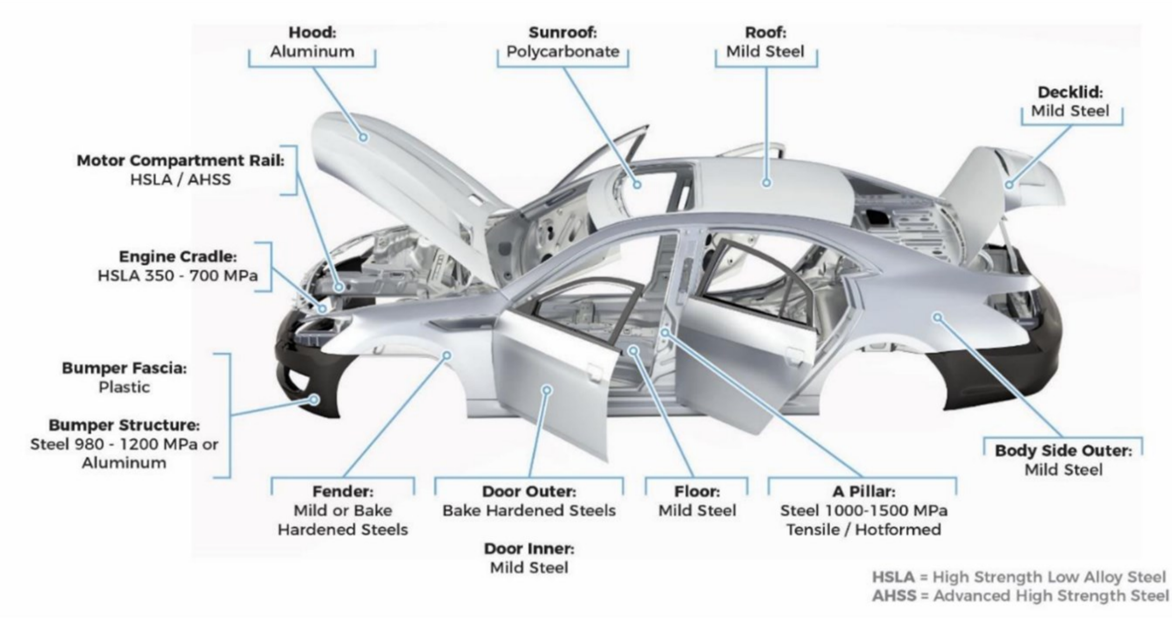

Fig. 1.3. Major vehicle structural components [2].

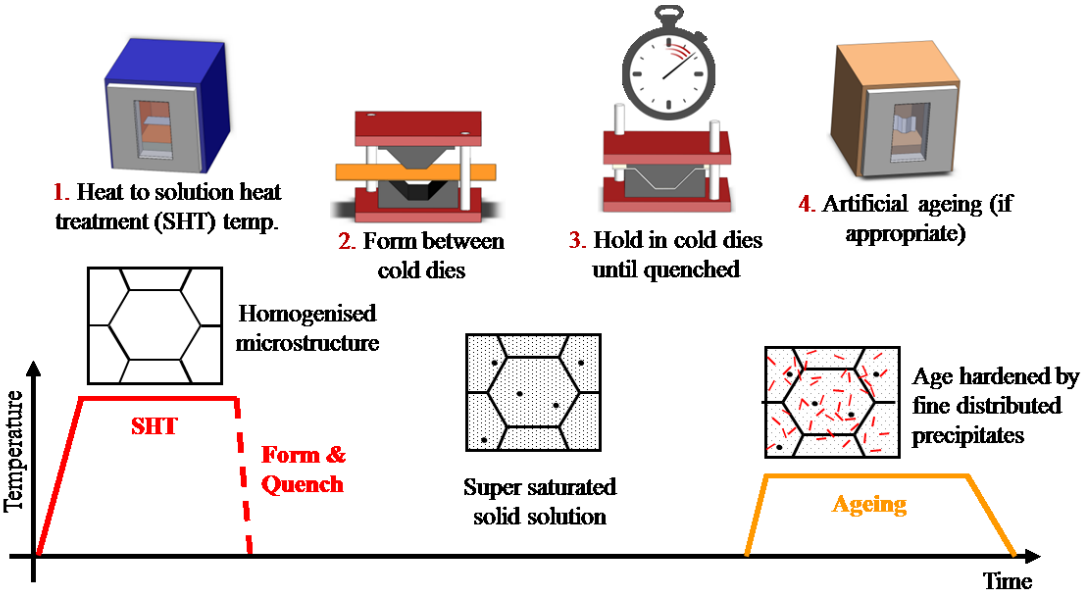

Fig. 1.4. Schematic diagram of the HFQ forming process [9].

Three fundamental modes of heat transfer, i.e. heat conduction, heat convection and radiation, determine the temperature field in a non-isothermal forming process [16], as shown in Fig. 1.5. Heat conduction is the transfer of heat within an object, either a hot blank or cold die, and evaluated by the thermal conductivity of the material. Heat convection is the transfer of heat from a hot blank to cold dies and dependent on the heat transfer coefficient, which describes the thermodynamic driving force for the flow of heat between the hot blank and cold dies. Due to heat convection occurring at the contact interface, the heat transfer coefficient is also named as the interfacial heat transfer coefficient (IHTC) in hot stamping processes [17]. In contrast, radiation is a mode of heat transfer that does not rely on any contact but determined by the emissivity of the material. Heat convection dominates the heat transfer in the hot stamping as a result of a large temperature gradient between a hot blank sheet and cold dies.

Therefore, the heat transfer coefficient at the contact interface, i.e. the IHTC, is an essential thermophysical parameter to determine the temperature field in a non-isothermal metal forming process. Two mature methods were typically used to determine the IHTC: the inverse heat conduction method , in which the temperature evolutions of the specimens were measured and then compared with those inversely calculated with Beck’s non-linear estimation method, or with those predicted by formulations using a 1D closed-form method or the inverse FE simulation method, in which FE simulations were applied to obtain the simulated temperature evolutions as a function of time to fit the experimental curves to identify the corresponding IHTC values. More details were introduced in Chapter 2.

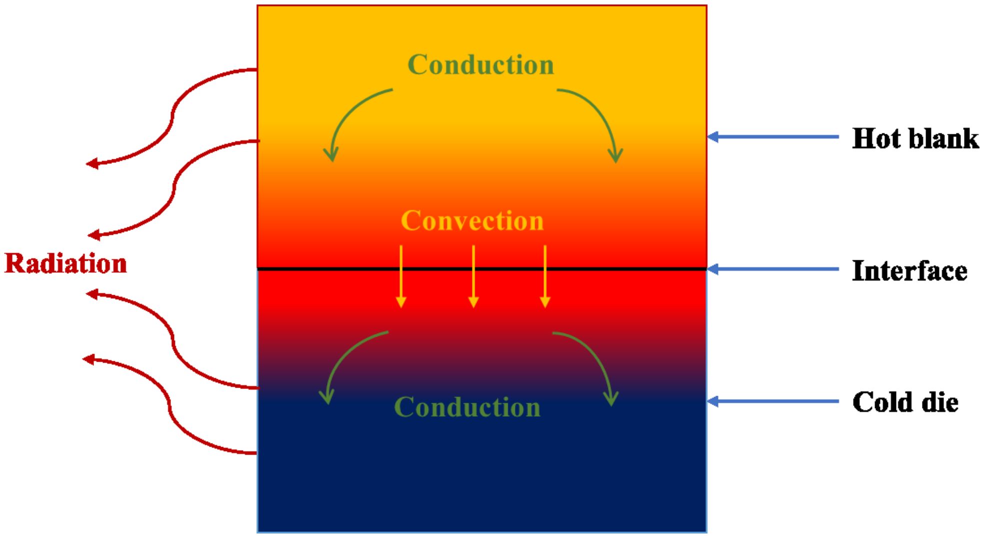

Fig. 1.5. Schematic diagram for three modes of heat transfer.

After simulating the temperature field, the temperature evolutions of all elements on the formed components can be obtained and then compared with the continuous cooling precipitation

(CCP) diagram of the material. The elements, of which the temperature evolutions do not intersect the CCP diagram, are able to achieve a high post-form strength after artificial ageing, due to the uniform distribution of precipitates; while the elements, of which the temperature evolutions intersect the CCP diagram, fail to retain its full mechanical strength as secondary phase is precipitated out of the aluminium matrix [18]. The critical cooling rate of the material is therefore determined. Fig. 1.6 shows a comparison example between the temperature evolution and CCP diagram of AA6082 to determine the critical cooling rate and thus the post-form strength [19]. Hence, the IHTC is able not only to obtain the temperature field of the formed components in simulations but also to retain the full mechanical strength of formed components by achieving the critical quenching rates for different aluminium alloys. It should be noticed that the critical cooling rate and post-form strength of the materials are of no interest in the present research. Instead, this work identified the IHTC only, which could be used to characterise the critical cooling rate and thus the post-form strength of the material in future work.

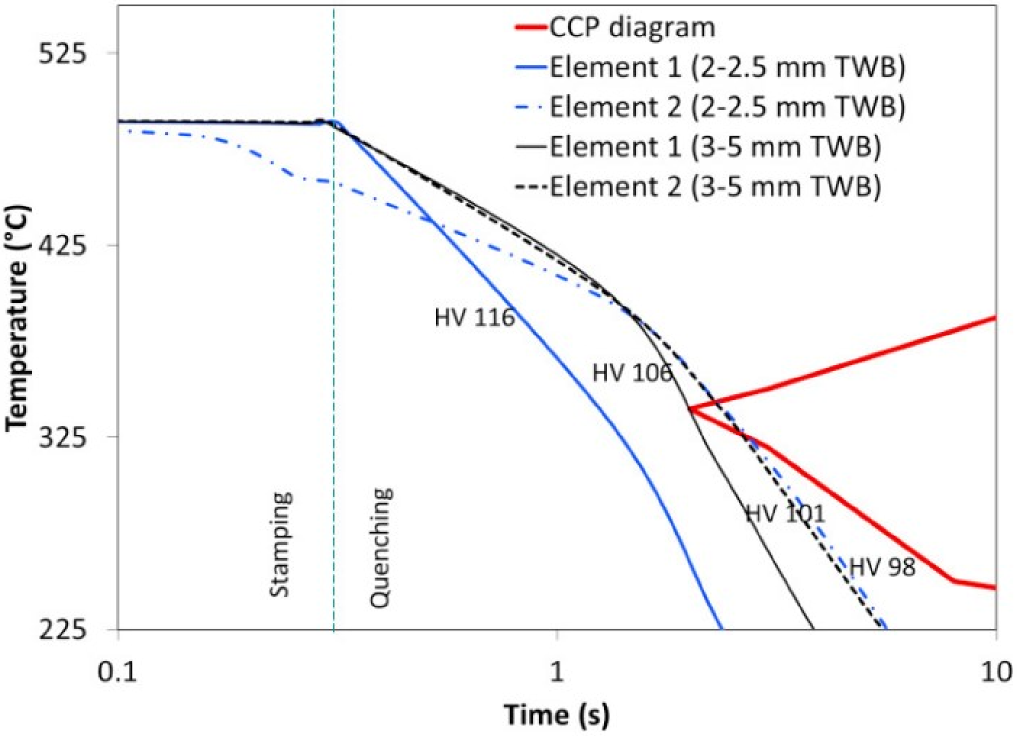

Fig. 1.6. Comparison between the temperature evolutions and CCP diagram of AA6082 [19].

1.2 Aim and objectives

Due to the importance of the IHTC in hot aluminium stamping processes, the present research aims to comprehensively study and determine the IHTC values for 7075 and 6082 aluminium alloys under different experimental conditions, and subsequently identify the key influential factors on the IHTC. These results could then be implemented in FE simulations of forming processes to simulate the temperature evolutions of the components being formed. Furthermore, the processing window and tool design could be optimised to ensure that the critical cooling rate is satisfied during hot stamping processes to achieve the desired post-form mechanical strength. In order to reach this aim, the research objectives were set as follows, and covered in each subsequent chapter:

- A literature review of the methods and equipment to determine the IHTC, the influential factors on the IHTC and the models to predict the IHTC – Chapter 2
- Development of a dedicated IHTC test facility to precisely measure the temperature evolutions of the aluminium specimens and thus accurately determine their IHTC values under different experimental conditions– Chapter 3
- Determination of the IHTC values for aluminium alloys under different experimental conditions, and the identification of the effects of the contact pressure, tool material, coating material, specimen thickness, lubricant and initial blank temperature on the IHTC – Chapter 4
- Development of a general mechanism-based IHTC model to predict the IHTC evolutions as a function of the contact pressure, tool material, coating material, specimen thickness, lubricant and initial blank temperature- Chapter 5
- Case studies of the application of the IHTC model into the hot stamping processes to validate the determined IHTC results and developed IHTC model – Chapter 6
- Conclusions of the research findings, key contributions, and proposals for future work – Chapter 7

Chapter 2

Literature review on the IHTC[2]

In Chapter 2, the methods and test facilities applied in previous research to determine the IHTC are reviewed. The main influential factors on the IHTC, e.g. contact pressure, tool material, coating material, specimen thickness, lubricant and initial blank temperature, were investigated, in addition to efforts made to develop the models to predict the IHTC.

2.1 Methods to determine the IHTC

In order to identify the IHTC under specific experimental conditions, two mature methods were typically used: the inverse heat conduction method , in which the temperature evolutions of the specimens were measured and then compared with those inversely calculated with Beck's non-linear estimation method [20]–[24], or with those predicted by formulations using a 1D closed-form method [25]–[27] or the inverse FE simulation method [28]–[31], in which FE simulations were applied to obtain the simulated temperature evolutions as a function of time to fit the experimental curves to identify the corresponding IHTC values.

---

[2] Chapter 2 was reproduced from two papers:

Liu, X., Gharbi, M.M., Manassib, O., El, O., Wang, L., 2017. Determination of the interfacial heat transfer coefficient between AA7075 and different forming tools in hot stamping processes. Procedia Eng. 0, 17–22. doi:10.1016/j.proeng.2017.10.818

Liu, X., Ji, K., Fakir, O. El, Liu, J., Zhang, Q., Wang, L., 2015. Determination of the interfacial heat transfer coefficient in the hot stamping of AA7075, in: 4th International Conference on New Forming Technology (ICNFT 2015). doi:10.1051/matecconf/20152105003

Specifically, the inverse heat conduction method was applied in Bai et al.'s study [25] to determine the IHTC values by comparing the experimental temperature evolutions of the specimen and tool at different locations with those calculated by the 1D closed-form method. The instantaneous IHTC was calculated by Newton's law of cooling, as shown in Eq. (2.1):

$$h^t = \overline{Q}^t / (T^t{}_{w,1} - T^t{}_{d,1}) \tag{2.1}$$

where $\overline{Q}^t$ is the instantaneous average heat flux, and $T^t{}_{w,1}$ and $T^t{}_{d,1}$ are the instantaneous temperatures of the specimen and tool at their contact surfaces respectively, which could be determined by the differential form of Fourier's law of thermal conduction, when assuming the heat transfer between the specimen and tool as a one-dimensional problem, as shown in Eqs. (2.2) and (2.3):

$$\frac{\partial T^t{}_w}{\partial t} = \frac{k_w}{\rho_w c_w}\left(\frac{\partial^2 T^t{}_w}{\partial^2 x_w}\right) \tag{2.2}$$

$$\frac{\partial T^t{}_d}{\partial t} = \frac{k_d}{\rho_d c_d}\left(\frac{\partial^2 T^t{}_d}{\partial^2 x_d}\right) \tag{2.3}$$

where k is the thermal conductivity, ρ is the density, c is the specific heat capacity and x is the location. The subscripts w and d indicate the properties of the specimen (workpiece) and tool (die) respectively. Fig. 2.1 shows a simplified 1D heat transfer finite difference model for the specimen and tool.

The heat fluxes at the contact surfaces of the specimen and tool could therefore be determined by solving those partial differential equations with a convergent time increment of 0.0001 seconds, which are shown in Eqs. (2.4) and (2.5) respectively:

$$Q^t{}_w = k_w (T^t{}_{w,1} - T^t{}_{w,2}) / \Delta x_w \tag{2.4}$$

$$Q^t{}_d = k_d (T^t{}_{d,1} - T^t{}_{d,2}) / \Delta x_d \tag{2.5}$$

where $T^t{}_{w,2}$ and $T^t{}_{d,2}$ are the temperatures of the specimen and tool at the locations, where $x_{s,2} = x_{s,1} + \Delta x_s$ and $x_{d,2} = x_{d,1} + \Delta x_d$ respectively. Δx_s is 4 mm, while Δx_d is 1.6 mm. Subsequently, the average heat flux $\overline{Q}^t$, describing the heat flow rate intensity at the contact interface shown in Eq. (2.6), was substituted in Eq. (2.1) to calculate the instantaneous IHTC h^t, whose average value was considered as the overall IHTC value. The IHTC evolution has to be applied in the FE simulation as a function of contact pressure only, instead of time or temperature. Therefore, the average value of the IHTC had to be calculated and used to represent a particular test condition.

$$\overline{Q}^t = \frac{1}{2}(Q^t_w + Q^t_d) \tag{2.6}$$

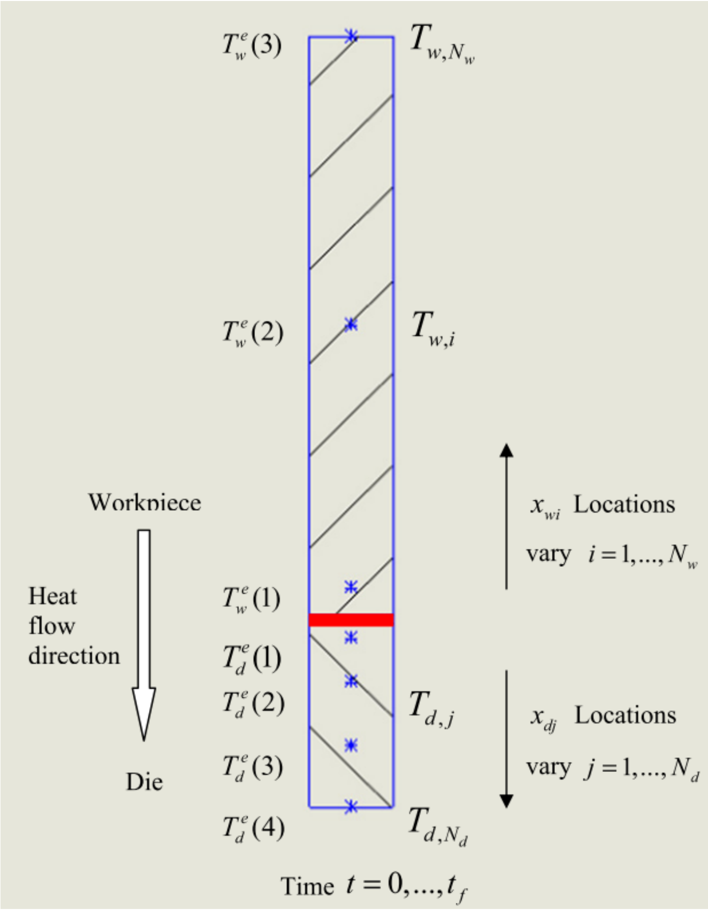

Fig. 2.1. Simplified 1D heat transfer finite difference for the specimen and tool.

The inverse FE simulation method was applied to determine the IHTC in the study of Yukawa et al. [30], in which the simulated temperature evolutions of the punch were obtained by implementing constant IHTC values in DEFORM-2D and then compared with the experimental temperature curves under different conditions. As shown in Fig. 2.2, the simulated temperature evolution of the punch at an IHTC value of 10 kW/m^{2}K was considered to have the best agreement with the experimental results at a contact pressure of 250 MPa, indicating that the IHTC value for the mild steel was 10 kW/m^{2}K when the contact pressure was 250 MPa. However, the experimental temperature evolution showed a better agreement with the simulated curve at an IHTC value of 8 kW/m^{2}K at the first two seconds. This indicated that the inverse FE simulation method requires a reliable test facility to precisely measure the temperature evolutions, leading to an accurate comparison result.

Both methods have been applied in the determination of the IHTC in the hot forging and stamping processes. The inverse heat conduction method requires precise measurements of the temperature evolutions of the specimen and tool at different locations to enable the calculation of the IHTC under one-dimensional heat transfer conditions. In contrast, the inverse FE simulation method does not necessitate significant experimental efforts. Furthermore, it is able to calculate the IHTC under three-dimensional heat transfer conditions, representing the overall heat transfer coefficient at the contact interface. Therefore, the inverse FE simulation method was applied in the present research to determine the IHTC values by comparing the experimental and simulated temperature evolutions of the specimen. It should be noticed that the experimental temperature evolutions with extremely high accuracy and repeatability are necessary for the inverse FE simulation method.

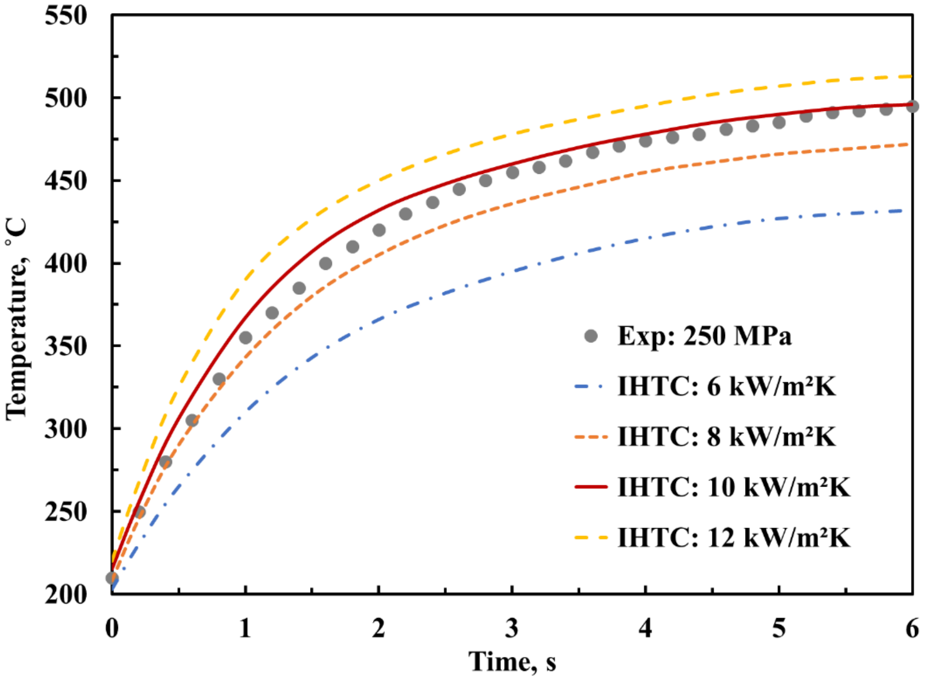

Fig. 2.2. Comparison between the experimental and simulated temperature evolutions of the punch in the study by Yukawa et al. [30].

2.2 IHTC test facilities

In order to determine the IHTC values by using either the inverse heat conduction method or the inverse FE simulation method, measurements of the temperature evolutions of the specimens under different experimental conditions were necessary. Therefore, considerable efforts have been made previously to develop IHTC test facilities to measure the temperature evolutions of specimens.

In Chang et al.'s [23] hot stamping experiments, a medium-Mn steel specimen was firstly heated to the target temperature of 900°C and soaked for 3 minutes in a furnace, and then quickly transferred onto a lower die and compressed by an upper die, which were both made of AISI 1045 tool steel, and their temperature evolutions were recorded, as shown in Fig. 2.3. Only plastic deformation at a microscopic level occurred under the applied test conditions. Similar test facilities were also applied in Caron et al.'s [20] and Zhao et al.'s [31] studies, in which hot specimens were manually transferred from heating furnaces to test facilities before each compression, resulting in decreases in the accuracy and repeatability of the tests. Although different materials and processing parameters were used in previous research, those test facilities were able to measure the temperature evolutions of aluminium alloys as well. However, the same issues on accuracy and repeatability would happen again.

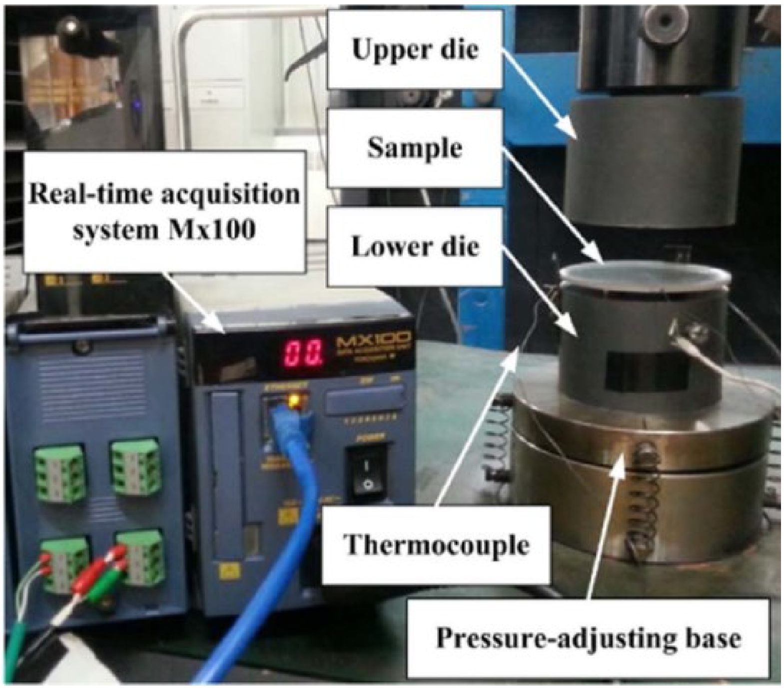

Fig. 2.3. The IHTC test facility developed by Chang et al. [23].

In the study of Bai et al. [25], a Ti-6Al-4V specimen was placed between two dies, which were made of H13 steel, as shown in Fig. 2.4 (a). The specimen was heated in a furnace to the target temperature and then compressed between two dies heated by nozzle band heaters controlled by a temperature control box, while the temperature histories were recorded by pairs of thermocouples embedded in the specimen at different locations, as shown in Fig. 2.4 (b).

However, the experimental temperature evolutions of the specimen oscillated due to unstable contact pressures being applied between the specimen and dies in the initial stages, as shown in Fig. 2.4 (c). Similar oscillations were also found in the experimental temperature evolutions of specimens measured using the IHTC test facilities developed by Mendiguren et al. [32] and Ji et al. [33].

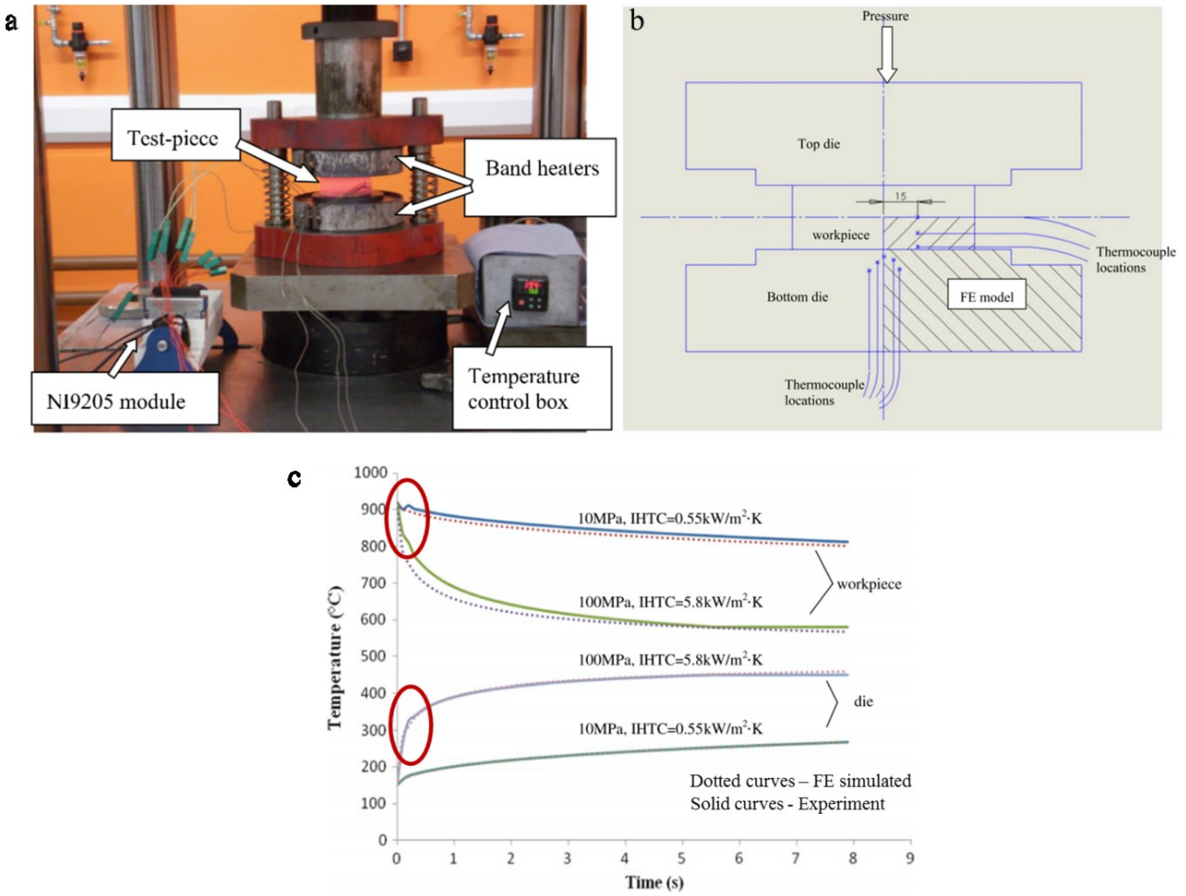

Fig. 2.4. (a) The IHTC test facility developed by Bai et al. [25]; (b) Thermocouple locations; (c) Experimental temperature evolutions of the specimen and die with oscillations in the initial stages.

A vertical-compression equipment was also developed by Yukawa et al. [30], as shown in Fig. 2.5 (a). Once heated to their target temperatures and soaked for different periods of times, the carbon steel specimens (workpiece) were moved onto a heat insulating die and then compressed by a heat conducting punch. The temperature evolutions of the punch and specimen were measured and recorded using thermocouples. Due to its insulating property, the zirconia die could eliminate the temperature loss of the specimen before each compression; however, heat flowed from the specimen to the punch only during compression, leading to asymmetric temperature distribution in the specimen and thus a decrease in the accuracy of the IHTC results.

Furthermore, severe plastic deformation occurred in the centre of the specimen at a high contact pressure due to its contact surface being larger than that of the punch, as shown in Fig. 2.5 (b).

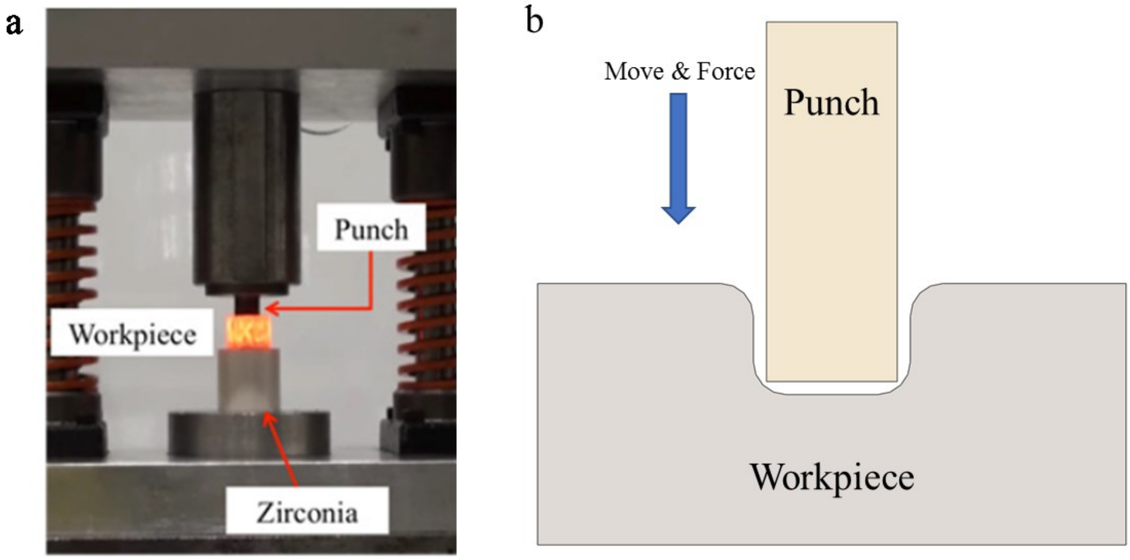

Fig. 2.5. The IHTC test facility developed by Yukawa et al. [30].

Previous research has therefore enabled the characterisation of the IHTC through manual transfer operations under constant contact pressure conditions. However, existing testing equipment faces challenges when ultra-precision control is required to represent the complex nature of a hot stamping process. Therefore, the development of a dedicated IHTC test facility able to precisely apply a contact pressure and measure the temperature evolutions of specimens is of great importance.

2.3 Influential factors on the IHTC

The influential factors on the IHTC, e.g. contact pressure, tool material, coating material, specimen thickness, lubricant and initial blank temperature, have been studied in previous research. As one of the most important effects on the IHTC, the effect of the contact pressure attracted considerable interest. The IHTC for Ti-6Al-4V was observed to increase exponentially from a small value at 0 MPa to 6 kW/m^{2}K at 100 MPa, followed by a plateau of the IHTC at high contact pressures [25], as shown in Fig 2.6 (a). The result of the exponential increasing trend of the IHTC with contact pressure was also found in the study of Yukawa et al. [30] of carbon steel. A different increasing trend of the IHTC evolution with contact pressure was found in the study of Chang et al. [21], in which the IHTC for a 22MnB5 steel increased from 0.3 kW/m^{2}K at 0 MPa to 4.5 kW/m^{2}K at 25 MPa as a power function of contact pressure, as shown in Fig 2.6 (b). In contrast, the IHTC for a Usibor 1500 steel increased linearly from 4.3 kW/m^{2}K at 0 MPa to 7.8 kW/m^{2}K at 25 MPa in the study of Caron et al. [20], as shown in Fig 2.6 (c). The evolution of the real contact area at the interface could explain the increasing trend of the IHTC in previous research, however, which was not proved yet.

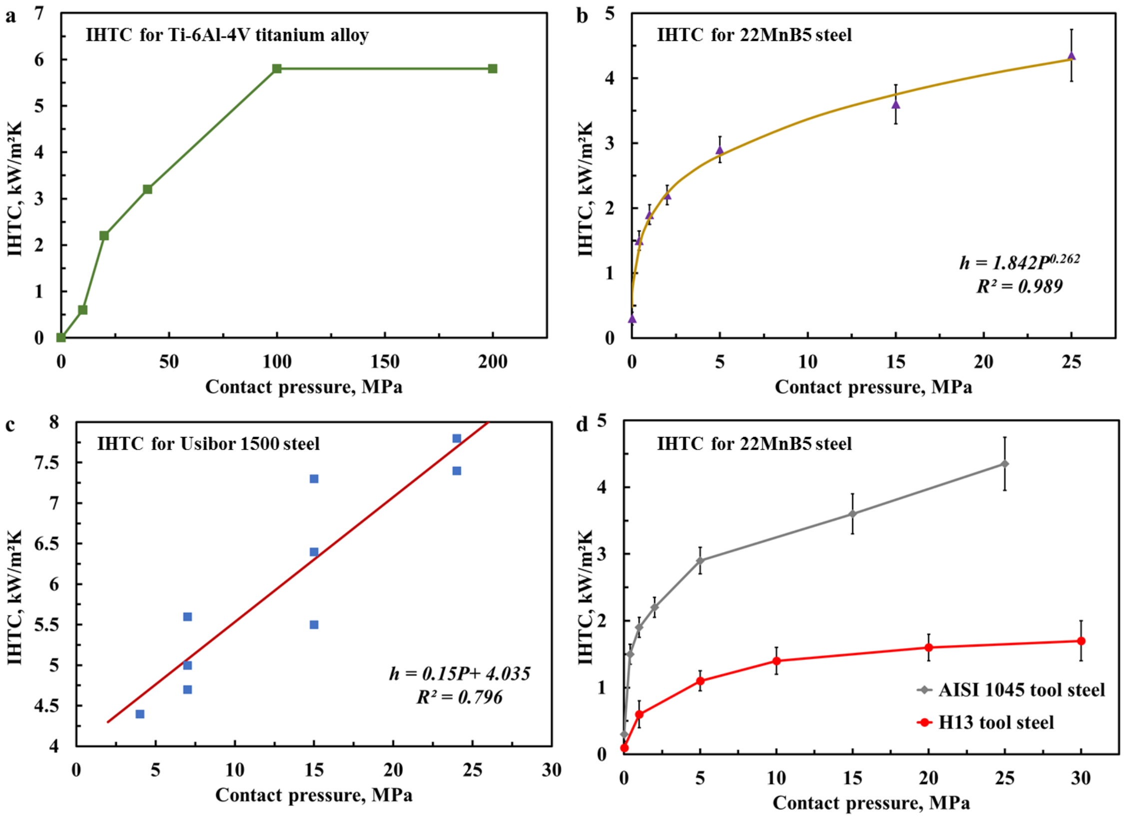

Fig. 2.6. The IHTC evolutions with contact pressure following (a) an exponentially increasing trend [25]; (b) a power increasing trend [21]; (c) a linearly increasing trend [20]; and (d) a power increasing trend when using AISI 1045 and H13 tool steels [21].

Different tool materials are used in the hot stamping processes to meet the desired requirement, and their effects on the IHTC are also required to be studied. The effect of tool material on the IHTC has been characterised in Chang et al.'s [21] study, in which 22MnB5 specimens were compressed by AISI 1045 steel and H13 tool steel respectively. The thermal conductivity of 1045 tool steel is higher than that of H13 tool steel, contributing to higher IHTC values, as shown in Fig 2.6 (d). Hu et al. [34] investigated the IHTC in hot stamping between 22MnB5 specimens and H11 tools, which have a thermal conductivity value and subsequently IHTC values between those of 1045 and H13 tool steels. Hu et al. [35] also found that the peak IHTC value for Ti-6Al-4V using Inconel alloy IN718 tools (2.5 kW/m^{2}K) was less than that when using H13 tools (20 kW/m^{2}K) under the same conditions [25], due to the thermal conductivity of Inconel 718 being much less than that of H13 tool steel.

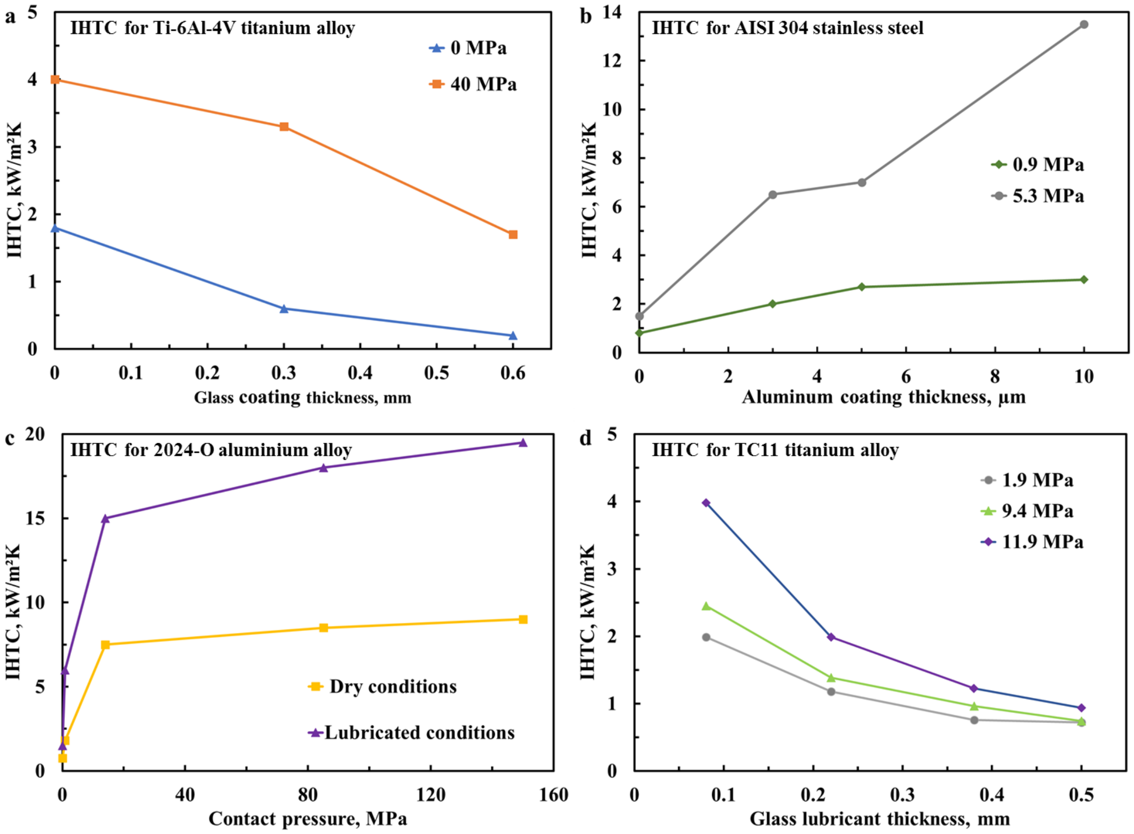

Fig. 2.7. The IHTC evolutions with (a) glass coating thickness [25]; (b) aluminium coating thickness [36]; (c) contact pressure under dry and lubricated conditions [37]; and (d) glass lubricant thickness [38].

Coatings are being widely used in the hot stamping industry due to their excellent wear resistance, friction performance, chemical stability and corrosion resistance [39]. An adverse effect of coatings on the IHTC was identified in Bai et al.'s [25] study, in which the IHTC between a titanium alloy and H13 tool steel decreased from 4 to 1.7 kW/m^{2}K when a glass coating with a low thermal conductivity was applied onto the specimen, as shown in Fig 2.7 (a). However, a positive effect on the IHTC was observed when coatings with high thermal conductivities were applied. Li et al. [36] found that the IHTC values for two different steels were dramatically increased when using four different coating materials, i.e. tin, copper, aluminium and silver, and furthermore the level of the increase was significantly influenced by the coating thickness, as shown in Fig 2.7 (b). Specifically, the IHTC dramatically increased from 1.5 to 13.5 kW/m^{2}K when the aluminium coating thickness increased from 0 to 10 µm at a contact pressure of 5.3 MPa. Aluminium chromium nitride (AlCrN) coatings with high oxidation resistance [40], chromium nitride (CrN) coatings with high plastic deformation resistance and excellent adhesion strength [41], and titanium nitride (TiN) coatings with extremely high hardness and excellent thermal stability [42], are being widely studied in the hot stamping industry as tool coatings, although their effects on the IHTC have yet to be determined.

Blank sheets with different thicknesses were used in the hot stamping industry to fulfil the desired requirements in the post-form strength of the formed components [43]. The effect of specimen thickness on the IHTC was also investigated by Caron et al. [44], who identified that the IHTC tended to increase with increasing specimen thickness at the same contact pressure. However, its mechanism was not identified yet. In addition, lubricants were widely applied in the hot stamping processes to reduce the tool wear [45] and increase the drawability of the material [46]. The effect of the lubricant on the IHTC was investigated in Burte et al.'s [37] study, in which a graphite-in-water suspension was applied as a lubricant between 2024-O aluminium alloy and H13 tool steel. The application of the lubricant raised the IHTC values from 1.8 to 6 kW/m^{2}K at a contact pressure of 0.85 MPa and from 9 to 18 kW/m^{2}K at a contact pressure of 150 MPa, as shown in Fig 2.7 (c). A similar positive effect of lubricant on the IHTC was also observed in the studies of Foster et al. [46] for AA6082 using four different lubricants and of Jain [47] for 1100-O aluminium alloy using MoS$_2$ as a lubricant. However, a negative effect on the IHTC was found in Zhang et al.'s [38] research, in which glass was used as a lubricant between titanium alloy TC11 and superalloy K403, and the IHTC value decreased from 4 to 1 kW/m^{2}K when the lubricant thickness increased from 0.08 to 0.5 mm at a contact pressure of 11.9 MPa, as shown in Fig 2.7 (d). The lubricant filled up the vacancies at the contact interface, and thus its thermal properties affected the heat transfer between the specimen and tools at different levels.

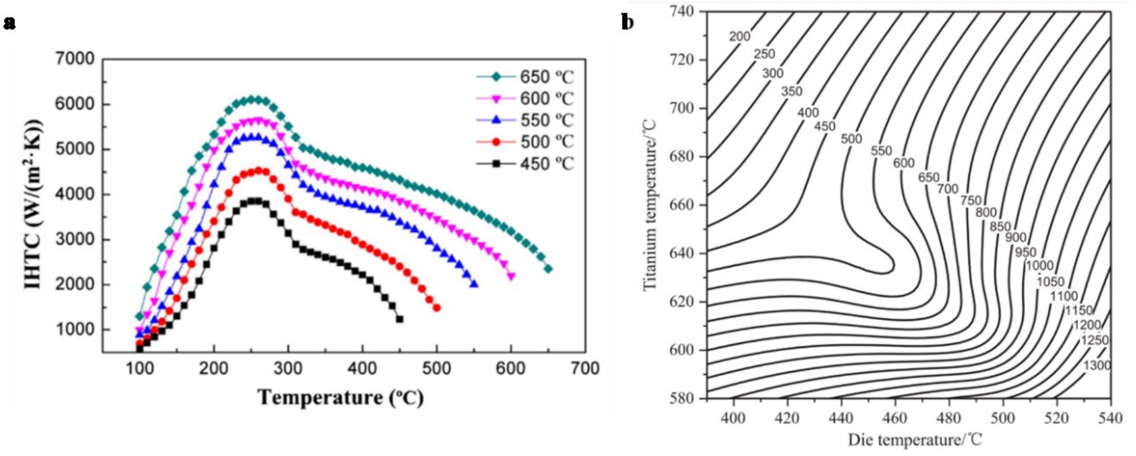

Fig. 2.8. The IHTC evolutions as a function of initial blank temperature for (a) a manganese steel [23]; and (b) a titanium alloy [48].

In the previous research outlined above, the IHTC values were determined at specific initial blank temperatures. However, Chang et al. [23] found that the IHTC for a manganese steel increased with increasing initial blank temperature, as shown in Fig. 2.8 (a). The peak IHTC value increased from approximately 3.6 to 6.2 kW/m^{2}K when the initial blank temperature increased from 450˚C to 650˚C. A similar positive effect was also found in Zhu et al. 's [48] hot forging of a Hastelloy, due to the higher thermal properties of the specimen at higher initial blank temperatures. In contrast, a negative effect of initial blank temperature on the IHTC was identified in Xu et al.'s [49] hot forging of a titanium alloy, in which the IHTC decreased from 0.95 kW/m^{2}K at 580˚C to 0.2 kW/m^{2}K at 720 ˚C when the initial temperature of the die was 400˚C, as shown in Fig. 2.8 (b). This indicated that the IHTC trends determined at a specific initial blank temperature were only accurate under that temperature condition, due to different thermal gradients between the specimen and tools. The identification of the IHTCs for aluminium alloys at different initial blank temperatures is therefore essential for different hot and warm stamping processes.

Based on this previous research, the contact pressure, tool material, coating material, specimen thickness, lubricant and initial blank temperature significantly influence the IHTC, and thus their effects on the IHTC for aluminium alloys are of great importance to be studied. Seldom research stated errors on the determined IHTC values, which will be analysed in the present study.

2.4 IHTC models

In order to predict IHTC values, Çetinkale and Fishenden's [50] equation is widely used to estimate the overall interfacial heat transfer coefficient. As shown in Eq. (2.7), the overall IHTC is a sum of two independent parts, the air-contact IHTC h_a and the solid-contact IHTC h_s, according to different heat transfer mechanisms, as shown in Fig. 2.9.

$$h = h_a + h_s \tag{2.7}$$

Several studies have modelled the solid-contact IHTC h_s. Cooper and Yovanovich [51] identified a theoretical model for the IHTC between the two contacting stainless steel as a power function of contact pressure, as shown in Eq. (2.8):

$$h_s = 1.45 K_{st} \frac{\tan \vartheta}{\sigma} (\frac{P}{H})^{0.985} \tag{2.8}$$

where K_{st} is the mean thermal conductivity of the two contacting solids, ϑ is the mean of the absolute slope of the surface profile, σ is the standard deviation of the profile heights, P is the applied contact pressure and H is the hardness of the specimen. The ratio of the applied contact pressure to the hardness/ultimate strength of the specimen is equivalent to the ratio of the real contact area to the apparent contact area at that contact pressure, representing the deformation mechanism of the asperities on the specimen surface, as shown in Eq. (2.9):

$$P / H = A_r / A_a \tag{2.9}$$

where A_r and A_a are the real contact area and apparent contact area respectively. Meanwhile, this ratio was found to have a linear relationship with the term of $\frac{h_s}{K_{st}} \cdot \frac{\sigma}{\tan \vartheta}$ based on Gaussian distribution. Therefore, the solid-contact IHTC was built up followed by Eq. (2.8) in this study.

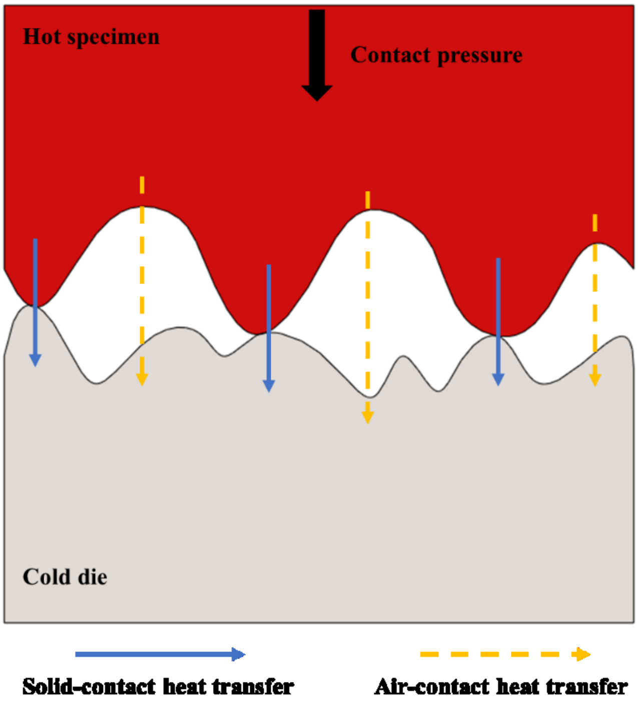

Fig. 2.9. Schematic diagram of the solid-contact and air-contact heat transfer between a hot specimen and cold dies.

As shown in Eq. (2.10), the power relationship between the IHTC and contact pressure was also developed as a semi-empirical dimensionless model by Shlykov et al. [52]:

$$h_s = 8000 K_{st} \left(\frac{P}{C\sigma_U} D\right)^{0.86} \tag{2.10}$$

where σ_U is the ultimate strength of the specimen, and C and D are model coefficients. Considering that the plastic deformation of asperities occurred at a large contact pressure during compression, this model therefore used the ratio of the contact pressure to the ultimate strength of the specimen, instead of the material hardness in Eq. (2.8), to describe the contact pressure mechanism. In addition, the model coefficients in Eq. (2.10) were different from those in Eq. (2.9) due to a cold work-hardened steel being used in this study. This indicated that the model coefficients are material dependent and thus have to be calibrated according to the experimental results.

Differing from the power equations above, an exponential equation for the IHTC as a function of contact pressure was developed by Yukawa et al. [30], as shown in Eq. (2.11):

$$h_s = E[1-\exp(-FP)] \tag{2.11}$$

where E and F are model constants determined by the least square method using the experimental results. As a result of the application of a large contact pressure up to 300 MPa, the peak real contact area was reached in this research, leading to the convergence of the IHTC. Therefore, an exponentially increasing trend of the IHTC was observed. However, this empirical model was not able to describe the mechanisms of the contact pressure and tool materials on the IHTC.

When a coating was applied, the coating-contact IHTC h_c was joint with the solid-contact IHTC h_s, modelled by Antonetti et al. [53] as Eq. (2.12):

$$h_c = h_s(\frac{H}{H^{'}})^{0.93}(\frac{k_t+k_s}{C_f k_t + k_s}) \tag{2.12}$$

where $H^{'}$ is the effective hardness of the coated substrate, C_f is the constriction parameter correction factor, and k_t and k_s are the thermal conductivities of the tool and specimen respectively. The coating-contact IHTC h_c was therefore determined by the solid-contact IHTC h_s and the properties of the applied coating material. As a critical parameter in this model, the constriction parameter C_f accounted for the heat transfer across the coated substrate but extremely difficult to be calculated, as shown in Eqs. (2.13 - 2.17):

$$C_f = \frac{\psi(\varepsilon^{'},\phi_n)}{\psi(\varepsilon^{'})} \tag{2.13}$$

$$\psi(\varepsilon^{'}) = (1-\sqrt{P/H^{'}})^{1.5} \tag{2.14}$$

$$\psi(\varepsilon^{'},\phi_n) = \frac{16}{\pi\varepsilon^{'}}\sum_{n=1}^{\infty}\frac{J_1^{\,2}(\delta^{'}\varepsilon^{'})}{\delta^{'3}J_0^{\,2}(\delta^{'})}\cdot\phi_n\cdot\gamma_n\cdot\rho_n \tag{2.15}$$

$$\phi_n = K[\frac{1+K+(1-K)e^{-2\delta^{'}\varepsilon^{'}\tau^{1}}}{1+K-(1-K)e^{-2\delta^{'}\varepsilon^{'}\tau^{1}}}] \tag{2.16}$$

$$\rho_n = \frac{\sin(\delta^{'}\varepsilon^{'})}{2J_1(\delta^{'}\varepsilon^{'})} \tag{2.17}$$

More information can be found in the studies of [53]–[56]. The coating-contact IHTC is necessary to be simplified to emphasise the effects of the thermal conductivity and layer thickness of the coating on the IHTC.

In order to characterise the IHTC values under lubricated conditions, an equation was built up by Wilson et al. [13], as shown in Eq. (2.18):

$$h_l = \frac{1-A}{\delta_l}\frac{2k_lk_sk_t}{2k_tk_s-k_sk_l-k_tk_l} \tag{2.18}$$

where A is the contact area, δ_l is the applied lubricant thickness and k_l is the thermal conductivity of the lubricant. This lubricant-contact IHTC h_l was particularly developed for the application of lubricants with low thermal conductivities, representing a negative effect on the IHTC.

An empirical model was developed by Xu et al. [49] to predict the IHTC evolutions as a function of the initial temperatures of the blank T_t and die T_s, as shown in Eq. (2.19). However, this model was not able to explain the mechanisms of the initial blank temperature on the IHTC.

$$h = 778.6-6.436\sin(0.3674\pi\cdot T_s\cdot T_t)+0.634\exp(-(0.114T_t)^2) \tag{2.19}$$

Efforts have been made previously to predict the IHTC evolutions as a function of a particular influential factor, however, without a comprehensive study. Therefore, the development of a general model to predict the IHTC evolutions as a function of different influential factors, e.g. contact pressure, tool material, coating material, specimen thickness, lubricant and initial blank temperature is of great importance.

2.5 Validations of the IHTC

Constant contact pressure conditions have been typically applied in previous studies on the IHTC. However, the contact pressure may actually vary over an extremely short period of time in practical hot stamping processes of complex-shaped components [57], leading to abrupt changes in the IHTC and consequently the temperature evolutions of the blank [58]. Therefore, it is necessary to prove that the IHTC values determined under constant contact pressure could be applied to simulate the temperature evolution of the blank under variable contact pressure conditions. A variable contact pressure able to represent the load conditions in practical hot stamping processes is firstly required in order to conduct the validation test of the IHTC. A data-driven approach developed by Wang et al. [59] has been successfully used in the characterisation of variable temperature and strain rate in the hot stamping processes.

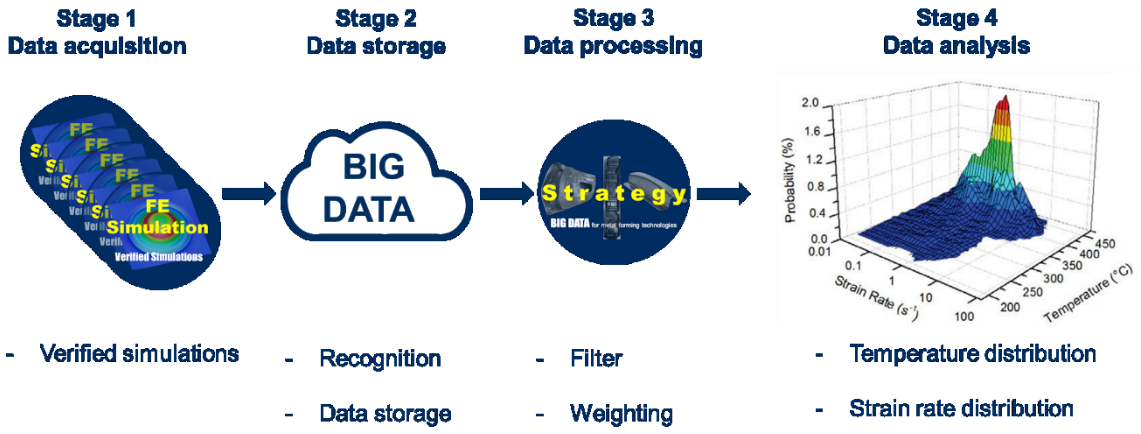

Fig. 2.10. Methodology of the data-driven approach to identify the temperature and strain rate distributions in the hot stamping processes [59].

This approach was developed by data mining of existing verified hot stamping simulations run under different forming conditions, which are currently available on the cloud-based finite element (FE) simulation platform Smart Forming [60]. It works in four stages, namely data acquisition, data storage, data processing and data analysis, as shown in Fig. 2.10. In Stage 1, data is firstly acquired through the Smart Forming platform, which consists of experimentally verified hot stamping simulation results under different forming conditions and provides the thermo-mechanical characteristics of deformation processes. Data is thus recognised and then stored in Stage 2. In Stage 3, filtering is used to eliminate the thermo-mechanical histories of irrelevant data sets to process the massive amounts of data. Data weighting is also applied to prevent distortion caused by data sets of different sizes. In Stage 4, the required thermo-mechanical parameter distributions are generated for analysis of the data. The representative temperature and strain rate values were obtained by converting the processed data into the bivariate distributions as a function of probability, as shown in Fig. 2.11. Therefore, the data-driven approach could be capable of visualising the contact pressure distribution as a function of probability to identify the representative variable contact pressure in the hot stamping processes.

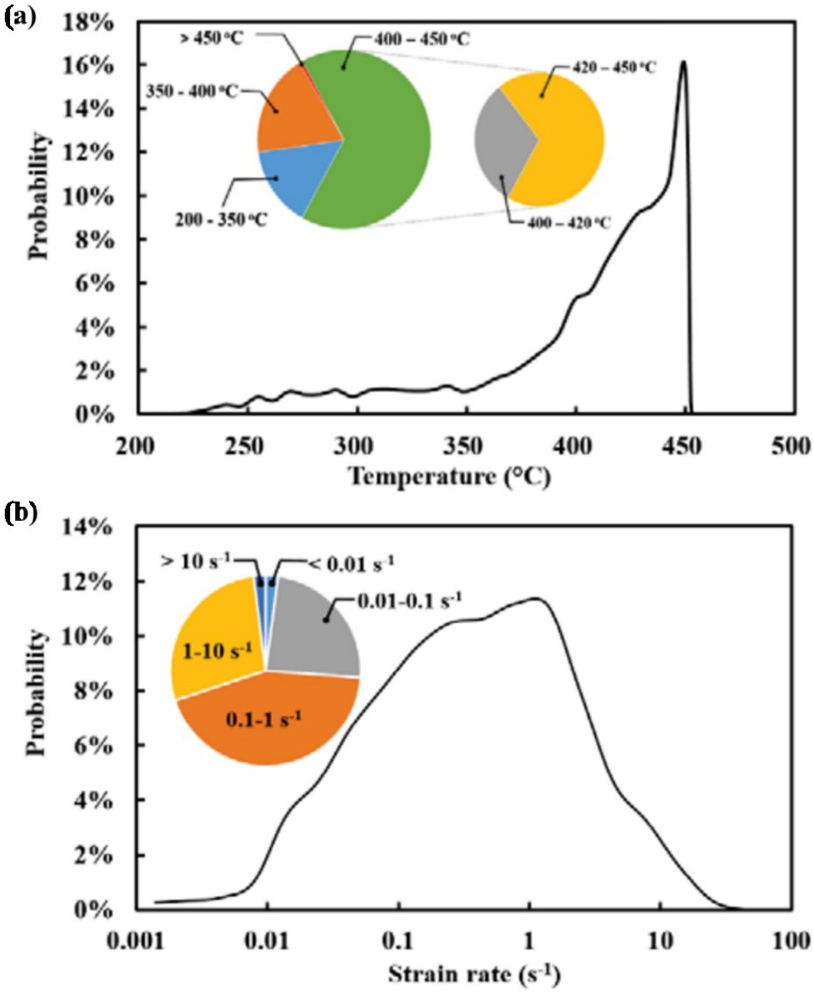

Fig. 2.11. (a) Temperature and (b) strain rate distributions as a function of probability in the hot stamping processes [59].

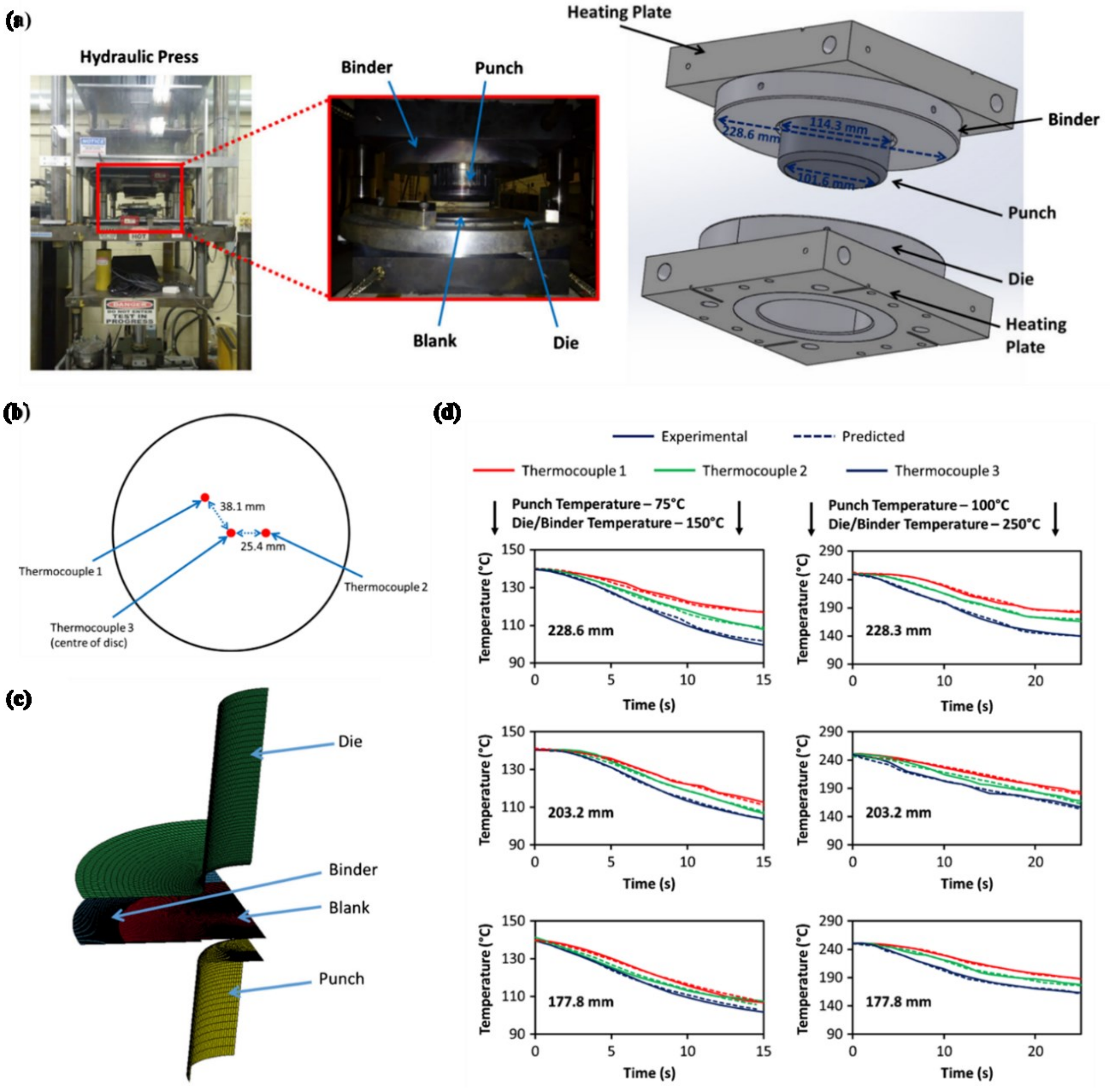

Fig. 2.12. (a) Experimental setup of the deep drawing; (b) Thermocouple locations on the blanks; (c) FE model of the deep drawing; and (d) Comparison between the experimental and predicted temperature evolutions of the AA7075 components.

Furthermore, the validation of the IHTC values in the hot stamping processes is essential for the industrial application. The deep drawing of AA7075 blanks was conducted in the study of Omer et al. [24], and their temperature evolutions were measured, as shown in Fig. 2.12 (a) and (b). The FE model was then built up in LS-Dyna finite element software with the implementation of the determined IHTC values to simulate the deep drawing process and obtain the temperature field of the formed components, as shown in Fig. 2.12 (c). The good agreement between the experimental and predicted temperature evolutions of the AA7075 components shown in Fig. 2.12 (d) verified the accuracy of the determined IHTC results. In addition to the deep drawing, the hot stamping of U-shaped components was conducted in the study of Bosetti et al. [61], validating the IHTC values through the comparison between the experimental temperature evolutions and the simulated results obtained from Comsol FE software. Previous research provided a reliable validation method. However, the hot stamping processes of complex-shaped components with much deformation have not been performed yet.

2.6 Summary

This chapter reviewed the previous work on the IHTC:

- Two sophisticated methods, i.e. the inverse heat conduction method and inverse FE simulation method, have been widely used to determine IHTC values in previous research.
- Several test facilities were also developed previously to measure the temperature evolutions of specimens under different experimental conditions.
- The effects of the contact pressure, tool material, coating material, specimen thickness, lubricant and initial blank temperature on the IHTC have been identified.
- Several studies have modelled the IHTC as a function of these influential factors.
- Non-isothermal forming of simple-shaped components to validate the determined IHTC.

However, some research gaps were found, which form the basis and novelties of this research work.

- A dedicated IHTC test facility able to ultra-precisely apply a contact pressure and measure the temperature evolution of a specimen is required to represent the temperature/pressure-sensitivity of a forming process under different conditions.
- A comprehensive study on the IHTC for aluminium alloys to identify the effects of the contact pressure, tool material, coating material, specimen thickness, lubricant and initial blank temperature has yet to be performed.
- The development of a general simplified model to predict the IHTC evolutions as a function of those influential factors is critical.
- Validation of the determined IHTC results by the hot stamping of complex-shaped components is demanded.

Chapter 3

Methodology to determine the IHTC[3]

This chapter presents the applied methodology to determine the IHTC. A dedicated IHTC test facility was first developed to precisely measure the temperature evolutions of the specimens under different experimental conditions, which were then compared to simulated curves obtained from FE software. Subsequently, the IHTC values for aluminium alloys with different thicknesses under a variety of conditions were determined by the application of different contact pressures, tools, coatings, lubricants and initial blank temperatures in the test facility, enabling the investigation of their effects on the IHTC.

3.1 Development of a dedicated IHTC test facility

3.1.1 Development of IHTC-mate 1.0

Previous IHTC test facilities necessitated manual transfers of hot specimens from a furnace to a press machine, decreasing the repeatability and accuracy of the pressure/temperature-sensitive IHTC tests. In order to realise an automatic testing system, a dedicated IHTC test facility, IHTC-mate 1.0, was developed and integrated into a Gleeble 3800 thermo-mechanical

---

[3] Chapter 3 is reproduced from two papers:

Liu, X., Fakir, O. El, Zheng, Y., Gharbi, M. M., Wang, L., 2019. Effect of tool coatings on the interfacial heat transfer coefficient in hot stamping of aluminium alloys under variable contact pressure conditions. Int. J. Heat Mass Tran. 137, 74–83.

Ji, K., **Liu, X.**, Fakir, O. El, Liu, J., Zhang, Q., Wang, L., 2016. Determination of the interfacial heat transfer coefficient in the hot stamping of AA7075. Manuf. Rev. 3, 16. doi:10.1051/mfreview/2016017 simulator, as shown in Fig. 3.1, which enables the application of a compression load up to 20 tonnes, a heating rate up to 10,000˚C/s and a ram speed up to 2000 mm/s [62].

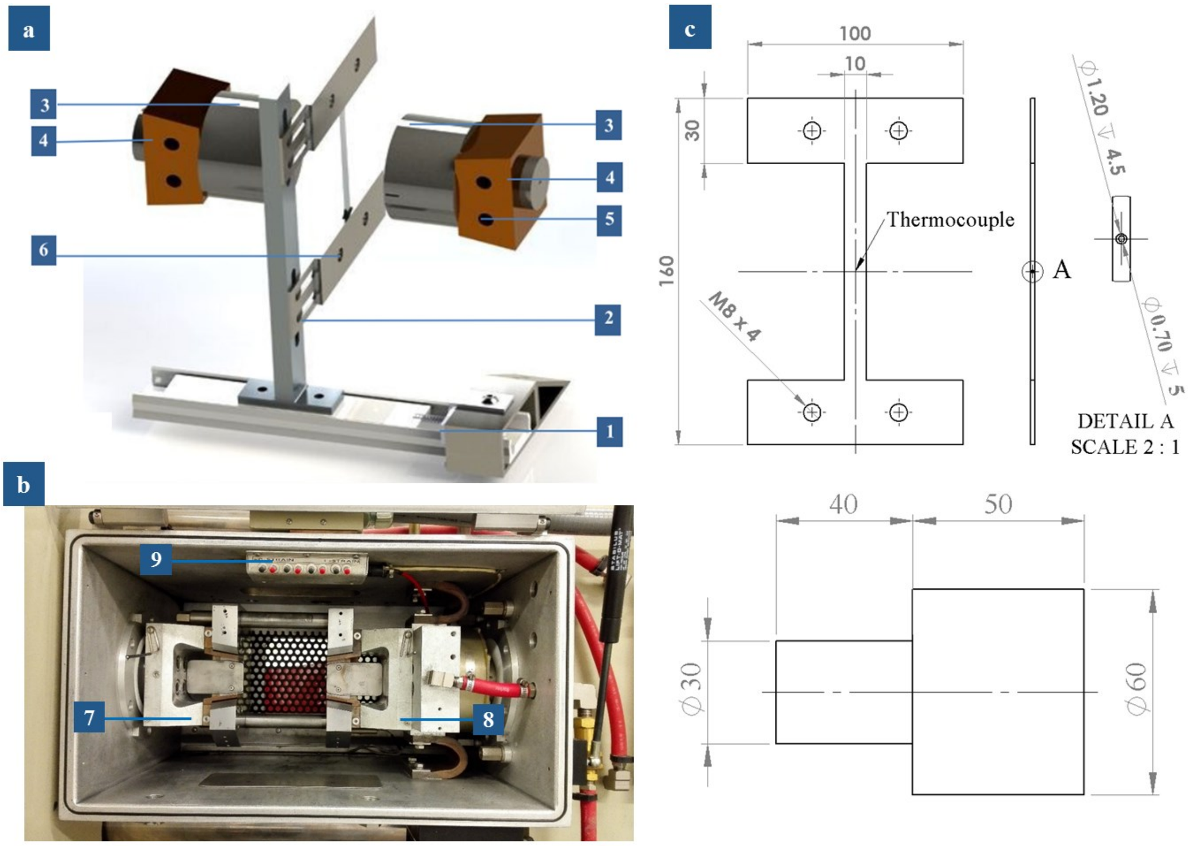

1. **Sliding rail**
2. **Blankholder**
3. **Anvils**
4. **Grippers**
5. **Power supply holes**
6. **Specimen**
7. **Mechanical jaw**
8. **Static jaw**
9. **Thermocouple data logger**

Fig. 3.1. (a) Structure of IHTC-mate 1.0; (b) Gleeble 3800 operation chamber; (c) Geometries of the specimen and tools with the location of the thermocouple.

Two cylindrical anvils (No. 3 in Fig. 3.1 (a)) with a diameter of 60 mm were gripped by two anvil grippers (No. 4 in Fig. 3.1(a)), which were then clamped within a mechanical jaw (No. 7 in Fig. 3.1 (b)) and a static jaw of the Gleeble (No. 8 in Fig. 3.1 (b)) respectively. The two anvils had the same geometry, ensuring symmetric heat transfer between the specimen and anvils during the IHTC tests. A dog-bone shaped specimen (No. 6 in Fig. 3.1 (a)) was screwed onto a blankholder (No. 2 in Fig. 3.1 (a)), which was then mounted onto a sliding rail (No. 1 in Fig. 3.1 (a)). This sliding rail was screwed onto the static jaw to allow the specimen to move along it horizontally when a load was applied by the mechanical jaw. Four cables were connected to the power supply holes on the anvils (No. 5 in Fig. 3.1 (a)), enabling the electrical resistance heating of the specimen. In order to monitor the temperature evolutions of the specimens, a pair of thermocouples was embedded mid-thickness at their centres through a two-step hole and connected to the data logger of the Gleeble (No. 9 in Fig. 3.1 (b)). Fig. 3.1 (c) shows the geometry of the specimen and the location of the thermocouple. A rectangular-shaped contact area on the specimen avoided heat concentration during heating, leading to a good homogenous temperature distribution before compression. In addition, two-step holes to embed thermocouples were much easier to be drilled on a flat surface using the equipment in the laboratory.

When the test is initiated, the punch moves towards the specimen, compressing it against the die. IHTC-mate 1.0 enables the processes of heating, compressing and quenching to be conducted automatically in a closed operation chamber, significantly improving the operation safety. Meanwhile, it does not necessitate the transfer of a hot specimen from a furnace to a press machine, dramatically increasing the repeatability and accuracy of the tests. In addition, the electrical resistance heating provides a homogeneous temperature distribution in the contact area of the specimen, ensuring symmetric heat transfer between the specimen and anvils.

IHTC-mate 1.0 was successfully manufactured and applied to determine the IHTC between a 7075 aluminium alloy and mild steel [28]. However, fluctuations were found in the experimental temperature evolutions of the specimens in the initial stages, caused by the low stiffness of the sliding rail and an unstable contact pressure being applied between the specimen and anvils. Consequently, IHTC-mate 1.0 was not capable of ultra-precision control of the contact pressure and heat transfer between the specimen and anvils. It was also found that the specimen and anvils could not be flexibly exchanged. In addition, excessive heat concentration occurred in the blankholding area of the specimen due to its dog-bone shape, leading to the power cables getting damaged. Therefore, it became necessary to enhance the stability and flexibility of the test facility before continuing the experimental investigations of the IHTC.

3.1.2 Development of IHTC-mate 2.0

In order to overcome the shortcomings of IHTC-mate 1.0, a new generation test facility, IHTC-mate 2.0, was developed and integrated into the Gleeble 3800 thermo-mechanical simulator. Two pedestals (No. 1 in Fig. 3.2) were clamped between the two jaws of the Gleeble, enabling assembly of the whole facility inside the test chamber. A recess with the same geometry as the rear of the punch and die was designed for the pedestals, enabling precise location of the tools and thus improving the repeatability of the test system assembly. A punch (No. 2 in Fig. 3.2), with a contact surface of 50 x 25 mm^2, was bolted onto the pedestal clamped to the mechanical jaw, to allow the punch to move horizontally. A die (No. 2 in Fig. 3.2, with the same dimensions as the punch) and a frame (No. 3 in Fig. 3.2) were bolted onto the pedestal clamped to the static jaw, ensuring that IHTC-mate 2.0 was stable.

In order to measure the temperature evolutions of the tools (punch and die), holes with 12.5 mm depth were drilled at a distance of 3 mm below their surfaces to embed thermocouples. The tools were also designed to be flexibly exchanged to realise different experimental requirements. The effects of the tool material, coating material and surface roughness on the IHTC could therefore be investigated by using tools with different sets of punches and dies.

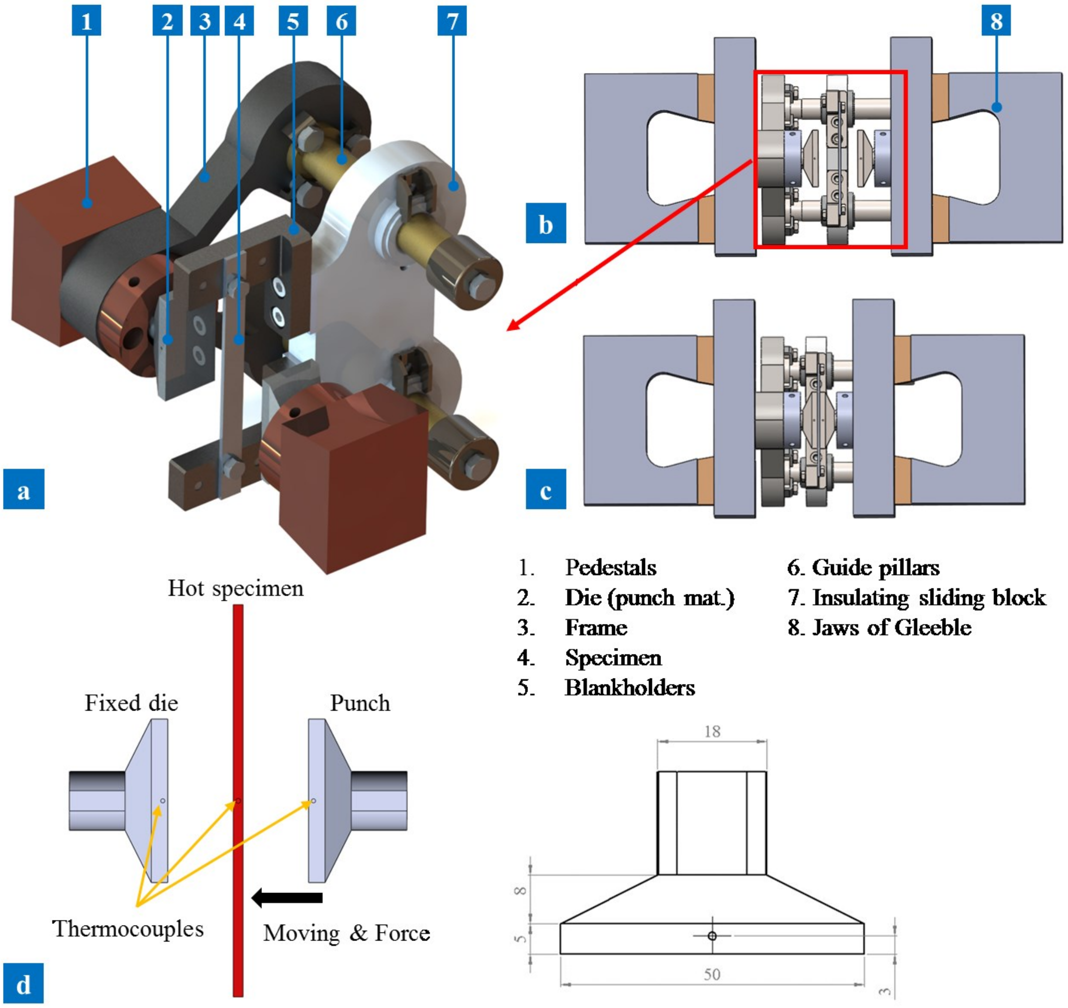

Fig. 3.2. (a) Structure of IHTC-mate 2.0; (b) The IHTC test under unloading conditions; (c) The IHTC test under loading conditions; (d) Schematic diagram of the compression between the specimen and tools, and geometry of the tools.

Prior to each test, a rectangular specimen (No.4 in Fig. 3.2) with a contact surface of 120 x 10 mm^2 was screwed onto two blankholders (No. 5 in Fig. 3.2) to position it precisely. Two power cables were screwed onto each blankholder to enable the electrical resistance heating of the specimen. Due to the symmetric location of the power cables, the current flow and thus the temperature distribution in the specimen were homogeneous during the heating processes. Furthermore, heat concentration was prevented due to the rectangular shape of the specimen. Thermocouples were embedded mid-thickness at the centre of the specimen and connected to the data logger of the Gleeble 3800 simulator, to record the temperature evolutions of the specimen during the IHTC tests, as well as to enable feedback-control of the heating process in the Gleeble to ensure that the desired temperature profile was attained.

In order to avoid short circuits during the heating process, the two blankholders were screwed onto an insulating sliding block (No. 7 in Fig. 3.2), made from an electrically and thermally insulated material with high strength. This block slides along two guide pillars (No. 6 in Fig. 3.1), mounted onto the stainless-steel frame, increasing the stability of IHTC-mate 2.0. When the test is initiated, the punch first contacts the specimen, moving the sliding block sub-assembly and specimen towards the die, before compressing it at a pre-defined contact pressure. The temperature loss of the specimen before compression is negligible at a sufficiently high punch speed.

With its compact size (approximately 200 x 120 x 120 mm) and low weight (5.2 kg), IHTC-mate 2.0 was easy to store and assemble, and safer and more efficient to operate than existing methods for measuring the IHTC. In addition, the Gleeble 3800 thermo-mechanical simulator provides a precise thermal and mechanical control system, for setting parameters including the heating rate, the target temperature, jaw speed, and compression force, through digital closed-loop feedback control and a sampling frequency ranging from 0.1 to 5000 Hz. This would be beneficial for the self-adjustment of the pre-defined contact pressure between the specimen and tools within a short time-period, contributing to a negligible temperature loss before compression at the target contact pressure and thus providing high repeatability and accuracy for the temperature/pressure-sensitive IHTC tests. Meanwhile, the solid frame and guide pillars provided a high stability for the tests. A variable contact pressure could therefore also be precisely applied and rapidly self-adjusted in an IHTC test to represent the contact pressure conditions in a practical hot stamping process. Due to its excellent performance, IHTC-mate 2.0 was manufactured and applied in the present research to measure the temperature evolutions of the specimen and thus determine the IHTC values for different aluminium alloys.

3.1.3 Development of IHTC-mate 3.0

The excellent performance of IHTC-mate 2.0 indicated that it has tremendous potential to enable the determination of IHTC values for materials other than aluminium alloys. However, the low melting point of the insulating sliding block limits its application in the characterisation of IHTC values for materials with high solution heat treatment temperatures, e.g. titanium alloys and boron steels. Therefore, the third generation of IHTC-mate was developed to realise IHTC tests under extremely high-temperature conditions. As before, a punch and die pair were assembled in two pedestals, however in this design, the specimen was clamped by two stainless-steel blankholders that could withstand high specimen temperatures. Additionally, cooling channels were designed in the blankholders to decrease their operating temperatures. In order to avoid short circuits, an insulating connector made from the same insulating material as that used in IHTC-mate 2.0, connected the two blankholders to increase the stability of IHTC-mate 3.0, as shown in Fig. 3.3 (a). The blankholders would now also slide along four guide pillars that were mounted onto another four insulating mounts to avoid short circuits. These insulating mounts were assembled in the two symmetric stainless-steel frames.

Due to the design of the blankholders and cooling channels, high target temperatures could be applied in the IHTC tests when using IHTC-mate 3.0. Furthermore, the application of the two symmetric stainless-steel frames could significantly increase the stability and stiffness of IHTC-mate 3.0. Consequently, torque through the blankholders and thus potential damage of the test facility could be prevented when tools were used to deform a specimen into a specific component geometry. Therefore, when using tools with such specific geometries, IHTC-mate 3.0 could enable laboratory-scale hot stamping processes to be conducted for optimisation of processing parameters, e.g. the forming temperature, heating rate, soaking time and die-closing force. Fig. 3.3 (b) shows an example of forming tools to deform a specimen into an M-shaped component. Due to its excellent characteristics, a patent application for IHTC-mate 3.0 is currently in progress, and it will be applied in the determination of the IHTC for titanium alloys and boron steels, as well as the hot stamping of laboratory-scale components. By comparison, IHTC-mate 2.0 is easier to be operated to determine the IHTC for aluminium alloys.

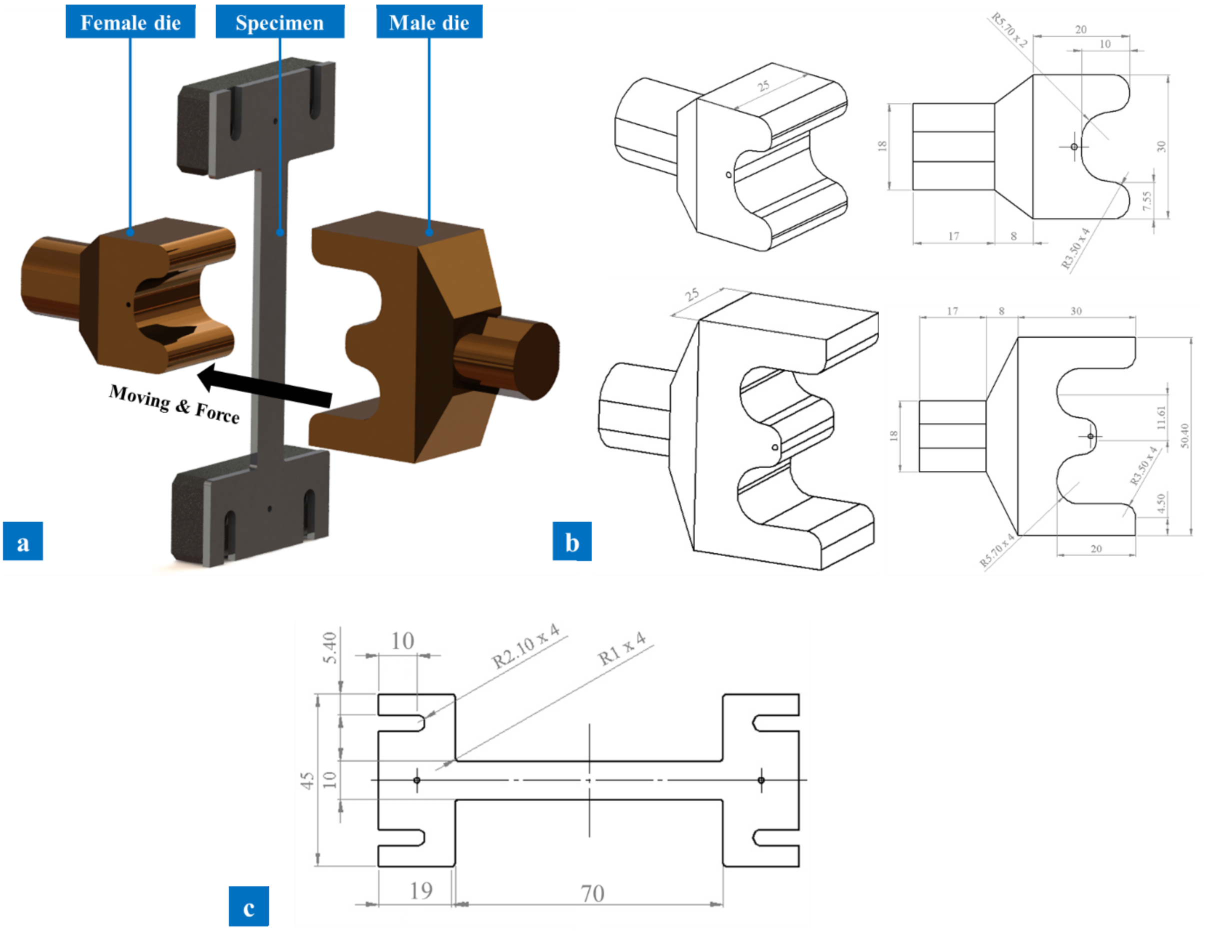

Fig. 3.3. (a) Structures of the M-shaped forming tools and specimen in IHTC-Mate 3.0; (b) Geometries of the forming tools; and (c) Geometries of the specimen.

3.2 Experimental procedures

The experimental procedures in this research work were carried out using IHTC-mate 2.0 alone. A hole with a diameter of 1.3 mm and a depth of 5 mm was drilled mid-thickness at the centre of a specimen to embed a pair of thermocouples, which was then screwed onto IHTC-mate 2.0, as shown in Fig. 3.4. The specimen was firstly heated by direct electrical resistance heating to its solution heat treatment (SHT) temperature at a heating rate of 10°C/s, while the temperature of the tools was maintained at room temperature. Once the target temperature was reached, the punch was instantly actuated to move towards the specimen at a speed of 400 mm/s and compressed it against the die at different pre-defined contact pressures. After compression, the punch was moved back to its initial position. The temperature evolutions of the specimen and the tools were recorded throughout the test. This procedure represented a hot stamping process and was automatically feedback-controlled by the Gleeble 3800's computer program QuickSim, shown in Fig. 3.5.

H13 and cast-iron G3500 steel tools were first used to study the effects of contact pressure and tool material on the IHTC. The material properties [63] and surface roughnesses of the tools, measured using White Light Interferometry equipment (Wyko NT9100), are shown in Table 3.1.

Table 3.1. Material properties and surface roughnesses of H13, cast-iron G3500 and P20 tools [63]

Property	**H13**	**Cast-iron G3500**	**P20**
Young's modulus (GPa)	210	101.4	205
Density (kg/m^3)	7800	7150	7850
Thermal conductivity (W/mK)	24.4	44	31.5
Specific heat capacity (J/kgK)	460	465	473
Surface roughness (nm)	980	810	960

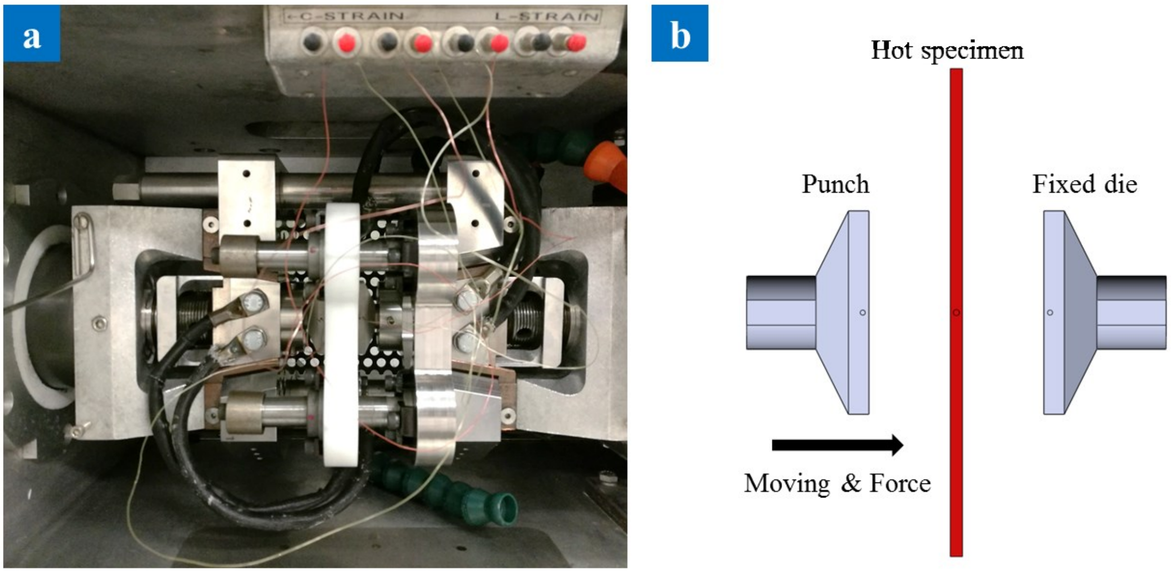

Fig. 3.4. (a) Integration of the Gleeble 3800 and IHTC-mate 2.0; (b) Schematic diagram of the compression between the specimen and dies.

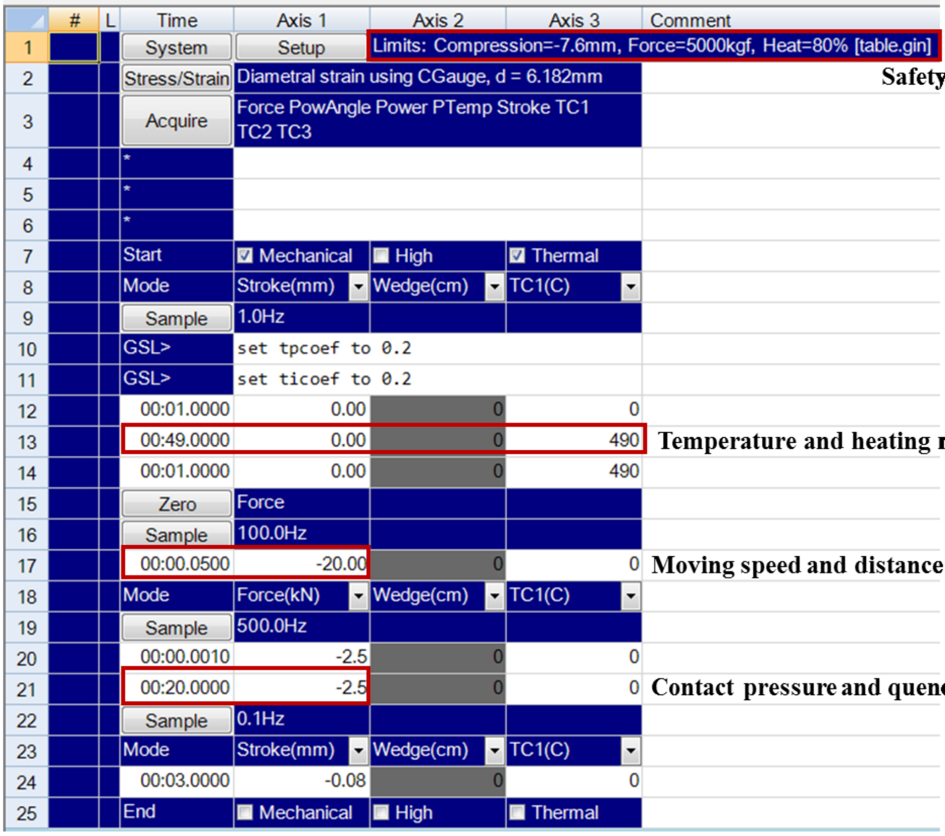

	#	L	Time	Axis 1	Axis 2	Axis 3	Comment
1			System	Setup	Limits: Compression=-7.6mm, Force=5000kgf, Heat=80% [table.gin]		
2			Stress/Strain	Diametral strain using CGauge, d = 6.182mm			
3			Acquire	Force PowAngle Power PTemp Stroke TC1 TC2 TC3			
4			*				
5			*				
6			*				
7			Start	☑ Mechanical	☐ High	☑ Thermal	
8			Mode	Stroke(mm) ▾	Wedge(cm) ▾	TC1(C) ▾	
9			Sample	1.0Hz			
10			GSL>	`set tpcoef to 0.2`			
11			GSL>	`set ticoef to 0.2`			
12			00:01.0000	0.00	0	0	
13			00:49.0000	0.00	0	490	
14			00:01.0000	0.00	0	490	
15			Zero	Force			
16			Sample	100.0Hz			
17			00:00.0500	-20.00	0	0	
18			Mode	Force(kN) ▾	Wedge(cm) ▾	TC1(C) ▾	
19			Sample	500.0Hz			
20			00:00.0010	-2.5	0	0	
21			00:20.0000	-2.5	0	0	
22			Sample	0.1Hz			
23			Mode	Stroke(mm) ▾	Wedge(cm) ▾	TC1(C) ▾	
24			00:03.0000	-0.08	0	0	
25			End	☐ Mechanical	☐ High	☐ Thermal	

Safety control

Temperature and heating rate control

Moving speed and distance control

Contact pressure and quenching time control

Fig. 3.5. Computer program QuickSim.

In order to study the effects of tool coating on the IHTC, eight pairs of uncoated/coated tools with identical geometries and a contact surface of 50 x 25 mm^2 supplied by Schuler Pressen GmbH were used in the present research. The tool materials were Substrate 1, made from a hot working steel, Substrate 2, made from a cast-iron steel, and Substrate 3, made from a cold working steel, whilst the coating materials were an aluminium chromium nitride (AlCrN) physical vapour deposition (PVD) coating, a chromium nitride (CrN) PVD coating and a titanium nitride (TiN) chemical vapour deposition (CVD) coating. The thicknesses and thermal conductivities of the coatings, as well as the material properties of the tool materials, were provided by Schuler Pressen GmbH, as shown in Tables 3.2 and 3.3. Those material properties could ensure accurate FE simulations. The surface roughnesses of the uncoated tools were treated by Schuler to approach those of the coated tools. Hence the effect of surface roughness on the IHTC was negligible when studying the effect of coating materials on the IHTC.

Table 3.2. Material properties of the applied substrates [64]

Property	**Sub 1**	**Sub 2**	**Sub 3**
Young's modulus (GPa)	205	212	110
Density (kg/m^3)	7600	7700	7200
Thermal conductivity (kW/mK)	0.0315	0.046	0.0219
Specific heat capacity (J/kgK)	460	470	506
Surface roughness (nm)	770	1150	790

Table 3.3. Thicknesses and thermal conductivities of the applied coatings [65]

No.	**Sub.**	**Coating**	**Coating thick. (μm)**	**Coating thermal cond. (kW/mK)**
1	Sub 1	Uncoated	---	---
2	---	AlCrN	3	0.0028
3	---	CrN	6	0.012
4	Sub 2	Uncoated	---	---
5	---	AlCrN	2	0.0028
6	---	CrN	3	0.012
7	Sub 3	Uncoated	---	---
8	---	TiN	8	0.019

In order to study the lubricant and its layer thickness effects on the IHTC, a graphite lubricant, supplied by Sovereign Lubricants Ltd., was weighed using a bench scale with a precision of 0.001 g and then applied onto the tool surfaces. The target lubricant layer thickness was calculated using the lubricant density of 1.33 g/cm^3 and the tool surface area of 1250 mm^2. A dedicated film thickness gauge was then used to verify whether the target lubricant layer thickness was uniformly achieved over the tool surfaces with an accuracy of ±10 μm. A chemical detergent was used to clean the tool surfaces after each IHTC test. Equipment able to apply lubricants with ultra-precise control would be required especially when studying the effect of the lubricant thickness on the IHTC in future work.

The IHTCs for 7075 and 6082 aluminium alloys, supplied by AMAG Austria Metal AG in the T6 condition, were determined in the present research for the different substrates, coatings and lubrication conditions. The chemical compositions of AA7075-T6 and AA6082-T6 are shown in Table 3.4, while their material properties and surface roughnesses are shown in Table 3.5. The material properties obtained from the previous studies were close to those last updated on Material Property Database MatWeb [66].

Table 3.4. Chemical compositions of AA7075 and AA6082 [67]

AA7075-T6										
Element	Si	Fe	Cu	Mn	Mg	Cr	Zn	Ti	Others each (max)	Al
Wt%	0.09	0.13	1.4	0.05	2.6	0.19	5.7	0.03	0.02	Bal.
AA6082-T6										
Element	Si	Fe	Cu	Mn	Mg	Cr	Zn	Ti	Others each (max)	Al
Wt%	0.9	0.38	0.08	0.42	0.7	0.02	0.05	0.03	0.02	Bal.

Table 3.5. Material properties and surface roughnesses of AA7075 [68] and AA6082 [69]

Property	**AA7075**	**AA6082**
Young's modulus (GPa)	63	70
Density (kg/m^3)	2770	2700
Thermal conductivity (kW/mK)	0.14	0.17
Specific heat capacity (J/kgK)	949	890
Surface roughness (nm)	340	430

3.3 Finite element simulation procedures

3.3.1 FE simulation of the IHTC tests in PAM-STAMP

In order to simulate the temperature evolutions of the specimen and tools and then compared with the experimental results, a FE model was built up in PAM-STAMP, which enables modelling of the interactions between mechanical and thermal fields [70], as well as heat transfer in 3D. The dimensions of the specimen and tools were the same as those used in IHTC-mate 2.0, as shown in Fig. 3.6. The corresponding material properties of the specimens and tools were also implemented in the FE simulations. Table 3.6 shows the yield strength and ultimate strength of AA7075 and AA6082 at elevated temperatures, which were obtained from the uniaxial tensile tests.

Table 3.6. Yield strengths and ultimate strengths of AA7075 and AA6082 at elevated temperatures.

Temperature	**AA7075**		**AA6082**	
	Yield (MPa)	Ultimate (MPa)	Yield (MPa)	Ultimate (MPa)
350˚C	96	101	78	96
400˚C	64	74	59	68
450˚C	53	60	49	61
500˚C	40	43	42	54
535˚C	-	-	34	40

Quadrangle thermal shell elements were used for the specimen to precisely represent the heat transfer mechanism that occurs during the hot stamping process. The selected element size of 2 mm ensured that the temperature at the centre of the specimen could be accurately captured while providing a reasonable computational time. The same element type and size were selected for the majority of the regions on the tools, while explicit triangle thermal shell elements were used for some regions near circular edges. The total number of elements of the specimen (No.1 in Fig. 3.6), punch/die (No.2 & 3 in Fig. 3.6), blankholders (No.4 in Fig. 3.6) and screws (No.5 in Fig. 3.6) were 240, 325, 634 and 216 respectively.

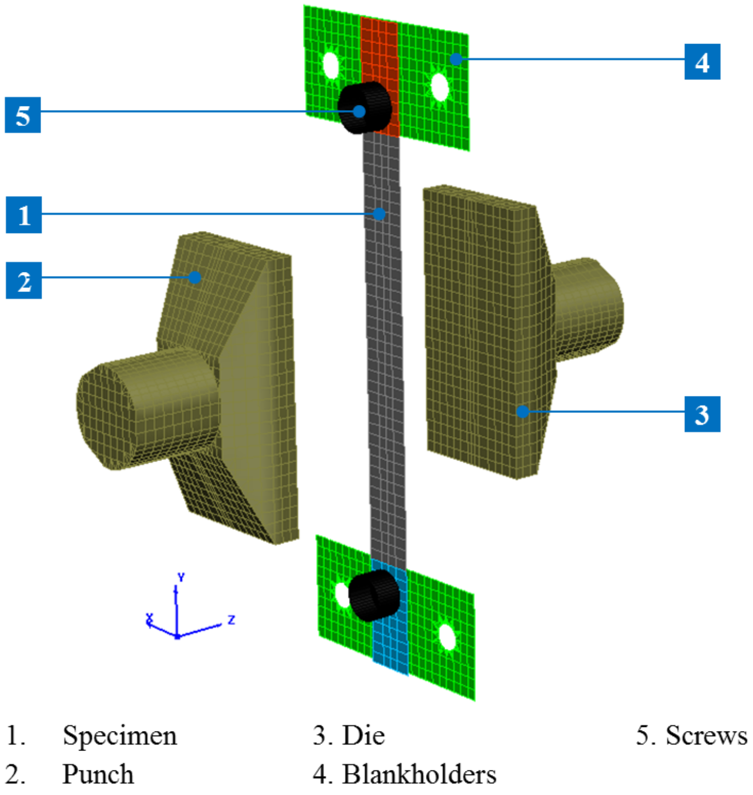

Fig. 3.6. The FE model of the IHTC test in PAM-STAMP.

'Hotforming double action validation' was selected as the simulation process type in PAM-STAMP and was composed of four stages, i.e. gravity, holding, stamping and quenching. All six degrees of freedom were restricted for the die, while all degrees of freedom, except for that in the z-direction (direction of punch motion), were restricted for the punch, blankholders and screws. The specimen was able to deform in all degrees of freedom. In the gravity and holding stages, the specimen was located and held by the blankholders and screws. In the subsequent stamping and quenching stages, the punch moved towards the specimen at the same speed as that in the experiments and compressed it against the die for 4 seconds. The temperature of each component was assumed to be stable before compression, while the air convection value was assumed as 20 W/m^{2}K [25].

A constant IHTC value was assigned for each simulation to eliminate the effect of contact pressure, tool coating, lubricant and surface roughness on the temperature evolution of the specimen. The temperature evolutions, at the same locations as those in the experiments, were then plotted and compared with the experimental results. The experimental and simulated curves with the best agreement indicated that the IHTC assigned in that simulation was the corresponding value at the selected experimental conditions.

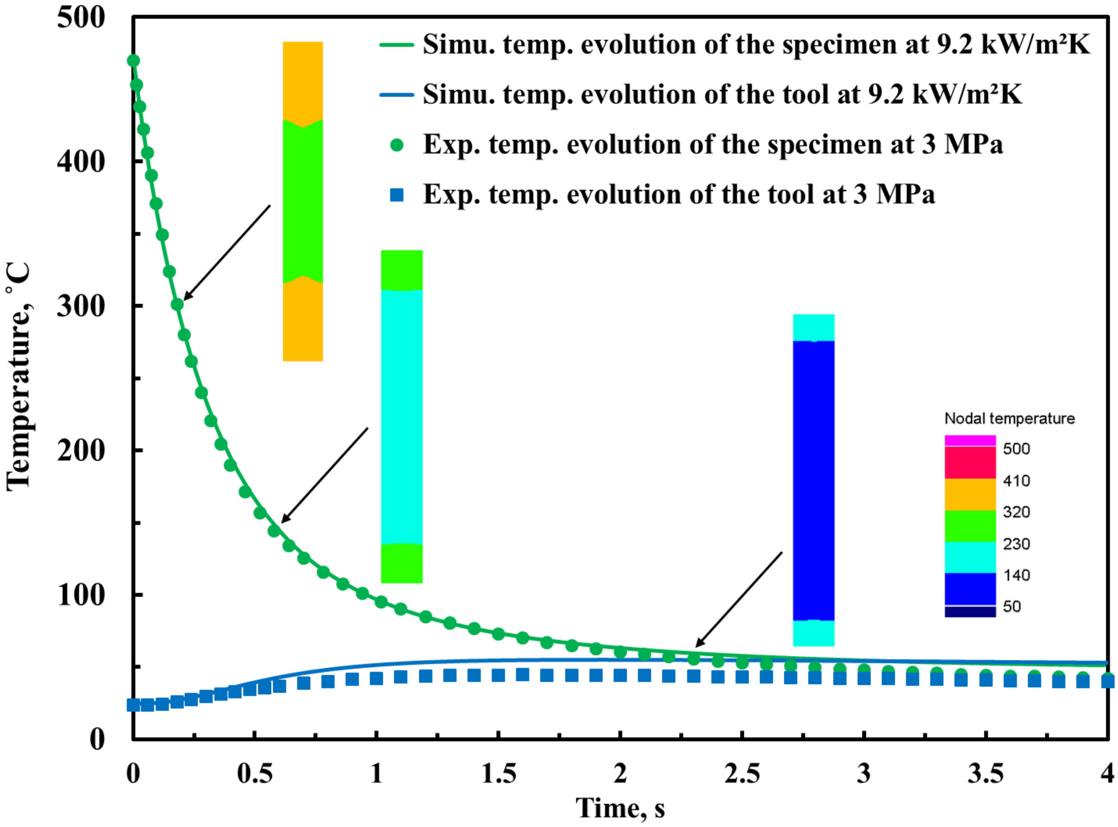

Fig. 3.7. Experimental and simulated temperature evolutions of an AA7075 specimen and cast-iron G3500 tools at a contact pressure of 3 MPa under dry conditions.

Fig. 3.7 shows the comparison of the temperature evolutions of an AA7075 specimen and uncoated cast-iron G3500 tools obtained from a simulation assigned an IHTC value of 9.2 kW/m^{2}K and from an experiment with a contact pressure of 3 MPa under dry conditions. From the results, it was found that the temperature of the specimen dropped drastically in the first 2 seconds, while the punch temperature increased gradually with time. The experimental temperature evolutions agreed well with the simulated curves, which indicated that the IHTC value between AA7075 and cast-iron G3500 was 9.2 kW/m^{2}K when the contact pressure was 3 MPa under dry conditions.

3.3.2 FE simulation of the IHTC tests in ABAQUS

In order to examine whether different FE software is also applicable to the determination of the IHTC, an identical FE model was built up in a different FE software ABAQUS, as shown in Fig. 3.8. The same processing parameters, e.g. initial temperature and moving speed, and the same material properties of the specimen and tools, were implemented to simulate the IHTC tests. 8-node trilinear displacement-temperature solid elements (C3D8T) with a size of 1 x 1 x

1 mm^3 were used for the 2 mm thick specimen, ensuring a high accuracy while maintaining a minimal computational time. The application of an even number of elements for the specimen ensured that the temperature evolution of the node at its mid-thickness could be measured. Therefore, solid elements with different sizes of 1 x 1 x 0.75 mm^3 and 1 x 1 x 0.83 mm^3 were used for the specimens with 3 and 5 mm thicknesses respectively.

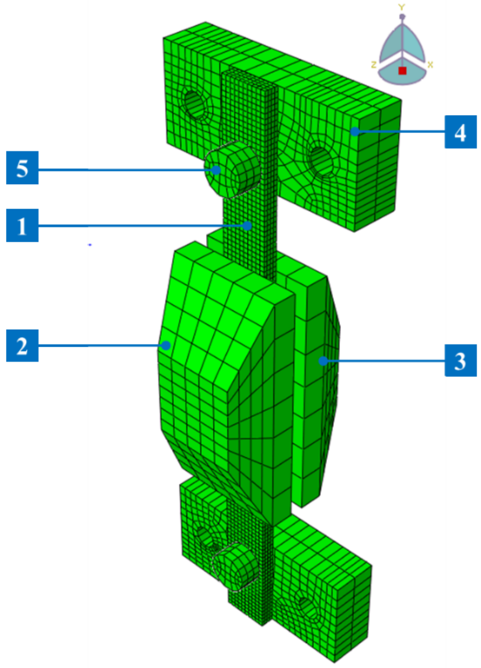

1. Specimen 3. Die 5. Screws
2. Punch 4. Blankholders

Fig. 3.8. The FE model of the IHTC test in ABAQUS.

As shown in Fig. 3.9, the experimental temperature evolutions of a 3 mm thick AA6082 specimen at the contact pressures of 5 and 30 MPa had the best agreement with the simulated results obtained from ABAQUS at the IHTC values of 8 and 17 kW/m^{2}K respectively. When the experimental temperature evolutions were compared to the simulated results obtained from PAM-STAMP, the corresponding IHTC values were 8.5 and 17.4 kW/m^{2}K. It was found that the IHTC values determined by using PAM-STAMP were higher than those determined by using ABAQUS under the same conditions, as shown in Fig. 3.10, which might be caused by the application of different element types and calculation formula in the two FE software. Further study is demanded to investigate the effects of the element type and calculation formula on the FE simulation results.

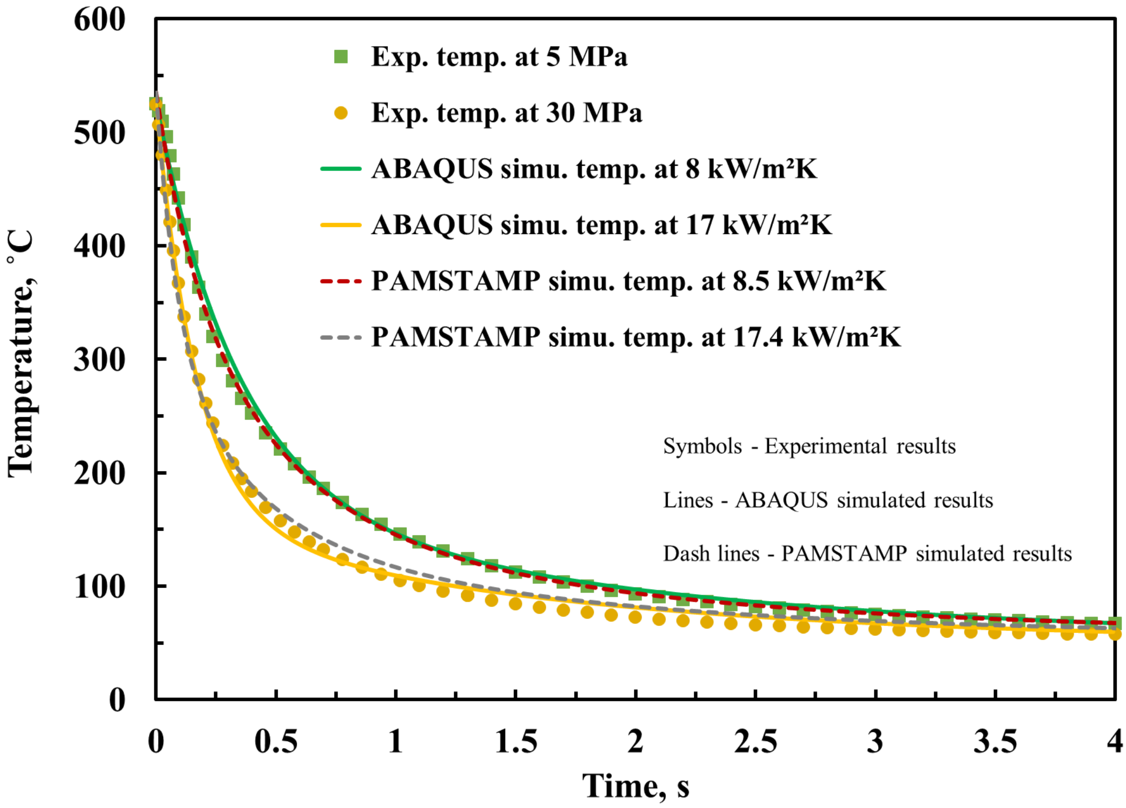

Fig. 3.9. Comparison between the experimental temperature evolutions of the 3 mm thick AA6082 specimen and the simulated results obtained from ABAQUS and PAM-STAMP.

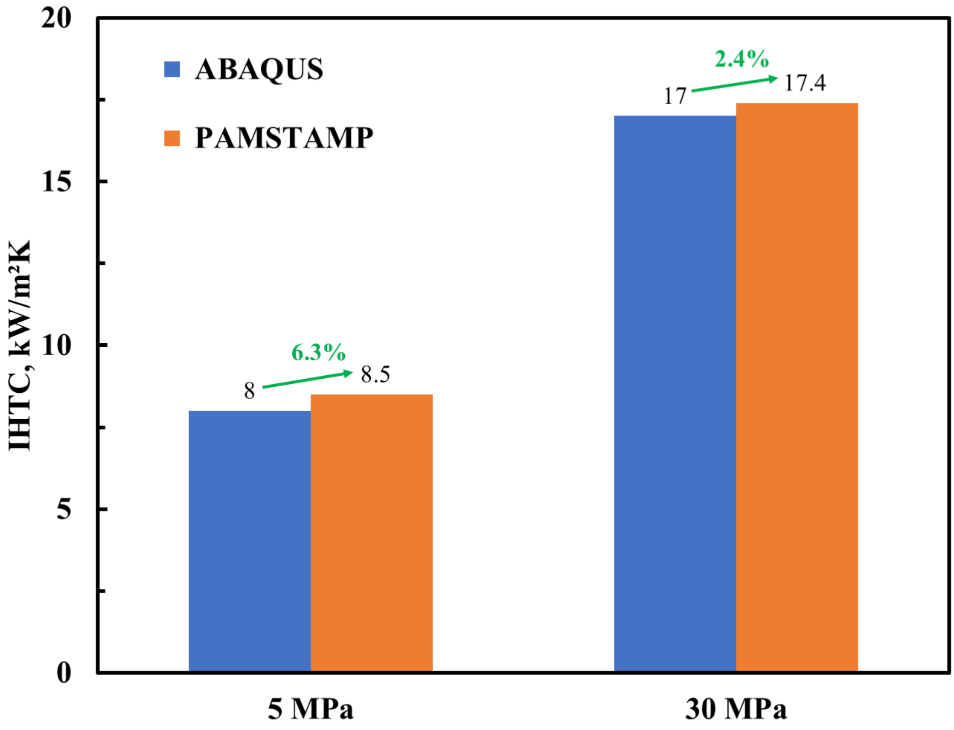

Fig. 3.10. Difference in the IHTC determined by ABAQUS and PAM-STAMP.

3.4 Summary

The work presented in this chapter is summaries as below:

- A dedicated IHTC test facility, IHTC-mate, was developed to precisely measure the temperature evolutions of aluminium specimens undergoing heat transfer.
- In order to increase its stability and repeatability, IHTC-mate 2.0 was subsequently developed and applied in the present research to accurately determine the IHTC values for different aluminium alloys with ultra-precise control. Furthermore, IHTC-mate 2.0 was capable of conducting IHTC tests under variable contact pressure conditions and measuring the consequent temperature evolution of the specimen with abrupt pressure changes to represent practical hot stamping processes of complex-shaped components.
- In order to determine the IHTC values for materials with extremely high solution heat treatment temperatures, IHTC-mate 3.0 was developed to enable the application of high target temperatures in the IHTC tests. In addition, IHTC-mate 3.0 was capable of conducting hot stamping of laboratory-scale components due to its excellent stability and stiffness.
- A FE model was also built up in PAM-STAMP to simulate the temperature evolutions of the specimens in the IHTC tests. The IHTC values for 7075 and 6082 aluminium alloys could subsequently be determined under different experimental conditions by using the inverse FE simulation method. Different contact pressures, tools, coatings, specimens, lubricants and initial blank temperatures were applied in the test facility to investigate their effects on the IHTC.
- Further study is required to investigate the effects of the element type and calculation formula on the FE simulation results, which would be beneficial to realise the application of different software to the determination of the IHTC.

Chapter 4

Influential factors on the IHTC[4]

This chapter presents the determined IHTC values for 7075 and 6082 aluminium alloys under different experimental conditions. The effects of the contact pressure, tool material, coating material, specimen thickness, lubricant and initial blank temperature on the IHTC are subsequently studied, and their heat transfer mechanisms are also explained in this chapter.

4.1 Effect of contact pressure on the IHTC

The effect of the contact pressure on the IHTC was first investigated with all other parameters, e.g. tool material, coating, specimen thickness, lubricant and initial blank temperature, as constant values. Similarly, all parameters were maintained in Sections 4.2 to 4.6, in addition to the influential factor investigated in that section. As shown in Fig. 4.1, when H13 was used as the tool material, the IHTC for AA7075 increased considerably from 0.7 kW/m^{2}K to approximately 8.2 kW/m^{2}K when the contact pressure increased from 0 to 7 MPa under dry conditions, followed by a moderate increase as the contact pressure increased from 7 to 10 MPa. When the contact pressure was higher than 13 MPa, a plateau of the IHTC was observed, with a value of approximately 8.6 kW/m^{2}K.

---

[4] Chapter 4 was reproduced from two papers:

Liu, X., Fakir, O. El, Meng, L., Sun, X., Li, X., Wang, L., 2018. Effects of lubricant on the IHTC during the hot stamping of AA6082 aluminium alloy: experimental and modelling studies. J. Mater. Process. Technol. 255, 175–183. doi:10.1016/j.jmatprotec.2017.12.013

Liu, X., Fakir, O. El, Cai, Z., Gharbi, M. M., Dalkaya, B., Wang, L., 2019. Development of an interfacial heat transfer coefficient model for the hot and warm aluminium stamping processes under different initial blank temperature conditions. J. Mater. Process. Technol. 273, 116245.

The symbols shown in Figs 4.1 to 4.11 were the experimental IHTC results, while the lines were the IHTC evolutions predicted by a mechanism-based model, which was stated in Chapter 5. The variation of the IHTC values could be explained by the evolutions of the real contact area at different contact pressures [71].

The real contact area between the specimen and tools is usually much less than the apparent contact area and increases with increasing contact pressure due to the variation of the specimen surface condition [72]. This is beneficial for the interfacial heat transfer between the specimen and tools, leading to an increase in the IHTC with increasing contact pressure.

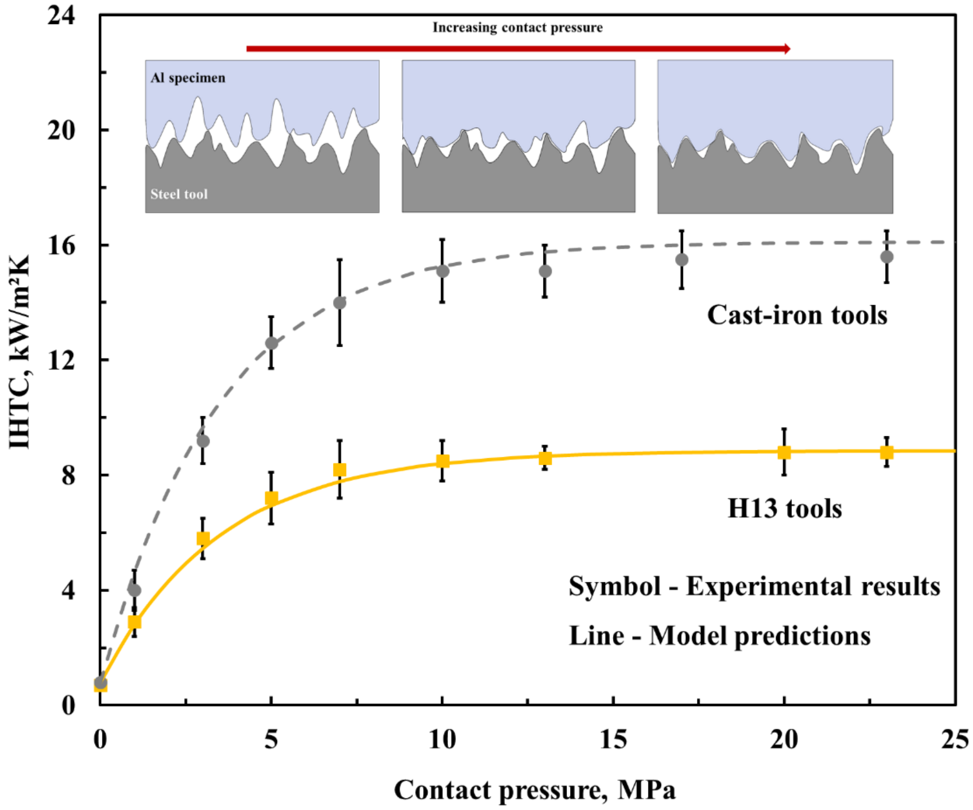

Fig. 4.1. Experimental IHTC evolutions with contact pressure for AA7075 using H13 and cast-iron G3500 tools under dry conditions.

In order to characterise the relationship between the real contact area and contact pressure, the average surface roughness of the H13 tools and the specimens were measured after the IHTC tests. The average surface roughness of the H13 tools remained stable at 980 nm throughout the experiments, whilst for the specimen this value varied with the contact pressure. The stiffness of H13 within the temperature range used in the experiments was much larger than that of AA7075 at elevated temperatures. As a result, the surfaces of the specimens were deformed by the tools during the hot stamping processes, and thus the surface roughness of the specimens increased correspondingly. Therefore, the real contact area was growing because the two contact surfaces increasingly meshed together.

As shown in Fig. 4.2, the surface roughness of the specimen increased slightly from 340 to 380 nm as the contact pressure increased from 0 to 5 MPa. During this stage, deformations occurred at the surface of the specimen, and thereby the real contact area increased. After the experiments, the elastic deformations recovered but the plastic deformations remained. As a result, the surface roughness of the specimen increased slightly but resulted in the rapid growth of the IHTC value. After yielding, the surface roughness increased dramatically from 380 nm at 5 MPa to 860 nm at 10MPa, and correspondingly the IHTC value continued to grow rapidly. When the pressure was larger than 10 MPa, the surface roughness of the specimen increased gently to 910 nm, approaching the value for that of the H13 tools. During this stage, the two contact surfaces meshed to the maximum extent, and thus the real contact area reached its peak. Consequently, a plateau of the IHTC was observed. In addition, the IHTC evolutions with contact pressure for AA6082 when using different tools followed a similar logarithmical increasing trend, as shown in Fig. 4.9 in Section 4.4, indicating that the effect of the contact pressure on the IHTC is consistent for different aluminium alloys and tools.

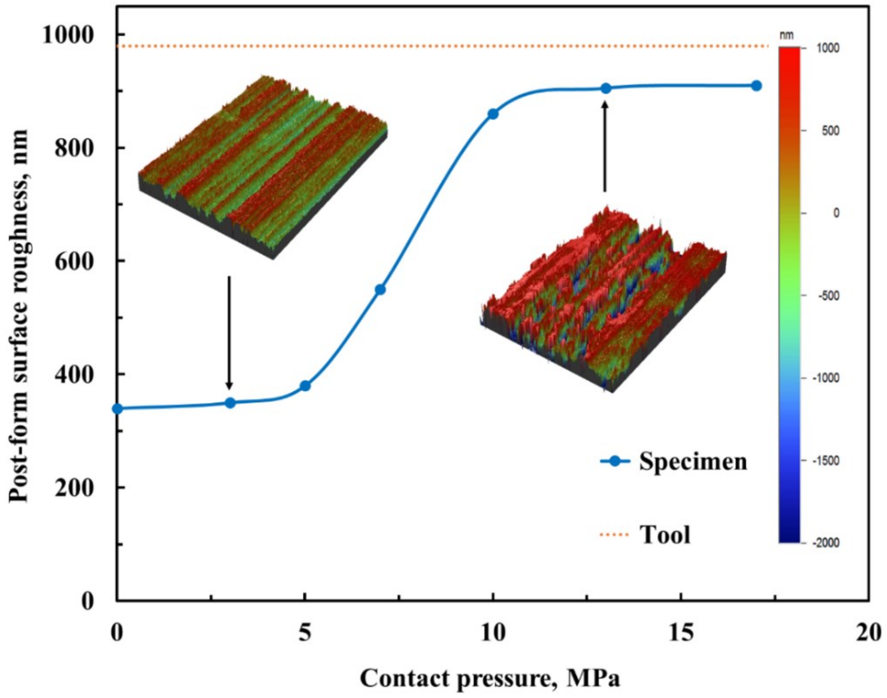

Fig. 4.2. Surface roughness evolution of the AA7075 specimen with contact pressure after the IHTC tests using H13 tools.

The surface roughness of the specimen was smaller than that of the tools in this case; while Section 4.6 shows a different case, i.e. the surface roughness of the specimen was larger than that of the tools. In that case, the asperities on the specimen were crashed by the tools during compression, leading to the increasing mesh between the specimen and tools. Consequently, the real contact area and thus the IHTC increased with increasing contact pressure. Therefore, the IHTC logarithmically increases with increasing contact pressure, regardless of the relationship of surface roughness between the specimen and tools. In the present research, the average surface roughness was measured to represent the real contact area. The calculation of the real contact area by the statistical analysis of surface skewness and kurtosis will be performed in future work [73].

In general, the critical cooling rate for 7xxx aluminium alloys is above 50°C/s, and this value is alloying element dependent, i.e. a higher cooling rate is required for an increasing content of alloying elements during quenching [74]. Through superimposing the quenching curves obtained from the experimental temperature evolutions with the continuous cooling precipitation (CCP) diagrams for the present aluminium alloys [75], the required contact pressure to achieve the critical cooling rate could therefore be identified [18]. Fig. 1.6 in Section 1.1 shows an example of the identification of the critical cooling rate for 6082 aluminium alloys. An excessive contact pressure could also be prevented from being applied between the two contact surfaces by accounting for the plateau value of the IHTC. This would be beneficial to the reduction of tool wear, the extension of tool service life and the promotion of cost efficiency in hot stamping processes.

4.2 Effect of tool material on the IHTC

When the cast-iron G3500 tools were applied, the evolution of the IHTC under dry conditions followed a similar trend to that of the H13 tools, i.e. a sharp increase at the initial stage, followed by a plateau at high contact pressures, as shown in Fig. 4.1. Specifically, the IHTC for AA7075 increased dramatically from 0.8 kW/m^{2}K at 0 MPa to 14 kW/m^{2}K at 7 MPa. When the contact pressure reached 13 MPa, the IHTC converged to a value of 15.2 kW/m^{2}K. The application of the cast-iron G3500 tools raised the peak IHTC value by approximately 77%, compared to that when the H13 tools were used.

Within the temperature range used in the experiments, the average thermal conductivity of cast-iron G3500, 0.044 kW/mK, is approximately 80% higher than that of H13, which is 0.0244 kW/mK. This indicated that the heat transfer occurred at a higher rate across the cast-iron G3500 tools than across the H13 tools, thus leading to higher IHTC values. The difference in the specific heat capacity between H13 (460 J/kgK) and cast-iron G3500 (465 J/kgK) is negligible in this study. It would therefore be desirable to deduce the influence of the thermal conductivity of the different tools on their resulting different IHTC values.

The temperature distributions in specimens and tools, either uniform or tailored, play a crucial role in hot stamping processes, influencing the post-form strength and thickness distribution of the formed component. The application of different contact pressures and different materials in specific regions of tools are notable and influential factors that could achieve desired temperature distributions. Tool materials with high thermal conductivities, e.g. cast-iron, can be used for the punch and die for manufacturing quenching rate-sensitive materials. Meanwhile, materials with low thermal conductivities, e.g. H13, can be used for blankholders to prevent the temperature of a specimen from dropping significantly in the blankholding regions of a forming tool during forming, thus enabling more material to be drawn into the tool cavity.

Compared with previous research, the IHTC values for AA7075, using either H13 or cast-iron G3500 tools, are much higher than those of Ti-6Al-4V titanium alloy, 22MnB5 boron steel and carbon steel, thus resulting in much shorter required quenching times for hot stamping processes. In addition, the contact pressure values at which the IHTC value plateaus, using either H13 or cast-iron G3500 tools, are much lower than those of titanium alloys and high strength steels, due to the lower strength of aluminium alloys at elevated temperatures. This desirable feature would reduce the requirements of the capabilities of the forming press and extend the tool life.

4.3 Effect of tool coating on the IHTC

In order to study the influence of the tool coatings on the IHTC, each pair of coated tools supplied by Schuler GmbH was assembled on IHTC-mate 2.0, and the IHTC tests were conducted. A different batch of AA7075 blank sheets with an approximate surface roughness of 210 nm was used in this section. The effect of different coatings deposited onto the same tool (the substrate) on the IHTC for AA7075 was firstly investigated. When AlCrN-coated

Substrate 1 was used, the IHTC increased from 0.5 to 6 kW/m^{2}K when the contact pressure was increased from 0 to 10 MPa and converged to an approximate value of 7 kW/m^{2}K after 15 MPa, which was approximately 48% lower than that when using Substrate 1 uncoated (13.5 kW/m^{2}K), as shown in Fig. 4.3.

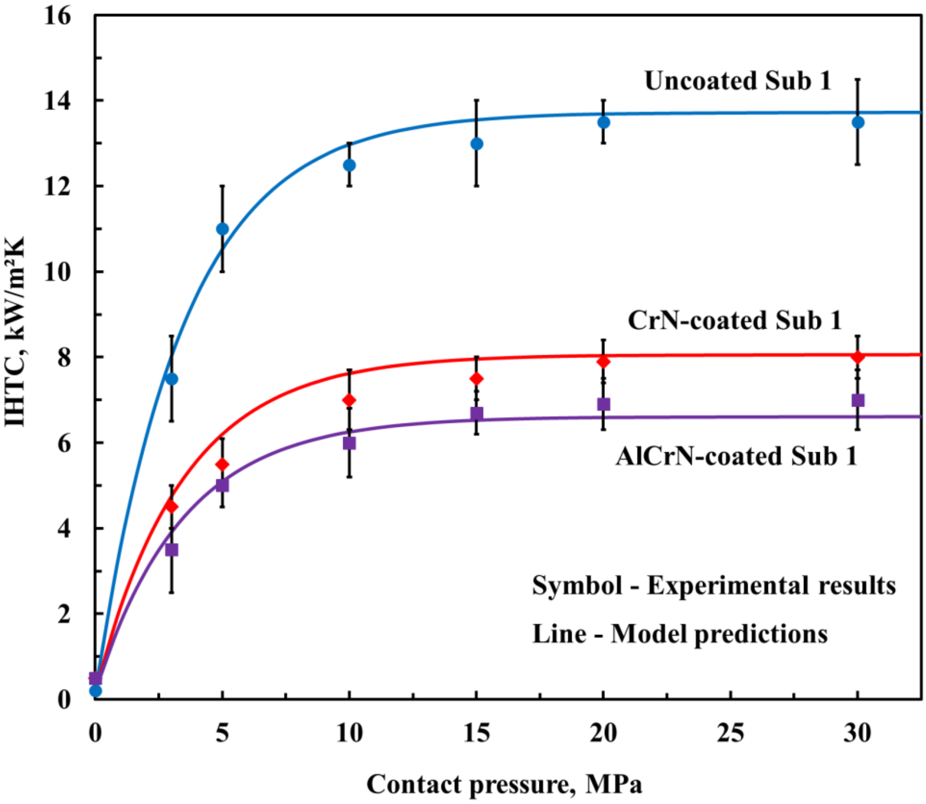

Fig. 4.3. Experimental IHTC evolutions with contact pressure for AA7075 using uncoated, CrN, and AlCrN-coated Substrate 1.

It was found that the IHTC evolution trend when using AlCrN-coated Substrate 1, i.e. a sharp increase at the initial stage, followed by a plateau at high contact pressures, was similar to that when using Substrate 1 uncoated, although the IHTC values were significantly lower. Due to the thermal conductivity of the AlCrN coating (0.0028 kW/mK) being considerably lower than that of Substrate 1 (0.0315 kW/mK), the heat transfer across the coating layer was dramatically reduced, and thus the IHTC values were substantially decreased.

When CrN-coated Substrate 1 was used, the IHTC increased at the initial stage and reached a peak IHTC value of 8 kW/m^{2}K when the contact pressure was larger than 15 MPa. This peak value was still much less than that when using Substrate 1 uncoated; however, it was approximately 14% larger than that when using AlCrN-coated Substrate 1. The IHTC values determined at different contact pressures when using uncoated, CrN and AlCrN-coated Substrate 1 are shown in Fig. 4.4. Compared to those when using uncoated Substrate 1, the IHTC values at different contact pressures when using AlCrN and CrN-coated Substrate 1 were averagely decreased by 50% and 42% respectively.

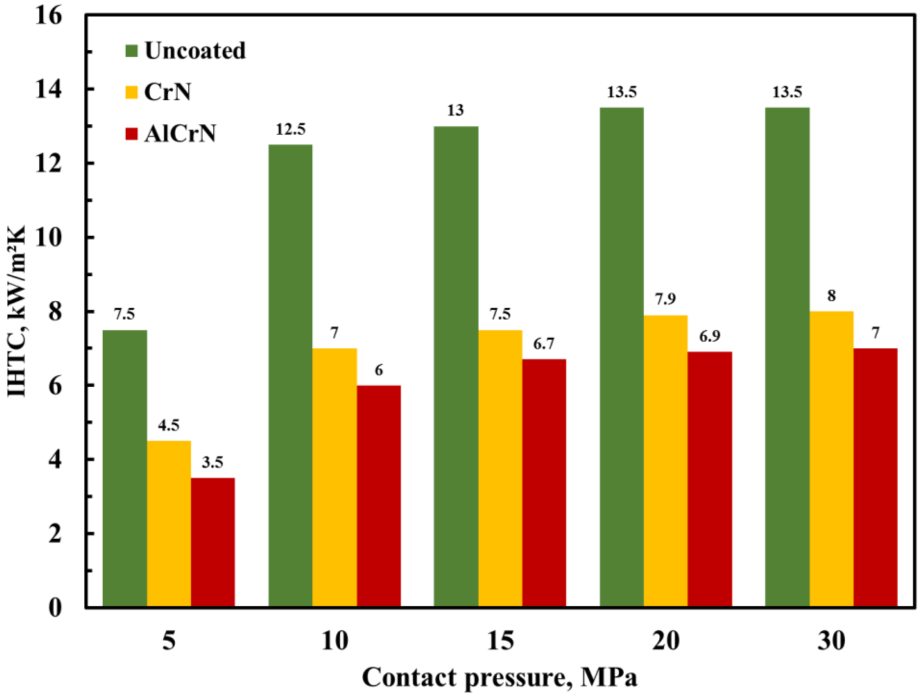

Fig. 4.4. Comparison of the IHTC values when using uncoated, CrN and AlCrN-coated Substrate 1.

Due to the thermal conductivity of the CrN coating (0.012 kW/mK) being larger than that of the AlCrN coating (0.0028 kW/mK), the heat transfer across the CrN coating layer was faster than that across the AlCrN coating layer, resulting in the larger IHTC values. The thermal conductivity of the coating was vital to its thermal performance on the IHTC.

The effect of the same coating deposited onto the different substrates on the IHTC was subsequently investigated. When AlCrN-coated Substrate 2 was used, the IHTC increased from 0.5 kW/m^{2}K at 0 MPa to 7 kW/m^{2}K at 10 MPa, as shown in Fig. 4.5. When the contact pressure was larger than 15 MPa, the IHTC converged to an approximate value of 7.8 kW/m^{2}K, which was 38% less than when using Substrate 2 uncoated (12.5 kW/m^{2}K). This amount of decrease in the peak IHTC value was lower than that caused by the application of the AlCrN coating onto Substrate 1 (48%). Due to the coating thickness of AlCrN-coated Substrate 2 (2 μm) being smaller than that of AlCrN-coated Substrate 1 (3 μm), the heat transfer occurred over a shorter distance for the AlCrN coating deposited onto Substrate 2, and thus the IHTC was reduced less than for the coating deposited onto Substrate 1.

In addition, when the CrN coating was applied onto Substrate 2, the peak IHTC value was decreased by 31% from 12.5 to 8.6 kW/m^{2}K, which was also lower than that caused by the application of the CrN coating onto Substrate 1 (41%), as shown in Fig. 4.6. This was also due to the coating thickness of CrN-coated Substrate 2 (3 μm) being smaller than that of CrN-coated Substrate 1 (6 μm). This indicated that the application of the same coating onto different substrates contributed to different thermal performances and hence influences on the IHTC due to their different thicknesses. In the present research, as the coatings had lower thermal conductivities than the tools, they influenced the IHTC negatively, decreasing the IHTC values with increasing coating thickness.

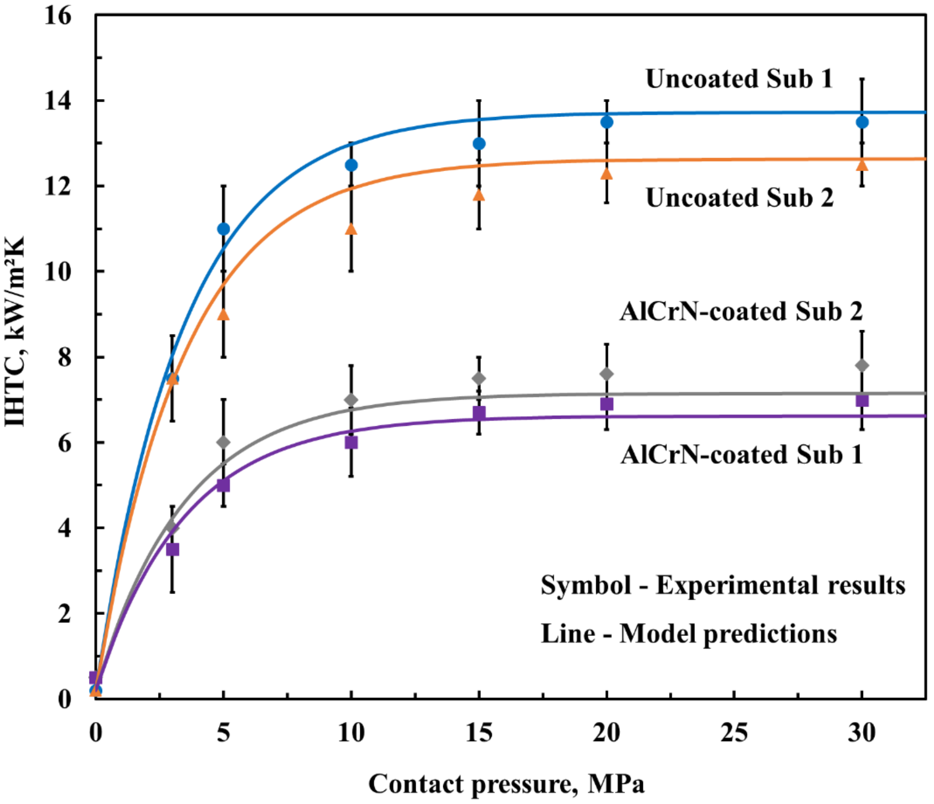

Fig. 4.5. Experimental IHTC evolutions with contact pressure for AA7075 using uncoated/AlCrN-coated Substrate 1 and 2.

Compared to those using uncoated Substrate 2, the IHTC values were decreased averagely by 36% and 28% at different contact pressures when using AlCrN-coated Substrate 2 and CrN-coated Substrate 2 respectively, as shown in Fig. 4.7. The percentage decreases in the IHTC caused by the deposition of the AlCrN and CrN coatings onto Substrate 2 were lower than those caused by the deposition of the same coatings onto Substrate 1. This once again proved that the effect of the tool coatings on the IHTC was enhanced with increasing coating thickness.

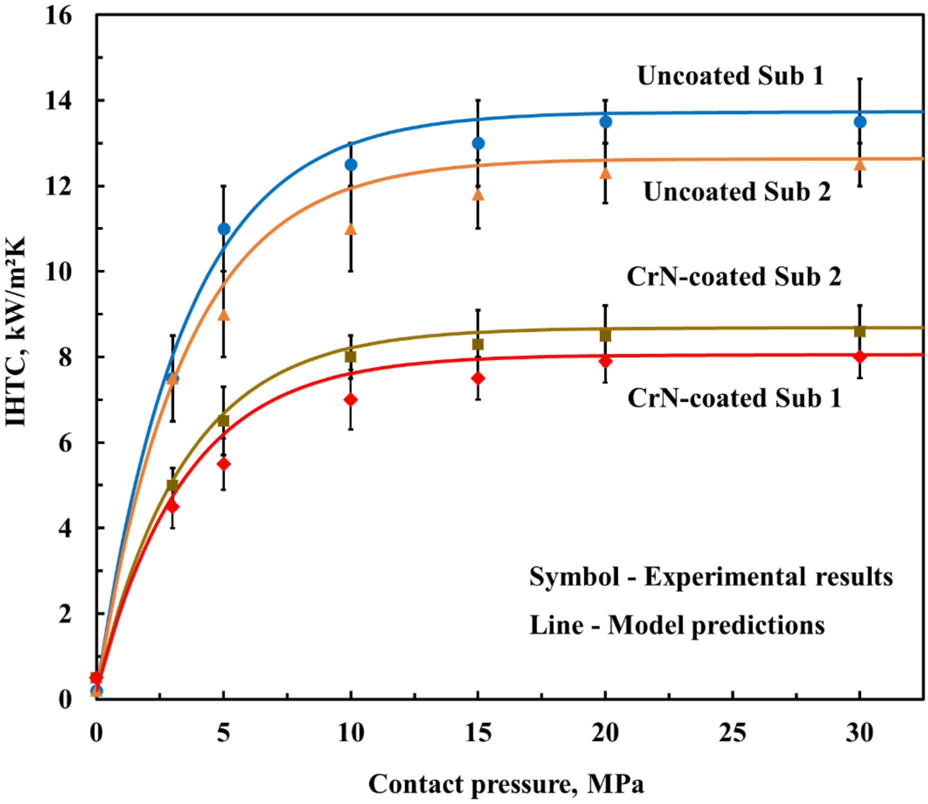

Fig. 4.6. Experimental IHTC evolutions with contact pressure for AA7075 using uncoated/CrN-coated Substrate 1 and 2.

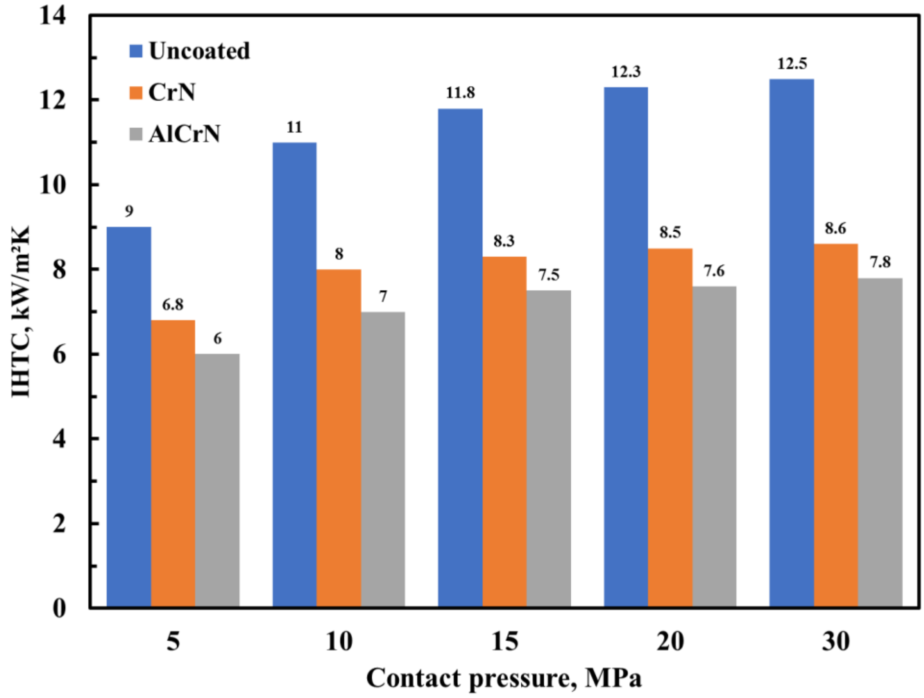

Fig. 4.7. Comparison of the IHTC values when using uncoated, AlCrN and CrN-coated Substrate 2.

In order to expand the investigation on the effect of the tool coatings, further IHTC tests were conducted using TiN-coated Substrate 3. As shown in Fig. 4.8, the IHTC increased from 0.5 to 8 kW/m^{2}K when the contact pressure increased from 0 to 10 MPa and reached a peak value of 9 kW/m^{2}K after 15 MPa. Due to the thermal conductivity of the TiN coating (0.019 kW/mK) being slightly smaller than that of Substrate 3 (0.0219 kW/mK), the peak IHTC value was decreased by only 10% compared to that when using Substrate 3 uncoated (10 kW/m^{2}K).

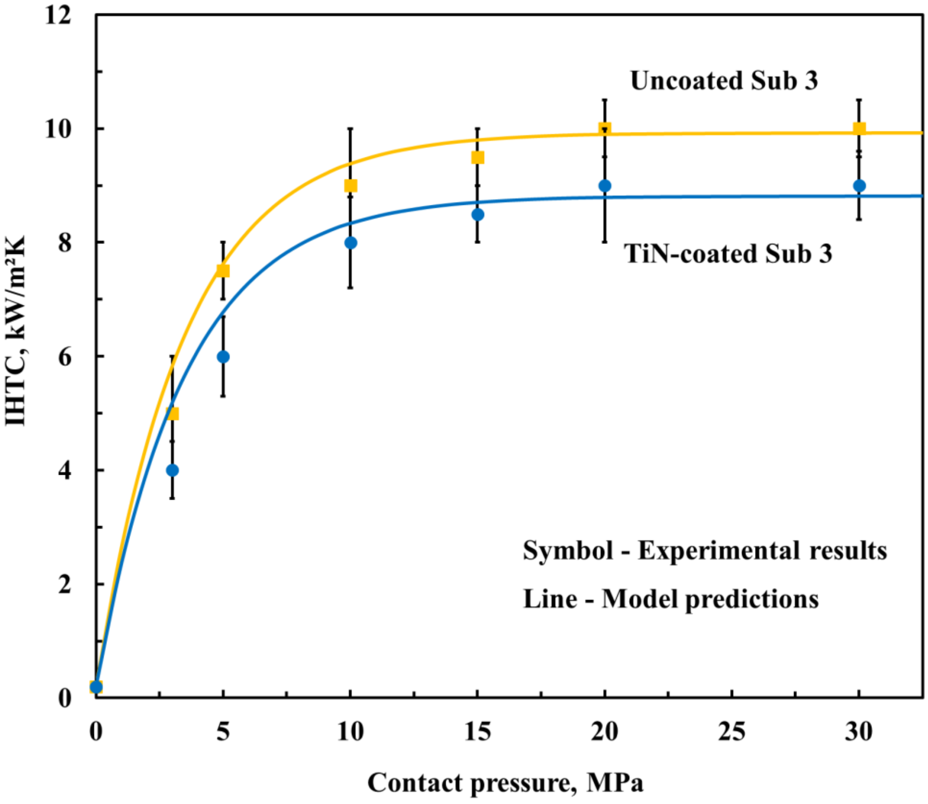

Fig. 4.8. Experimental IHTC evolutions with contact pressure for AA7075 using uncoated and TiN-coated Substrate 3.

According to the IHTC model stated in Chapter 5, the coating thermal performance and its effect on the IHTC values can be represented by the term $\delta_c \cdot \ln(k_c/k_t)$, where δ_c is the coating thickness, and k_c and k_t are thermal conductivities of coating and substrate (tool) respectively. As shown in Table 4.1, the value of this term for AlCrN-coated Substrate 1 was the smallest (-7.3), leading to the largest percentage decrease in the peak IHTC value (48%). The value of the term for TiN-coated Substrate 3 was the largest (-1.1), leading to the smallest percentage decrease in the peak IHTC value (10%). This indicated that the thermal conductivity ratio of the coating to the substrate as well as the coating thickness determined the coating thermal performance and can be either a positive or negative effect on the IHTC. These results could be used to guide the tool design and material selection in a hot stamping process. Coatings with lower thermal conductivities, e.g. AlCrN and CrN, can be applied onto blankholders to prevent the temperature of the blank from decreasing rapidly, thus maintaining good material drawability during forming, whilst those with high thermal conductivities, e.g. TiN, can be applied onto punches and dies to reduce tool wear and meanwhile provide high IHTC values, thus achieving the required critical cooling rates. The coatings used in the present research are hard ones. The effect of the soft coatings on the IHTC will be a topic of future work.

Table 4.1. Coating thermal performances

	AlCrN	CrN	TiN
$\delta_c \cdot \ln(k_c/k_t)$ (Sub 1)	-7.3	-5.8	---
$\delta_c \cdot \ln(k_c/k_t)$ (Sub 2)	-5.6	-4.3	---
$\delta_c \cdot \ln(k_c/k_t)$ (Sub 3)	---	---	-1.1
Decrease in the peak IHTC (Sub 1)	48%	41%	---
Decrease in the peak IHTC (Sub 2)	38%	31%	---
Decrease in the peak IHTC (Sub 3)	---	---	10%

4.4 Effect of specimen thickness on the IHTC

AA6082 specimens with three different thicknesses and P20 tools were used in this section to study the effect of the specimen thickness on the IHTC. The material properties of the P20 tools are shown in Table 3.1. The overall evolutions of the IHTC for the 2, 3 and 5 mm thick AA6082 specimens under dry conditions were also found to follow a similar trend, i.e. a sharp increase at the initial stage, followed by a plateau at high contact pressures, as shown in Fig. 4.9. The IHTC for the 3 mm thick specimens increased considerably from 1.4 to 16.5 kW/m^{2}K when the contact pressure increased from 0 to 20 MPa under dry conditions, followed by a moderate increase as the contact pressure increased from 20 to 25 MPa. When the contact pressure was larger than 25 MPa, a plateau of the IHTC was observed, at a value of approximately 17.5 kW/m^{2}K. The IHTC for the 2 mm thick specimen increased dramatically from 1.4 kW/m^{2}K at 0 MPa to 12 kW/m^{2}K at 20 MPa. When the contact pressure reached 25 MPa, the IHTC converged to a value of approximately 13.5 kW/m^{2}K. A 1 mm increase in the specimen thickness led to an approximately 30% increase of the IHTC values at different contact pressures, as shown in Table 4.2. Compared to that for the 3 mm thick specimen, the IHTC plateau value for the 5 mm thick specimen was increased by 20%, reaching approximately 21 kW/m^{2}K when the contact pressure was larger than 25 MPa.

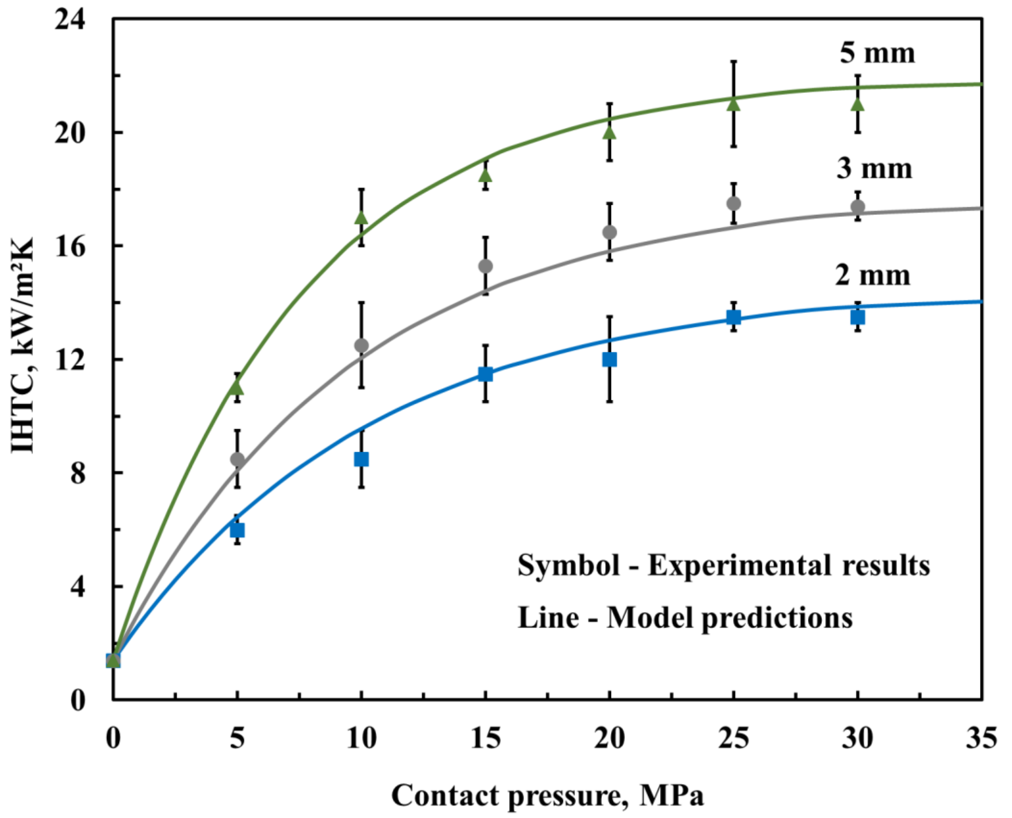

Fig. 4.9. Experimental IHTC evolutions with contact pressure for AA6082 specimens with different thicknesses when using P20 tools.

The percentage increases in the IHTC were between 30% and 47% at different contact pressures with an average increase of 39% when the specimen thickness increased from 2 to 3 mm, whilst those were between 20% and 36% at different contact pressures with an average increase of 26% when the specimen thickness increased from 3 to 5 mm, as shown in Table 4.2. This indicated that the IHTC increased with increasing specimen thickness; however, its amount of increase was reduced.

Table 4.2. The IHTC for AA6082 with different thicknesses at different contact pressures

Contact pressure (MPa)	5	10	20	25	30
IHTC for 2 mm thick AA6082 (kW/m^2K)	6	8.5	12	13.5	13.5
IHTC for 3 mm thick AA6082 (kW/m^2K)	8.5	12.5	16.5	17.5	17.4
Increase in the IHTC from 2 to 3 mm	42%	47%	38%	30%	29%
IHTC for 5 mm thick AA6082 (kW/m^2K)	11	17	20	21	21
Increase in the IHTC from 3 to 5 mm	30%	36%	21%	20%	21%

The thermal conditions at the contact interface did not actually vary with increasing specimen thickness for the same target temperature and contact pressure during the experiments. However, due to the larger internal thermal energy being stored in the thicker specimens, an engineering IHTC could be defined that increased with increasing specimen thickness, describing the equivalent heat transfer coefficient at the contact interface; while the true IHTC, defined at the contact interface, would not change. Although the specimen thickness has no effect on the true IHTC at the interface, the engineering IHTC affected by the specimen thickness would be required for accurately predicting the temperature evolutions of specimens with different thicknesses in simulations of hot stamping processes.

4.5 Effect of lubricant on the IHTC

When a graphite lubricant was applied onto the surfaces of the tools with a 20 μm thickness, the overall evolutions of the IHTC for both 2 and 3 mm thick AA6082 specimens followed logarithmic increasing trends. As shown in Fig. 4.10, the IHTC for the 3 mm thick specimen increased dramatically from 3 kW/m^2K at 0 MPa to 20.5 kW/m^2K at 20 MPa, using P20 tools. When the contact pressure reached 25 MPa, the IHTC converged to a value of approximately

21 kW/m^{2}K. The large difference in the IHTC at 0 MPa under lubricated conditions between the experimental and predicted results will be improved in future work.

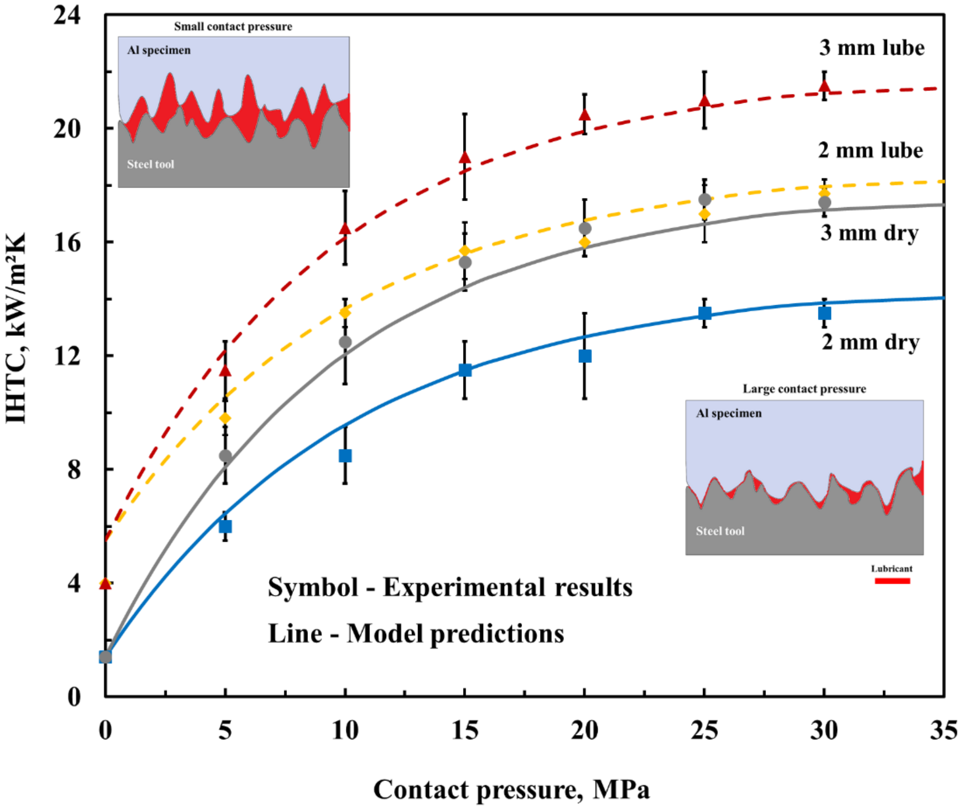

Fig. 4.10. Experimental IHTC evolutions with contact pressure for the 2 and 3 mm thick AA6082 specimens under dry and lubricated conditions using P20 tools.

The application of the graphite lubricant increased the IHTC values for both 2 and 3 mm thick AA6082 specimens at different contact pressures, compared to those under dry conditions. This was due to the thermal conductivity of the graphite lubricant being approximately 0.024 kW/mK, which is much higher than that of the air; thus, the heat transfer was much more rapid when the lubricant filled up the vacancies of the asperities at the contact interface.

The IHTC for the 2 mm thick AA6082 specimens was increased by approximately 63% at a contact pressure of 5 MPa when the graphite lubricant was applied. However, the percentage increase in the IHTC decreased from 63% to 21% when the contact pressure increased from 5 to 25 MPa, as shown in Table 4.3. A similar decreasing trend of the percentage increase in the IHTC with contact pressure was also observed when using the 3 mm thick AA6082 specimens, in which the percentage increase in the IHTC decreased from 35% to 20% when the contact pressure increased from 5 to 25 MPa. This indicated that the effect of the lubricant on the IHTC was reduced with increasing contact pressure. When the contact pressure reached its convergent value, the application of the graphite lubricant raised the peak IHTC values for both 2 and 3 mm thick AA6082 specimens by approximately 20%, compared to those under dry conditions. It was therefore deduced that the lubricant mechanism is independent of the specimen thickness in its effect on the IHTC at high contact pressures.

Table 4.3. The IHTC values for the 2 and 3 mm thick AA6082 specimens at different contact pressures under dry and lubricated conditions.

Contact pressure (MPa)	5	10	15	20	25
IHTC for 2 mm thick AA6082 under dry conditions (kW/m^2K)	6	8.5	11.5	12	13.5
IHTC for 2 mm thick AA6082 under lube conditions (kW/m^2K)	9.8	13.5	15.7	16	17
Increase in the IHTC from dry to lube	63%	59%	37%	33%	21%
IHTC for 3 mm thick AA6082 under dry conditions (kW/m^2K)	8.5	12.5	15.3	16.5	17.5
IHTC for 3 mm thick AA6082 under lube conditions (kW/m^2K)	11.5	16.5	19	20.5	21
Increase in the IHTC from dry to lube	35%	32%	24%	24%	20%

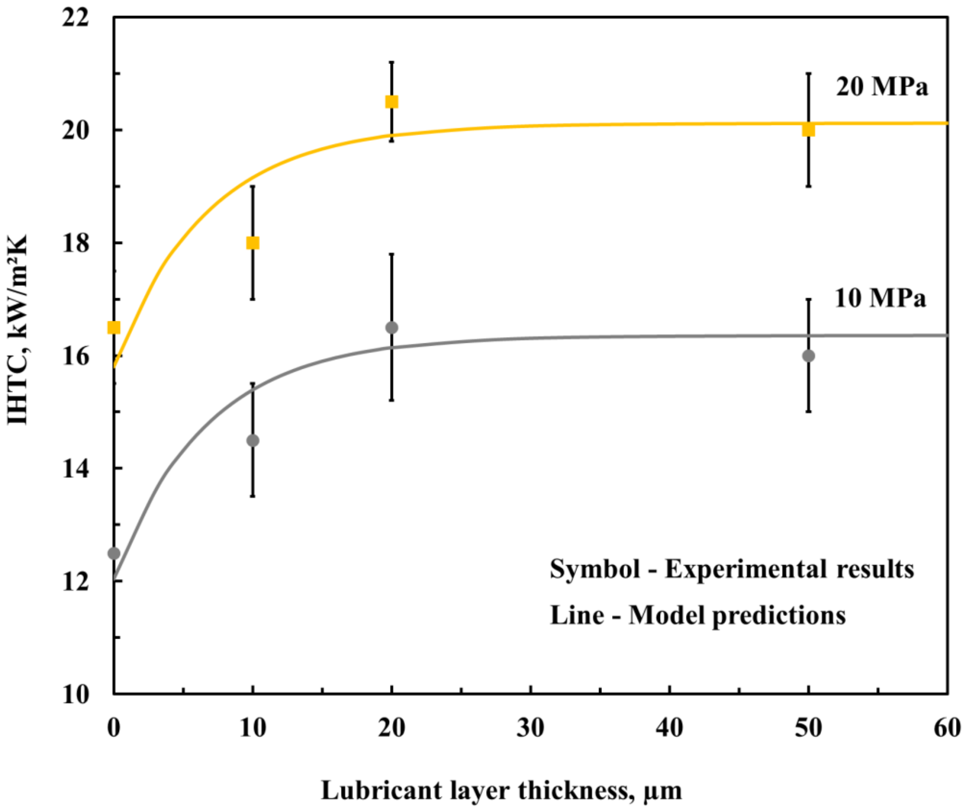

Fig. 4.11. Experimental IHTC evolutions with lubricant layer thickness for AA6082 at different contact pressures using P20 tools.

The evolutions of the IHTC for the 3 mm thick specimen were also determined as a function of the applied lubricant layer thickness at different contact pressures, as shown in Fig. 4.11. When the contact pressure was 10 MPa, the IHTC increased from 12.5 to 16.5 kW/m^{2}K when the lubricant layer thickness increased from 0 to 20 µm. The IHTC then remained stable when the lubricant layer thickness was larger than 20 µm. A similar trend of the IHTC evolution was observed when the contact pressure was 20 MPa, i.e. as the lubricant layer thickness increased, there was a steep increase followed by a plateau of the IHTC.

When more lubricant filled up the vacancies at the contact interface, the heat was transferred and dissipated more rapidly, leading to larger IHTC values. However, excessive lubricant was squeezed out of the contact interface by the tools when the layer thickness of 20 µm was reached at different contact pressures, leading to the converged IHTC values. This indicated that 20 µm is the maximum effective lubricant layer thickness in this case.

By comparison, the peak IHTC value for AA7075 was increased by approximately 39% from 15.6 to 21.7 kW/m^{2}K when the graphite lubricant was applied, which was larger than that for

AA6082 (26%), as shown in Fig. 4.12. Meanwhile, the maximum effective lubricant layer thickness was approximately 15 µm, which was slightly lower than that for AA6082 (20 µm), as shown in Fig. 4.13. It was found that the initial surface roughness of the AA7075 specimen (340 nm) was smaller than that of the AA6082 specimen (430 nm). It was therefore deduced that the effect of the lubricant on the IHTC is reduced with increasing initial surface roughness of the specimen and tools, while the maximum effective lubricant layer thickness is increased, as more lubricant is required to fill the larger vacancies of the asperities at the contact interface for higher surface roughnesses. Dedicated equipment able to apply the lubricant thickness with ultra-precise control is required to improve the quality of the lubricant thickness study in future work.

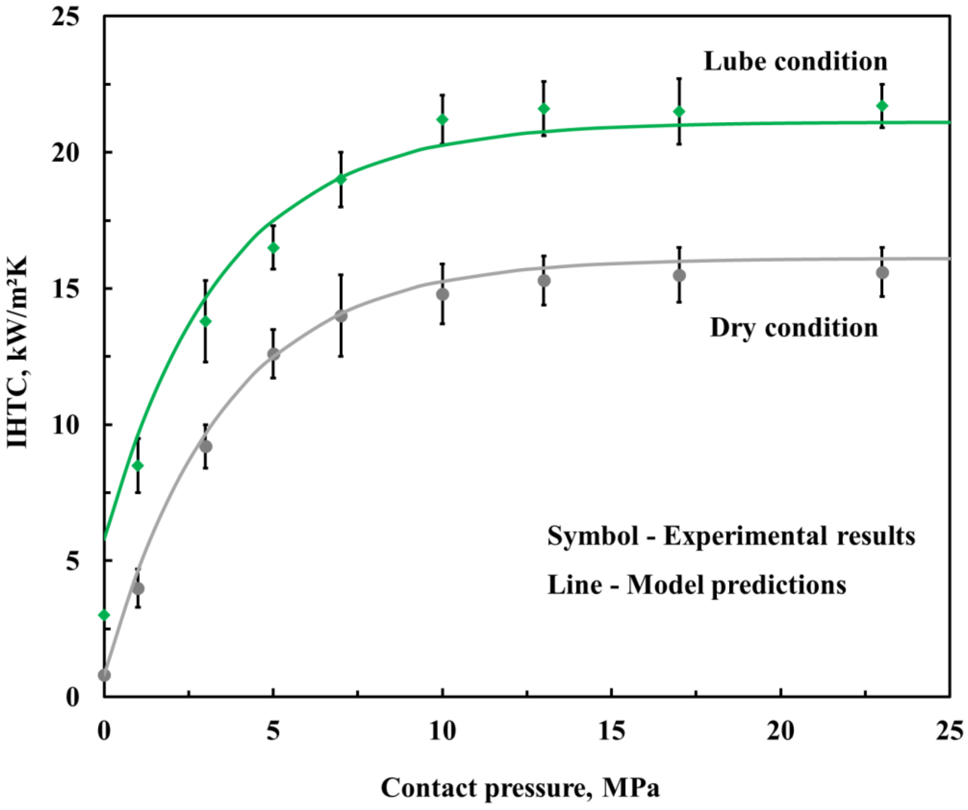

Fig. 4.12. Experimental IHTC evolutions with contact pressure for AA7075 under dry and lubricated conditions using cast-iron G3500 tools.

In addition, the percentage increase in the IHTC for AA7075 caused by the application of the graphite lubricant also decreased from 50% to 39% when the contact pressure increased from 3 to 23 MPa, as shown in Table 4.4. This once again proved that the effect of lubricant on the IHTC was reduced with increasing contact pressure and became stable when the contact pressure reached its convergent value.

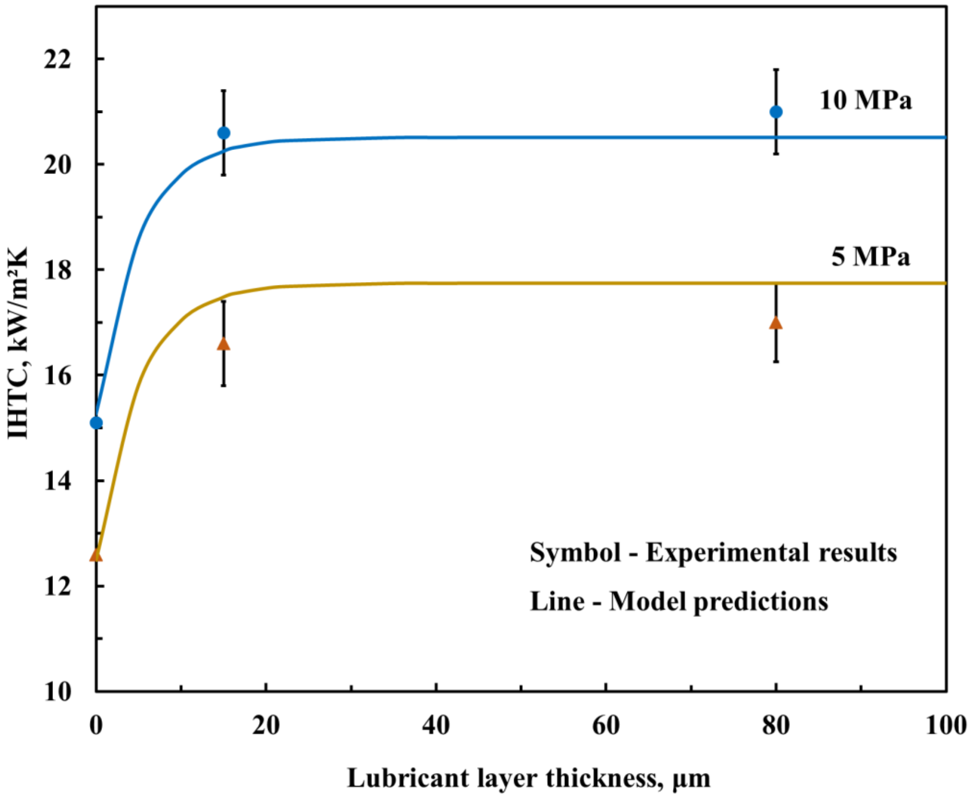

Fig. 4.13. Experimental IHTC evolutions with lubricant layer thickness for AA7075 at different contact pressures using cast-iron G3500 tools.

Table 4.4. The IHTC for AA7075 under dry and lubricated conditions

Contact pressure (MPa)	IHTC under dry conditions (kW/m^{2}K)	IHTC under lube conditions (kW/m^{2}K)	Increase in the IHTC
3	9.2	13.8	50%
10	14.8	21.2	43%
13	15.3	21.6	41%
17	15.5	21.5	39%
23	15.6	21.7	39%

4.6 Effect of initial blank temperature on the IHTC

According to different hot and warm stamping technologies, three initial blank temperatures of 350˚C, 420˚C and 470˚C were applied in this section to determine the IHTC values for AA7075 to identify the effect of the initial blank temperature on the IHTC. A pair of uncoated/coated punch and die supplied by the 'Low Cost Materials Processing Technologies for Mass Production of Lightweight Vehicles (LoCoMaTech)' project was bolted onto pedestals. The substrate material of the tools was a D6510 cast-iron, and their contact surface areas were 50 x 25 mm^2, onto which a tungsten carbide (WC) coating with a layer thickness of 2 µm was deposited for one set of tools. The average surface roughness (Ra) of the tool surfaces, measured using White Light Interferometry equipment (Wyko NT 9100), was approximately 180 nm for both the uncoated and coated tools, eliminating the effect of the coating surface roughness on the IHTC.

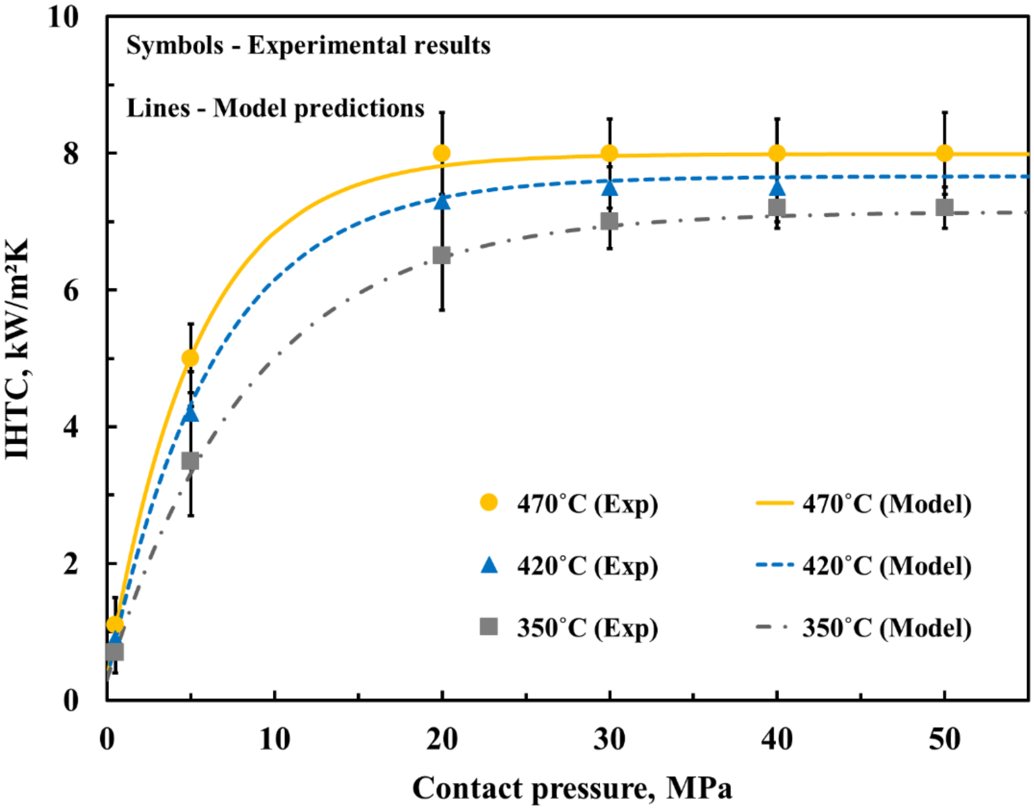

Fig. 4.14. Experimental and predicted IHTC evolutions for AA7075 with contact pressure at different initial blank temperatures, when using WC-coated D6510 tools.

As shown in Fig. 4.14, the trends of the IHTC evolutions as a function of contact pressure were similar at different initial blank temperatures, i.e. a rapid increase at the initial stage followed by a plateau at higher contact pressures. However, the IHTC was found to increase with increasing initial blank temperature, and their convergent contact pressure values were different. The effects of the WC coating and initial blank temperature on the IHTC are analysed in the following sections.

4.6.1 Effect of the WC coating on the IHTC at different initial blank temperatures

When the WC-coated tools were used, the IHTC for AA7075 increased significantly from 0.7 to 7 kW/m^{2}K when the contact pressure increased from 0.5 to 30 MPa at an initial blank temperature of 350˚C, as shown in Fig. 4.15. The IHTC values increased when uncoated tools were used at the same initial blank temperature. At an initial blank temperature of 470˚C, the IHTC for AA7075 increased dramatically from 1.1 kW/m^{2}K at 0.5 MPa to 7.7 kW/m^{2}K at 20 MPa, followed by a plateau of the IHTC at higher contact pressures, when using the WC-coated tools.

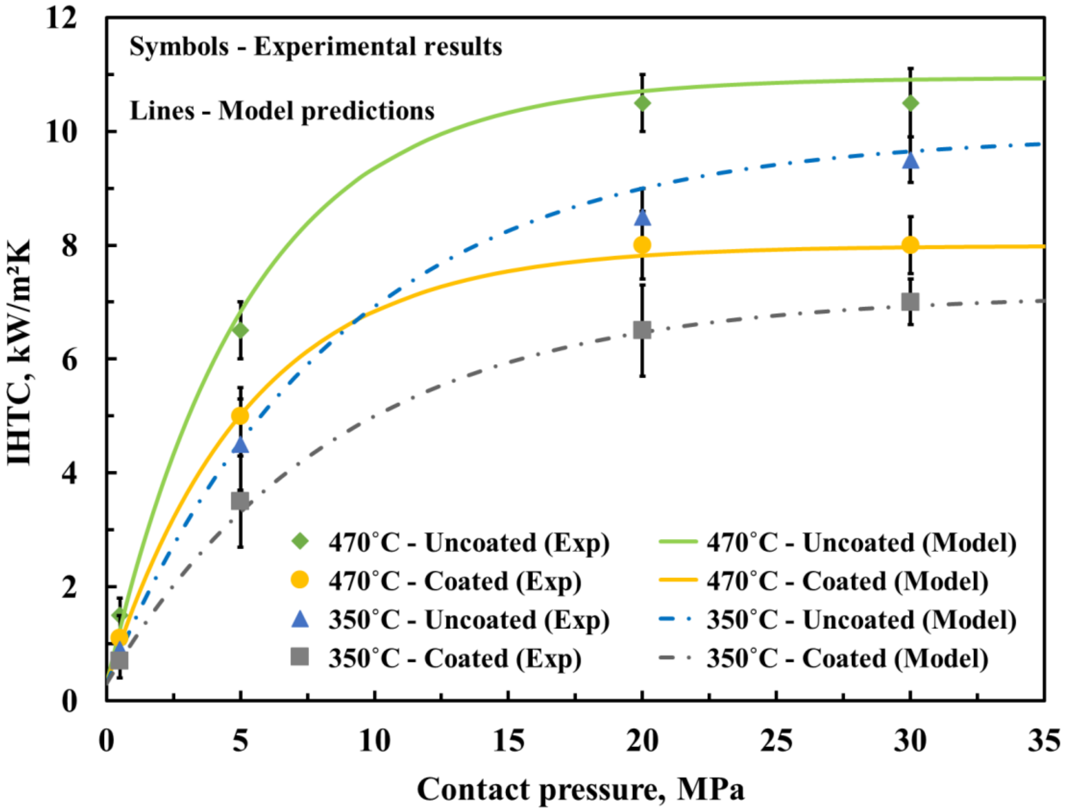

Fig. 4.15. Experimental and predicted IHTC evolutions for AA7075 with contact pressure at initial blank temperatures of 350˚C and 470 ˚C, when using uncoated and coated D6510 tools.

A similar increase in the IHTC was also found when uncoated tools were used at the same initial blank temperature. As mentioned before, due to the thermal conductivity of the WC coating (292 W/mK) being lower than that of the D6510 substrate (353 W/mK), the heat transfer across the coating layer was consequently reduced, resulting in lower IHTC values. Therefore, the application of tool coatings with the thermal conductivities lower than those of the substrates could reduce the IHTC, which has also been deduced in previous research.

As shown in Table 4.5, when the contact pressure was 0.5 MPa, the IHTC values were decreased by approximately 22.2% and 26.7% due to the application of the WC coating at initial blank temperatures of 350˚C and 470˚C respectively. Furthermore, it was found that the amount of decrease in the IHTC caused by the WC coating was always between 22% and 27%, with an average value of 24%, at different initial blank temperatures and contact pressures. This indicated that the thermal properties of the WC coating, particularly its thermal conductivity, were negligibly changed when the initial blank temperature increased from 350˚C to 470˚C. Therefore, the effect of the tool coating on the IHTC was consistent for different initial blank temperatures and did not cause the variation in the IHTC at different initial blank temperatures.

Table 4.5. Decreases in the IHTC due to the application of the WC coating

350˚C			
Pressure (MPa)	**IHTC (Uncoated)** (kW/m^{2}K)	**IHTC (Coated)** (kW/m^{2}K)	**Decrease in the IHTC** %
0.5	0.9	0.7	22.2%
5	4.5	3.5	22.2%
20	8.5	6.5	23.5%
30	9.5	7	26.3%
470 ˚C			
Pressure (MPa)	**IHTC (Uncoated)** (kW/m^{2}K)	**IHTC (Coated)** (kW/m^{2}K)	**Decrease in the IHTC** (%)
0.5	1.5	1.1	26.7%
5	6.5	5	23.1%
20	10.5	8	23.8%
30	10.5	8	23.8%

4.6.2 Effect of material strength on the IHTC at different initial blank temperatures

The IHTC was decreased by 18.2% at a contact pressure of 0.5 MPa when the initial blank temperature was reduced from 470˚C to 420˚C, as shown in Table 4.6. However, the amount of decrease in the IHTC decreased with increasing contact pressure and reached a constant value of 6.3% when the contact pressure was larger than the convergent value of 30 MPa. Similarly, when the initial blank temperature decreased from 470˚C to 350˚C, the amount of decrease in the IHTC decreased from 36.4% at 0.5 MPa to 12.5% at 30 MPa and reached a constant value of 10% after the convergent contact pressure of 40 MPa. It was found that the effect of the initial blank temperature on the IHTC was reduced with increasing contact pressure and became constant when the convergent contact pressure was reached. The effect of the initial blank temperature on the IHTC could therefore be categorised into two stages dominated by two mechanisms respectively.

Table 4.6. Decreases in the IHTC due to the decreasing initial blank temperature

Pressure (MPa)	**IHTC (470˚C)** (kW/m²K)	**IHTC (420˚C)** (kW/m²K)	**IHTC decrease** (470 to 420˚C)	**IHTC (350˚C)** (kW/m²K)	**IHTC decrease** (470 to 350˚C)
0.5	1.1	0.9	18.2%	0.7	36.4%
5	5	4.2	16%	3.5	30%
20	8	7.3	8.8%	6.5	18.8%
30	8	7.5	6.3%	7	12.5%
40	8	7.5	6.3%	7.2	10%
50	8	-	-	7.2	10%

The material strength of aluminium alloys decreased with increasing initial blank temperature, as shown in Fig. 4.16. Therefore, the fracture of the asperities on the specimen surface increased with increasing initial blank temperature at the same contact pressure, resulting in a larger real contact area and thus a higher IHTC between the specimen and tools. However, the convergent contact pressure value decreased with increasing initial blank temperature due to the achievement of the peak contact area at a lower contact pressure.

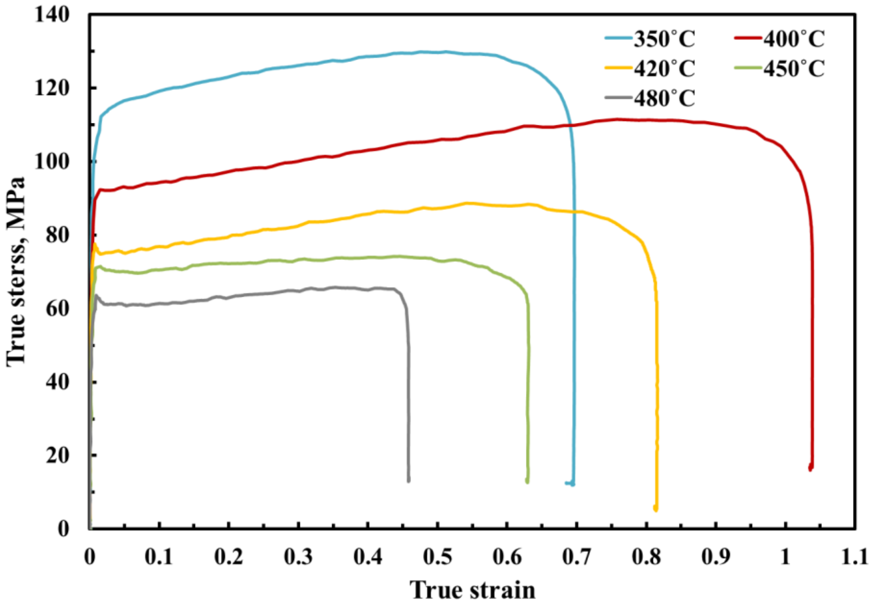

Fig. 4.16. Hardening curves of AA7075 at elevated temperatures.

In order to represent the specimen surface condition after compression, its average post-form surface roughness (Ra) under different experimental conditions was measured. The initial surface roughnesses of the specimen and tool (WC-coated tools from LoCoMaTech in this section) were 390 and 180 nm respectively. As shown in Fig. 4.17, when the initial blank temperature was 350°C, the post-form surface roughness of the specimen decreased from 378 nm at 0.5 MPa to 226 nm at its convergent contact pressure of 40 MPa, approaching that of the tool. When the initial blank temperature was 420°C, the post-form surface roughness of the specimen was 354 nm at a contact pressure of 0.5 MPa and decreased to 230 nm when the convergent contact pressure of 30 MPa was reached, while it decreased from 312 to 231 nm when the contact pressure increased from 0.5 MPa to its convergent value of 20 MPa at an initial blank temperature of 470°C.

From these results, it could be deduced that the post-compression surface roughness of the specimen was lower at a higher initial blank temperature when the same contact pressure was applied, representing a better mesh and thus a larger real contact area between the specimen and tools. When the convergent contact pressure was reached, the post-form compression surface roughness of the specimen was close to that of the tools at different initial blank temperatures. Therefore, the material strength of the specimen at different initial blank temperatures affected the IHTC before the convergent contact pressure was reached. However, this effect reduced with increasing contact pressure and became negligible at the convergent contact pressure. This section shows a case that the surface roughness of the specimen is larger than that of the tools.

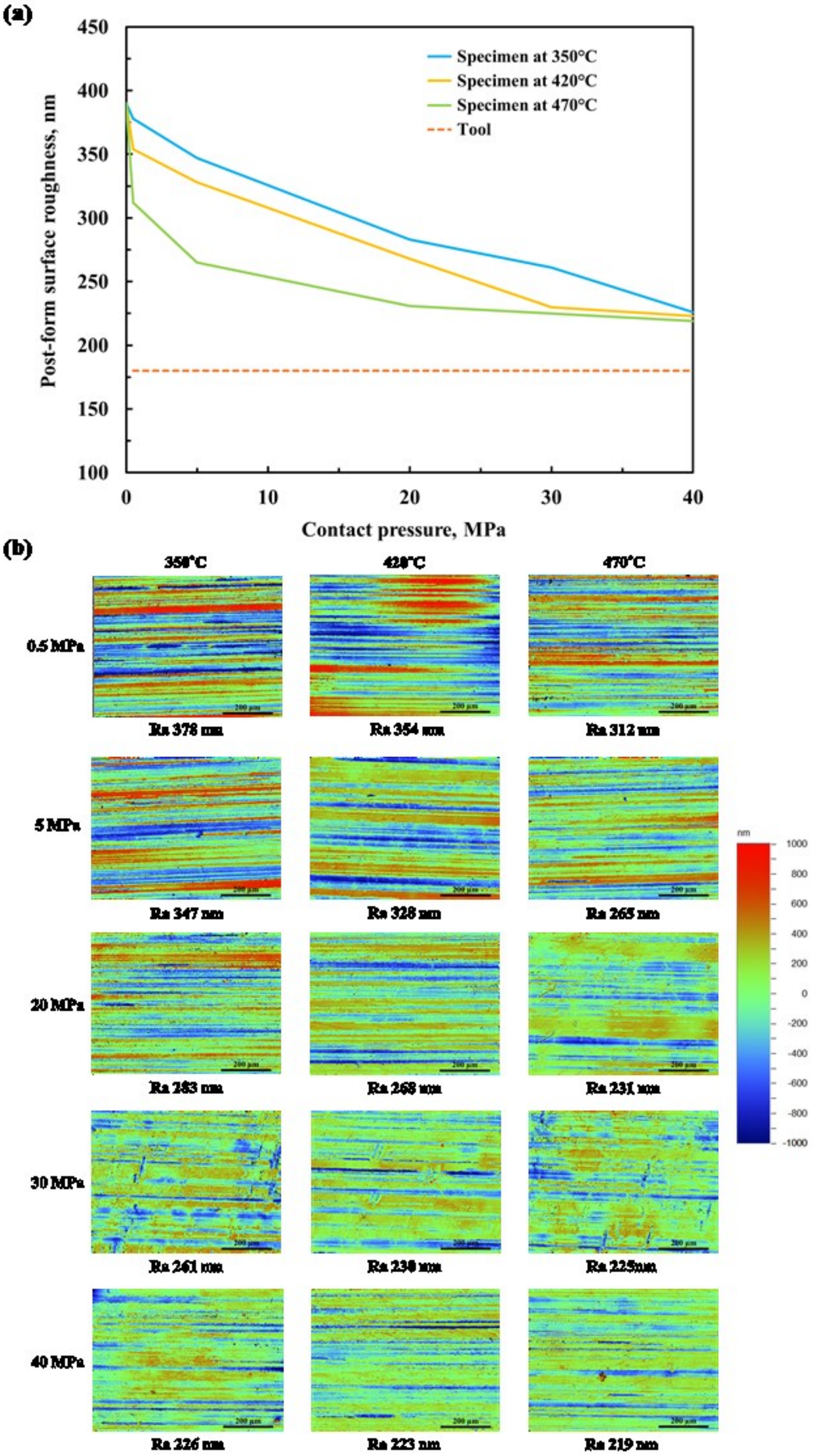

Fig. 4.17. (a) Post-form surface roughness evolution of the specimen as a function of contact pressure at different initial blank temperatures; (b) White light interferometry scanned post-form surface roughness of the specimen under different experimental conditions.

The differences in the IHTC at different initial blank temperatures were caused by the variations in the thermal properties of the specimen after the convergent contact pressure was reached. The thermal conductivity and specific heat capacity of the specimen decreased with decreasing initial blank temperature, thus reducing the heat transfer between the specimen and tools. It has been proven that the specific heat capacity of the specimen has a negligible effect on the IHTC [23]. Therefore, the variation in the thermal conductivity of the specimen resulted in different IHTC values. When the initial blank temperature decreased from 470˚C to 420˚C, the thermal conductivity of the specimen was decreased by 2% from 158 to 155 W/mK. The IHTC was consequently decreased by approximately 6.3%, as shown in Table 4.6. Additionally, a decrease from 470°C to 350°C in the initial blank temperature caused a decrease of 5% from 158 to 150 W/mK in the thermal conductivity of the specimen, leading to a decrease of 10% in the IHTC.

Hence, the effect of the initial blank temperature on the IHTC was composed of two mechanisms; the effects of the material strength and thermal conductivity. When the contact pressure was lower than its convergent value, the material strength of the specimen was the leading mechanism, but once the convergent contact pressure was reached, the variation in the thermal conductivity of the specimen became the dominant mechanism affecting the IHTC.

4.7 Summary

The IHTC values for 7075 and 6082 aluminium alloys were determined under different experimental conditions, and the effects of the contact pressure, tool material, coating material, specimen thickness, lubricant and initial blank temperature on the IHTC were subsequently studied.

- The IHTC evolutions with contact pressure for different aluminium alloys were found to be similar, i.e. a sharp increase at the initial stage, followed by a plateau when the contact pressure was larger than its convergent value.
- The IHTC values were increased by the application of the tools with higher thermal conductivities, due to the heat transfer occurring at higher rates across the tools.
- In contrast, when the coatings with lower thermal conductivities than those of the tools (substrates) were applied, the IHTC values were decreased correspondingly. Furthermore, the coating thickness and thermal conductivity of the coating determined the coating thermal performance and its effect on the IHTC.

- It was also found that the IHTC increased with increasing specimen thickness, due to the larger internal thermal energy being stored in the thicker specimen.
- The application of the lubricants with higher thermal conductivities could also raise the IHTC values, due to the lubricant filling up the vacancies of the asperities at the contact interface. In addition, the IHTC increased with increasing lubricant layer thickness before reaching the maximum effective lubricant layer thickness.
- The effect of the initial blank temperature was consequently identified as a combination of two mechanisms; the effects of the material strength and thermal conductivity. The IHTC was affected by the strength of the specimen when the contact pressure was lower than its convergent value, i.e. the IHTC increased with decreasing material strength due to a larger fracture of the asperities occurring at a higher initial blank temperature. However, the effect of the material strength became negligible after the convergent contact pressure, while the increasing thermal conductivity of the specimen became the dominant mechanism, further increasing the IHTC values.

Chapter 5

A mechanism-based IHTC model[5]

Efforts have been made previously to predict the IHTC evolutions as a function of a particular influential factor, however, without a comprehensive study. Therefore, the development of a general model to predict the IHTC evolutions as a function of different influential factors, e.g. contact pressure, tool material, coating material, specimen thickness, lubricant and initial blank temperature is of great importance. Furthermore, the developed IHTC model enables the prediction of the interaction between the lubricant diminution and the IHTC with sliding time.

5.1 Development of a mechanism-based IHTC model

An overall IHTC model was developed by Çetinkale and Fishenden [50] as a sum of two independent parts, according to different heat transfer mechanisms. Based on their theory, the overall IHTC was assumed to be comprised of four mechanisms in the present research: the air-contact IHTC h_a, for when the contact pressure was zero and heat flow was mainly across the air gap between the specimen and tools, the solid-contact IHTC h_s, for when the contact pressure was applied and heat transfer across the contact surfaces dominated, the coating-contact IHTC h_c, for when a tool coating was applied to the tools (substrates),

---

[5] Chapter 5 was reproduced from two papers:

Liu, X., Zheng, Y., Fakir, O. El, Said, R., Wang, L., 2018. Characterisation of the contact pressure dependent interfacial heat transfer coefficient for a hot stamping process following a data driven approach, in: 5th International Conference on New Forming Technology (ICNFT2018).

Liu, X., Fakir, O. El, Gharbi, M. M., Wang, L., 2018. Effect of tool coating on interfacial heat transfer coefficient in hot stamping of AA7075 aluminium alloys. Procedia Manuf. 15, 1127-1133. doi:10.1016/j.promfg.2018.07.378

and heat transfer across the coating layer, and the lubricant-contact IHTC h_l, for when a lubricant was applied between the two contact surfaces, and more heat could be transferred and dissipated by a lubricant with a higher thermal conductivity.

The lubricant layer diminishes during sliding, leading to h_l decreasing, up to the point at which lubricant breakdown occurs, where h_l would not contribute to the overall IHTC any longer. Therefore, it is of great importance to model the interaction between the lubricant diminution and lubricant-contact IHTC h_l, and thus express h_l as a time-dependent variable, as shown in Eq. (5.1):

$$h = h_a + h_s + h_c + h_l(t) \tag{5.1}$$

It was found that the air-contact IHTC h_a did not play an essential role in the present research since the initial amount of heat transfer between the contact surfaces was negligible according to the experimental observations. Once a contact pressure was applied, the heat transfer between the contact surfaces was increased significantly. Thus, the overall IHTC was mainly characterised by the solid-contact IHTC h_s, the coating-contact IHTC h_c and the lubricant-contact IHTC $h_l(t)$. Therefore, it was reasonable to assume a constant value for the air-contact IHTC h_a, which was determined by running the IHTC tests under dry conditions with zero contact pressure. The solid-contact IHTC h_s, induced by the applied contact pressure, was modelled by Eq. (5.2):

$$h_s = \alpha_l \cdot \varphi(T) \cdot \frac{K_{st}}{R_{st}} N_P \tag{5.2}$$

where α_l is a specimen thickness-dependent parameter, $\varphi(T)$ is a temperature-dependent parameter, K_{st} is the harmonic mean thermal conductivity of the contact interface, R_{st} is the surface roughness of the contact interface and N_P is a pressure-dependent parameter. α_l represents the effect of the specimen thickness on the IHTC and modelled by Eq. (5.3):

$$\alpha_l = m\ln(l) + n \tag{5.3}$$

where m and n are model parameters, which were determined from the experimentally observed trends of the IHTC. Although the specimen thickness has no effect on the true IHTC at the contact interface, the engineering (equivalent) IHTC affected by the specimen thickness would be required for accurately predicting the temperature evolutions of specimens with different thicknesses in simulations of hot stamping processes.

The solid-contact IHTC h_s depends on the thermal conductivity of the two contact solids and the contact surfaces. Eq. (5.2) therefore was developed combining the physical mechanism of the heat transfer between the contact surfaces and the theory of Cooper and Yovanovich [51]. The amount of heat transfer was considered to increase with increasing thermal conductivity of both the specimen and tools. The solid-contact IHTC h_s is thus correlated positively with the harmonic mean thermal conductivity K_{st}, which is appropriate to average the heat transfer rate. In order to simplify the model, the harmonic mean thermal conductivity K_{st} shown in Eq. (5.4) was determined from the thermal conductivities of the specimen k_s and the tools k_t, describing the ability of the contact interface to conduct heat.

$$K_{st} = \frac{2}{k_s^{-1} + k_t^{-1}} \tag{5.4}$$

Meanwhile, the amount of heat transfer was reduced with decreasing real contact area between the specimen and tools, which was associated with a higher initial surface roughness of the contact surfaces. Hence a negative relationship between the solid-contact IHTC h_s and the surface roughness of the contact interface R_{st} was considered. R_{st} was the root mean squared value of the measured average surface roughness of the specimen R_s, i.e. $R_{a,s}$ and the tools R_t, i.e. $R_{a,t}$, representing the surface roughness conditions of the contact interface, as shown in Eq. (5.5). Due to no relative sliding between the specimen and tools occurred, the change of the surface roughness from its initial value to the post-compression value was completed within a short time period. Therefore, the present research assumed that the variation of the surface roughness had no effect on the IHTC, leading to the application of the initial surface roughness as a constant value in this model. It should be noticed that the variation of the surface roughness would have an effect on the IHTC at a slow stamping speed in a real forming process. The interaction between the surface condition and IHTC will be a topic in future work.

$$R_{st} = \sqrt{R_s^{\,2} + R_t^{\,2}} \tag{5.5}$$

The heat transfer was more rapid when the contact pressure increased, as the real contact area between the contact surfaces was increased. Hence this results in a positive correlation between the solid-contact IHTC h_s and the pressure dependent parameter N_P, which can be represented by the following exponential-law equation, Eq. (5.6):

$$N_P = 1 - \exp[-\gamma \frac{P}{\sigma_U(T)}] \tag{5.6}$$

where γ is a model parameter and $\sigma_U(T)$ is the ultimate strength of the specimen at elevated temperatures, which was obtained by the results of the uniaxial tensile tests. The current equipment was not able to accurately measure the hardness of the specimen at elevated temperatures. The ratio of the applied contact pressure to the ultimate strength of the specimen is equivalent to the ratio of the real contact area to the apparent contact area at that contact pressure, representing the deformation mechanism of the asperities on the specimen surface [52]. However, when the real contact area approaches the apparent contact area at a large contact pressure, the increasing contact pressure would not affect the IHTC any longer, leading to a plateau of the IHTC [76], [77]. Therefore, the relationship between the solid-contact IHTC and the contact pressure follows an exponential-increasing trend. This indicated that the contact pressure works as a driving force for the solid-contact IHTC h_s in the developed model. The present research did not measure the real contact area and asperities of the specimen to explain the contact pressure mechanism according to a microscopic view. This would be a topic in future work to validate the contact pressure mechanism.

When a coating was applied onto the tool, an additional heat transfer medium would be to contribute to the overall IHTC as the coating-contact IHTC h_c, which was modelled by Eq. (5.7):

$$h_c = \beta \frac{k_s \ln(k_c/k_t)}{A} \delta_c N_P \tag{5.7}$$

where β is a model parameter, k_c is the thermal conductivity of the coating, δ_c is the coating thickness and A is the contact area. When a coating with a thermal conductivity higher than that of the substrate is applied, the heat transfer through the contact area A is enhanced, leading to a positive effect on the IHTC. In contrast, the IHTC is decreased when a coating with a thermal conductivity lower than that of the substrate is applied, due to the reduced heat transfer across the coating layer. The term $\ln(k_c/k_t)$ represents either a positive or negative effect of the applied coating on the heat transfer. The coating thermal performance is also amplified with increasing coating layer thickness δ_c, due to the longer distance over which heat transfer occurs, which was also deduced in previous research [25]. The pressure dependent parameter N_P captures the effect of the contact pressure as described previously.

In order to enable the prediction of the IHTC evolutions as a function of the initial blank temperature, the identification and development of the temperature-dependent parameters in the model were necessary. According to the results of the IHTC tests, the tool coating was independent of the initial blank temperature in its effect on the IHTC. Therefore, the model parameter β was maintained as a constant value. In contrast, the material strength and thermal conductivity of the specimen contributed to the temperature-dependent IHTC. Hence, the ultimate strength of the specimen σ_U and the model parameter φ were identified as temperature-dependent parameters and modelled by Eqs. (5.8 and 5.9) using Arrhenius equations [78]. In addition, the thermal conductivity of the specimen $k_t(T)$ was a temperature-dependent material property and characterised by Johnson [68].

$$\sigma_U(T) = \sigma_0 \exp(\frac{Q_\sigma}{RT}) \tag{5.8}$$

where σ_0 and Q_σ were the model constants, determined through tensile tests at elevated temperatures at a strain rate of 1 s^{-1}, $\boldsymbol{R}$ is the molar gas constant, and T is the absolute temperature in Kelvin.

$$\varphi(T) = \varphi_0 \exp(\frac{Q_\varphi}{RT}) \tag{5.9}$$

where φ_0 and Q_φ were the model constants, determined using different values of φ at elevated temperatures.

When a lubricant was applied, the number of heat transfer mediums were increased to four, i.e. the specimen, coating, tool and lubricant. The simultaneous application of both coating and lubricant to the tools was not studied in the present research. Therefore, the harmonic mean thermal conductivity of the three contact mediums K_{slt} is correlated positively with the time-dependent lubricant-contact IHTC $h_l(t)$ and modelled by Eq. (5.10):

$$K_{slt} = \frac{3}{k_s^{-1} + k_l^{-1} + k_t^{-1}} \tag{5.10}$$

where k_l is the thermal conductivity of the lubricant. It was found that $h_l(t)$ is positively correlated to the lubricant layer thickness, and negatively correlated to the surface roughnesses of the specimen and tools, as derived from the experimental IHTC results for AA6082 and AA7075. The root mean square of the initial surface roughness R_{st} of the specimen and tools is still used to represent the surface condition at the contact interface. Hence, the lubricant-contact IHTC $h_l(t)$ was modelled as shown in Eq. (5.11):

$$h_l(t) = \omega \frac{K_{slt} N_\delta(t)}{R_{st}} \tag{5.11}$$

where ω is a model parameter. The effect of the lubricant thickness was represented by the lubricant thickness-dependent parameter $N_\delta(t)$. Increasing the lubricant layer thickness enhances thermal conduction and heat dissipation, and thus increases the IHTC. This relationship, between the instantaneous lubricant layer thickness $\delta_l(t)$ and the lubricant thickness-dependent parameter $N_\delta(t)$, was modelled by Eq. (5.12), which defines the effect of the lubricant on the IHTC.

$$N_\delta(t) = 1 - \exp[-\theta \delta_l(t)] \tag{5.12}$$

where θ is a model parameter. In the present research, the lubricant layer thickness was assumed to be constant, and no sliding between the specimen and the tools occurred. However, as the lubricant thickness-dependent parameter decreases due to the diminution of the lubricant layer thickness when sliding does occur, it is therefore expressed as a time-dependent variable.

In the present research, a lubricant diminution model developed by Hu et al. [79] was extended to represent the lubricant behaviours during the sliding wear. The behaviour of different lubricants applied at the contact interface is determined by their thermal conductivity and viscosity, which affect the heat transfer and lubricant diminution rate respectively. It has been found that the frictional energy dissipation was faster and the lubricant diminution rate was lower with increasing lubricant viscosity [80]. Furthermore, the ratio of contact pressure to lubricant viscosity affected the lubricant layer thickness [81]. The lubricant diminution rate was therefore modelled as Eq. (5.13):

$$\dot{\iota} \qquad {}_{at} \cdot = -\delta_l[b(P/\eta)^{\lambda_1} v^{\lambda_2} t] \tag{5.13}$$

where b , λ_1 and λ_2 are model parameters, η is the lubricant viscosity and v is the sliding speed. In order to simplify the model, the lubricant viscosity at room temperature is used and is assumed to be a constant during sliding. Considering the boundary conditions as $\delta_l(t) = \delta_l(0)$ when t is zero, the instantaneous lubricant layer thickness equation can be integrated into the form of Eq. (5.14):

$$\delta_l(t) = \delta_0 \exp[b(P/\eta)^{\lambda_1} v^{\lambda_2} t] \tag{5.14}$$

where δ_0 is the initial lubricant layer thickness and $\exp[b(P/\eta)^{\lambda_1} v^{\lambda_2} t]$ indicates the lubricant layer thickness diminution rate. Therefore, the time-dependent lubricant-contact IHTC $h_l(t)$ was modelled as a function of the initial lubricant layer thickness and sliding time, through the combination of the IHTC and the lubricant diminution models, enabling the effect of the lubricant diminution on the IHTC to be predicted. The graphite lubricant used in the present work was the same as that used in the study of Hu et al. [79], and thus the same values of b , λ_1 and λ_2 were used. The excessive lubricant was always applied in the hot stamping processes. In addition to the lubricant diminution, the lubricant growth also occurred in some regions during sliding. Due to the convergent lubricant thickness being reached, the lubricant growth would not affect the IHTC. Therefore, the lubricant growth was not accounted for the developed model.

The model parameters shown in Table 5.1 were calibrated using the experimental data from the IHTC tests under different experimental conditions in Chapter 4. There were in total 31 parameters in this model, and 13 of them were alloy-dependent constants. Fig 5.1 shows all agreements between the experimental and predicted IHTC evolutions for AA7075 and AA6082 aluminium alloys under different conditions. The calibrated model could therefore be used to predict the IHTC evolutions as a function of contact pressure, tool material, coating material, specimen thickness and lubricant layer thickness.

Table 5.1. Model parameters of the IHTC model.

AA7075						
h_a (kW/m^{2}K)	m (-)	n (-)	σ_U (MPa)	γ (-)	β (-)	A (m^2)
0.2	2.1e-4	9.9e-5	21	6.05	3.5e3	5e-4
ω (-)	θ (m^{-1})	φ_0 (-)	σ_0 (MPa)	Q_σ (J/mol)	Q_φ (J/mol)	R (J/molK)
1.1e-4	2e5	0.63	5.69	1581.61	-2845.93	8.31
AA6082						
h_a (kW/m^{2}K)	m (-)	n (-)	σ_U (MPa)	ω (-)	θ (m^{-1})	γ (-)
1.4	1.6e-4	1.5e-4	50	1.2e-4	1.5e5	5.2
λ_1 (-)	λ_2 (-)	b ($s^{\lambda_2-\lambda_1-1}GPa^{-\lambda_1}mm^{2\lambda_1-\lambda_2}$)				
0.75	0.73	23.02				

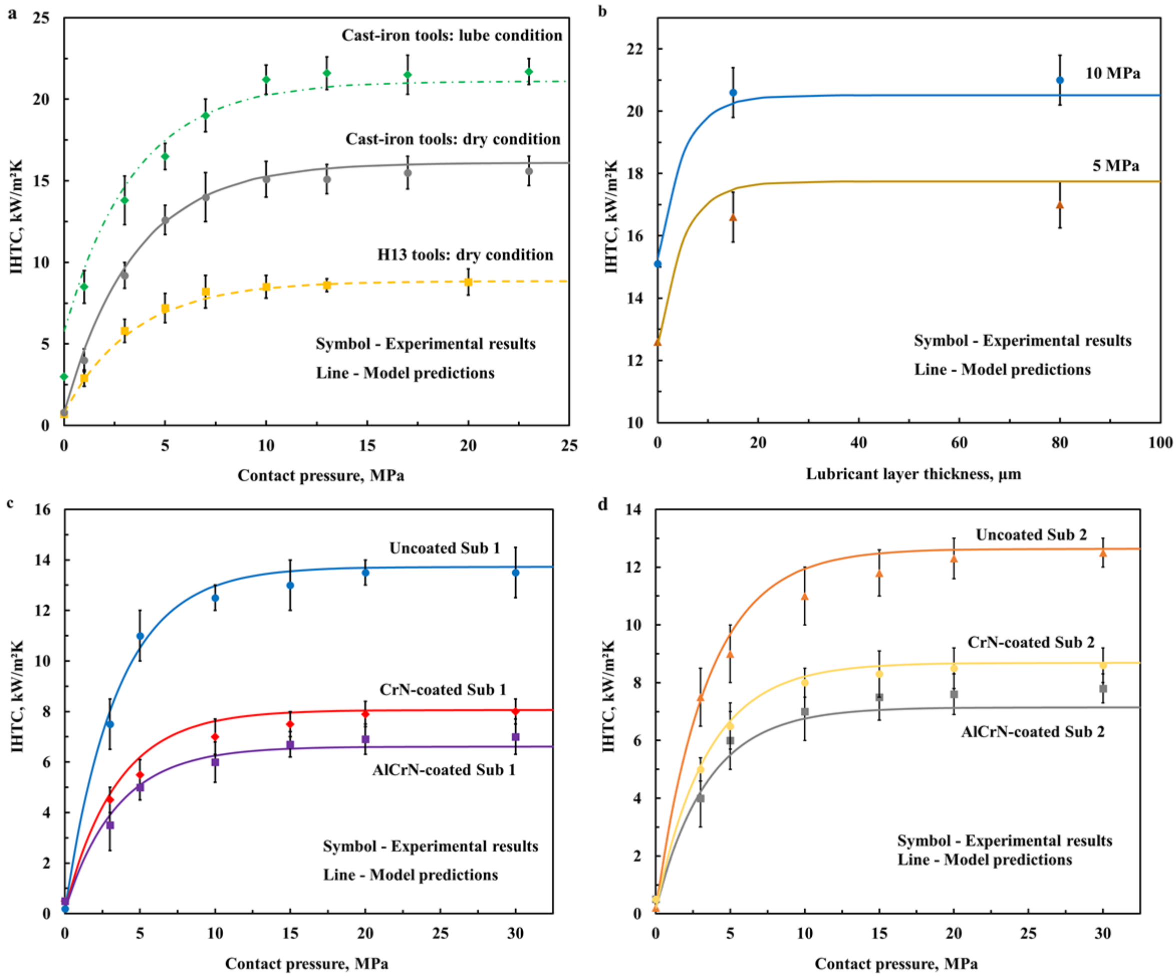

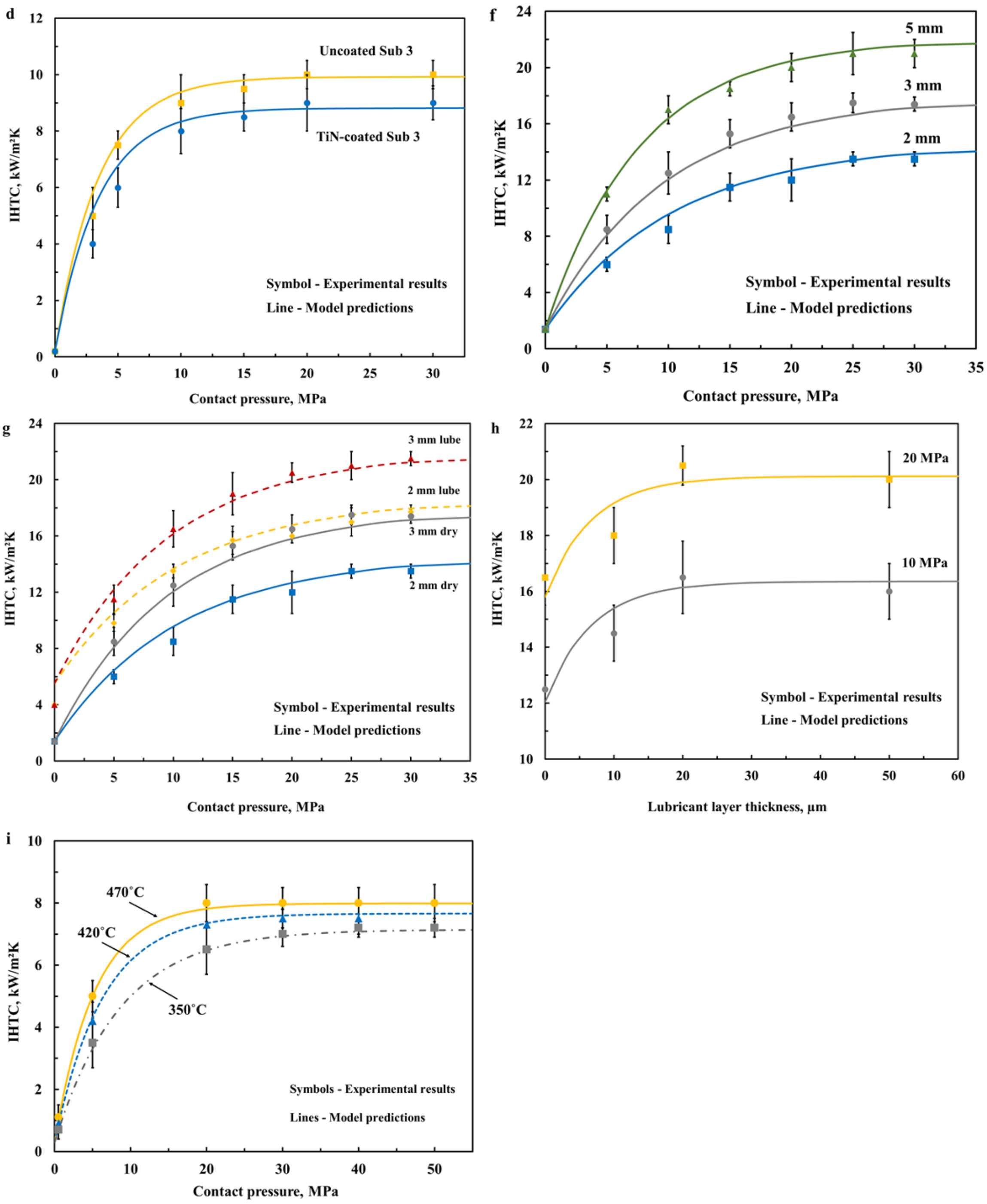

Fig. 5.1. Comparisons between the experimental and predicted IHTC evolutions for (a) AA7075 with contact pressure using different tools; (b) AA7075 with lubricant layer thickness at different contact pressures; (c) AA7075 with contact pressure using different uncoated and coated Substrate 1; (d) AA7075 with contact pressure using different uncoated and coated Substrate 2; (e) AA7075 with contact pressure using different uncoated and coated Substrate 3; (f) different thickness AA6082 with contact pressure under dry conditions; (g) different thickness AA6082 with contact pressure under both dry and lubricated conditions; (h) AA6082 with lubricant layer thickness at different contact pressures; (i) AA7075 with contact pressure at different initial blank temperatures.

5.2 Interaction between the IHTC and lubricant diminution during sliding

The diminutions of the lubricant layer thickness and the IHTC for the 3 mm thick AA6082 specimen with sliding distance and time at different contact pressures were predicted by the IHTC model for a sliding speed of 400 mm/s using a time step of 0.01 second, which was able to provide accurate results, as shown in Fig. 5.2 (a). It was found that the lubricant diminishes more rapidly at a higher contact pressure, which agreed with the analysis in Section 5.1. When the remaining lubricant layer thickness reaches the 20 μm convergent point at the sliding distances of approximately 64 mm (sliding time of 0.16 seconds) and 28 mm (sliding time of 0.07 seconds) for contact pressures of 10 and 30 MPa respectively, the IHTC values start to decrease from their respective stable values of 16.3 and 21.4 kW/m^{2}K.

Lubricant breakdown occurs when the lubricant layer thickness is less than the tool's asperity height [82]. In the present research, the tool's asperity height is assumed to be the average surface roughness of the tools, i.e. 1 μm. When the sliding distance is 360 mm (sliding time of 0.9 seconds) and 152 mm (sliding time of 0.38 seconds) at contact pressures of 10 and 30 MPa respectively, the lubricant layer thicknesses at both contact pressures are lower than 1 μm, and lubricant breakdown occurs. Consequently, the IHTC values decrease dramatically to 12.7 kW/m^{2}K at 10 MPa and 18.0 kW/m^{2}K at 30 MPa. To compensate for the loss in the IHTC and avoid an insufficient cooling rate induced by the lubricant diminution, the IHTC can be increased by increasing the instantaneous contact pressure. However, the lubricant service life would be decreased more rapidly as a result of the higher contact pressure.

Typically, the lubricant diminution rate increases with increasing sliding speed as a function of sliding time. However, for the same sliding distance, the sliding time and hence the lubricant diminution rate decreases with increasing sliding speed. As shown in Fig. 5.2 (b), the diminution rates of the lubricant layer thickness and the IHTC as a function of sliding distance increase when the sliding speed decreases from 400 to 100 mm/s for a contact pressure of 10 MPa. When the remaining lubricant layer thickness reaches the 20 μm convergent point at the sliding distances of approximately 47 and 64 mm for sliding speeds of 100 and 400 mm/s respectively, the IHTC values for AA6082 start to decrease from the stable value of 16.3 kW/m^{2}K. When the sliding distances are 250 and 360 mm at sliding speeds of 100 and 400 mm/s respectively, lubricant breakdown occurs. The IHTC values decrease to 12.7 kW/m^{2}K and approach the final stable value of 12.1 kW/m^{2}K.

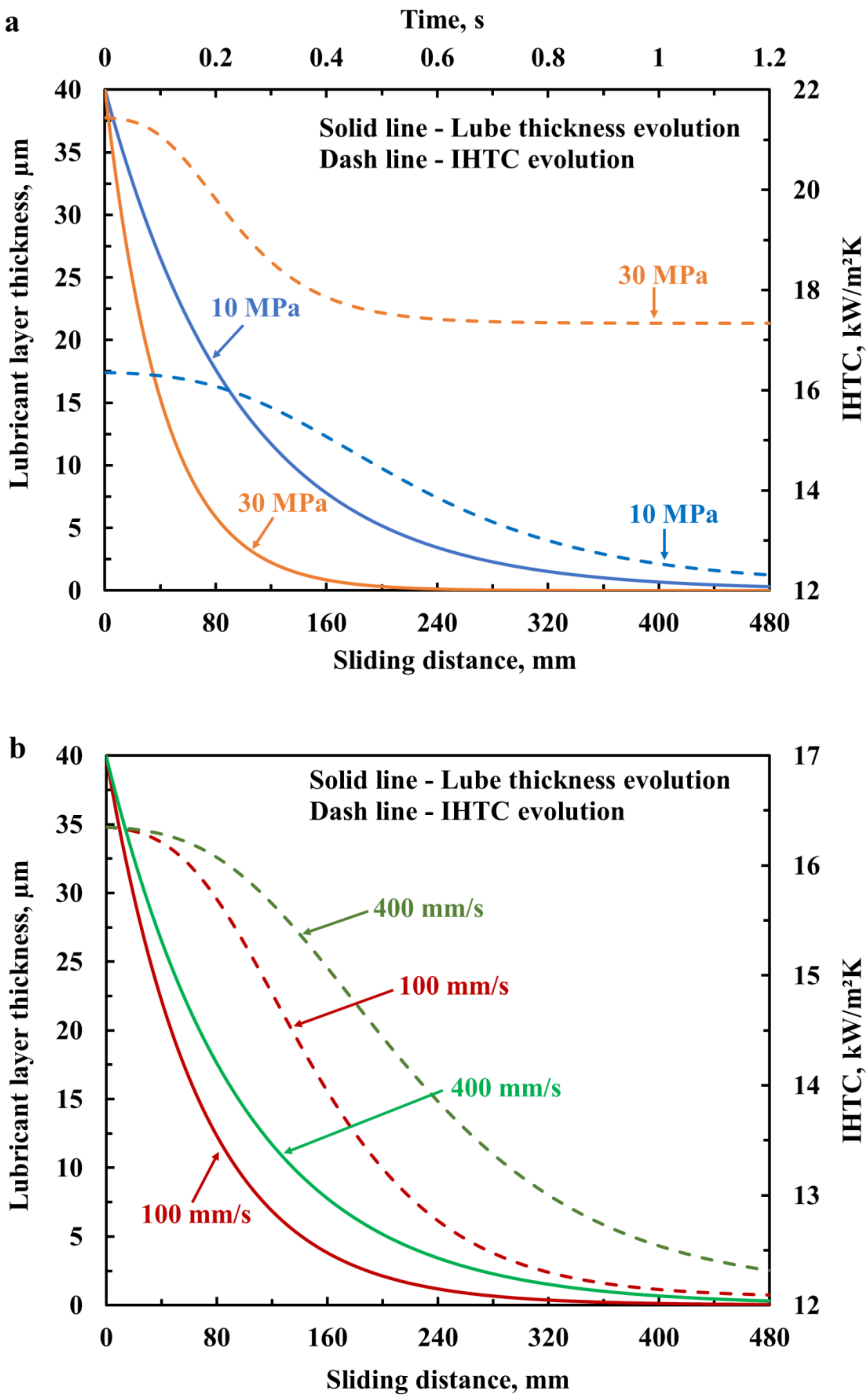

Fig. 5.2. Lubricant layer thickness diminutions and the IHTC diminutions for AA6082, with sliding distance and time at (a) different contact pressures; and (b) different sliding speeds.

The lubricant service life can be increased with increasing sliding speed, leading to the maintenance of higher IHTC values over a longer sliding distance. Therefore, it is crucial to predict the lubricant layer thickness and IHTC evolutions with sliding distance (time) using the IHTC model for a given contact pressure and sliding speed.

Fig. 5.3 shows the IHTC model predictions for AA6082 specimens of different thicknesses under lubricated conditions. Three-dimensional IHTC surface plots were generated as a function of sliding distance and contact pressure/sliding velocity, for an initial lubricant layer thickness of 40 µm. The surface plots indicate the lubricant behaviour at different stages; namely stage I (excessive stage), in which the lubricant is applied excessively, and the IHTC is plateaued, stage II (consumption stage), in which the lubricant diminishes during sliding and the IHTC decreases rapidly, and stage III (breakdown stage), in which lubricant breakdown occurs and the IHTC is equal to its values under dry conditions. The predicted IHTC surface plots can be implemented in FE simulations as boundary conditions to accurately simulate temperature evolutions of a blank during deformation.

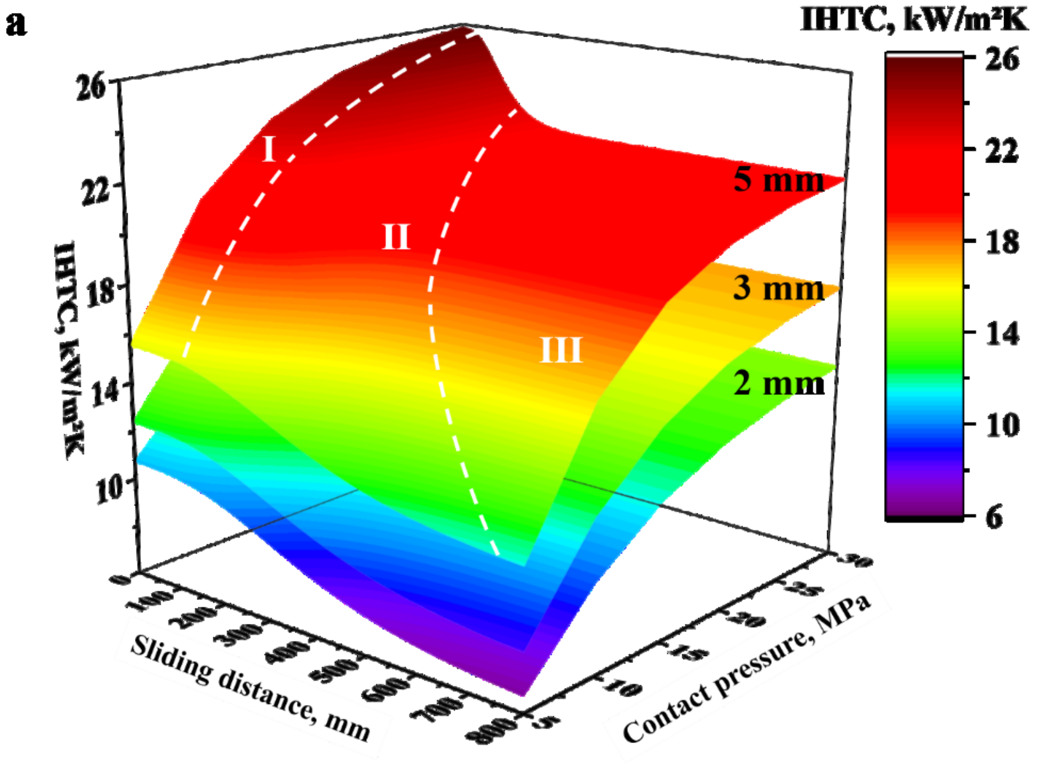

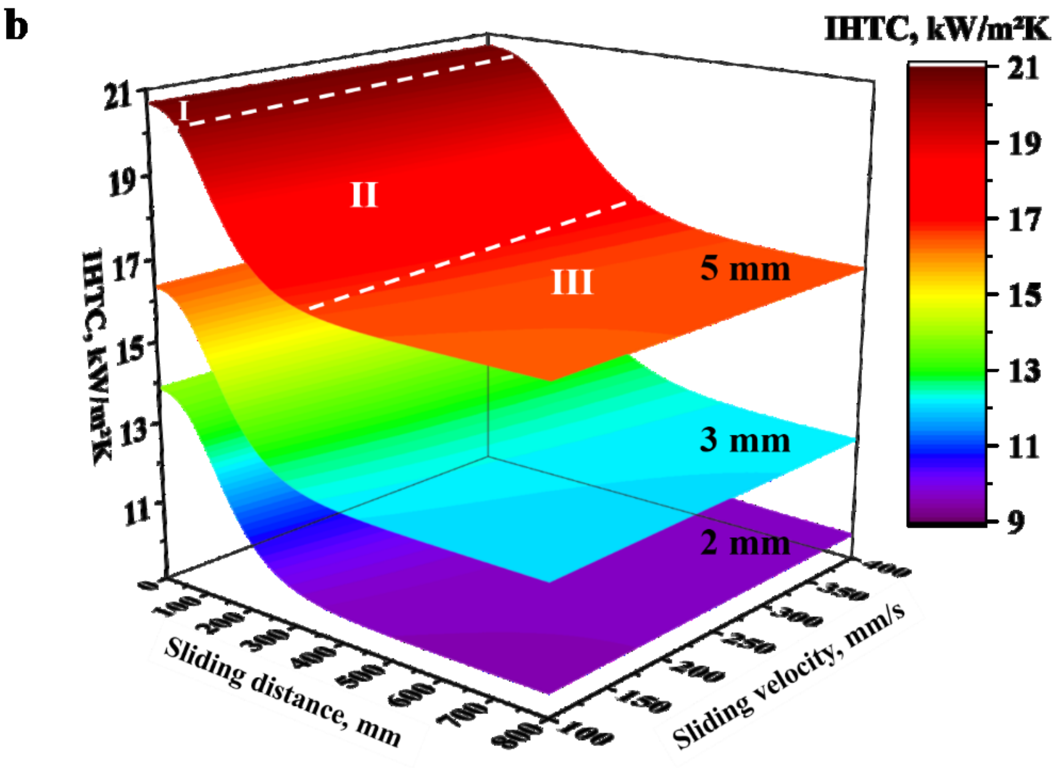

Fig. 5.3. Three-dimensional representation of the time-dependent modelling predictions: IHTC surfaces for AA6082 specimens of different thicknesses as a function of (a) sliding distance and contact pressure when the sliding speed is 400 mm/s and the initial lubricant layer thickness is 40 μm; (b) sliding distance and sliding speed when the contact pressure is 10 MPa and the initial lubricant layer thickness is 40 μm.

Fig. 5.4 shows the predicted diminutions of the lubricant layer thickness and the IHTC for the 3 mm thick AA6082 specimens as a function of sliding distance (time) for a contact pressure of 10 MPa and a sliding speed of 400 mm/s, using three different widely used lubricants, whose material properties are shown in Table 5.2.

Table 5.2. Lubricant material properties

Property	Poly-α-olefin (PAO) [83]	TC5600 [63]	Graphite (Oil-based)
State	Liquid	Grease	Grease
Thermal conductivity (W/mK)	0.154	7.1	24
Viscosity (mm^2/s)	150	24	35

It was found that the PAO lubricant diminishes most slowly due to its highest viscosity, while the TC5600 lubricant diminishes fastest due to its lowest viscosity. When the sliding distances are approximately 52, 68 and 204 mm, the remaining lubricant layer thickness reaches the 20 μm convergent point, using TC5600, graphite and PAO lubricants respectively. The IHTC starts to decrease from 14 kW/m^{2}K when using TC5600 lubricant and decreases from 16.3 kW/m^{2}K at a larger diminution rate when using graphite lubricant. Compared to that of TC5600 and graphite lubricant, the effect of the diminution of the PAO lubricant on the IHTC is negligible due to its low thermal conductivity, and it consequently has a stable IHTC value of 12.1 kW/m^{2}K. When the sliding distances are 268 and 360 mm, the breakdown of the TC5600 and graphite lubricants occur, while the breakdown of the PAO lubricant only occurs significantly later at a sliding distance of approximately 1088 mm.

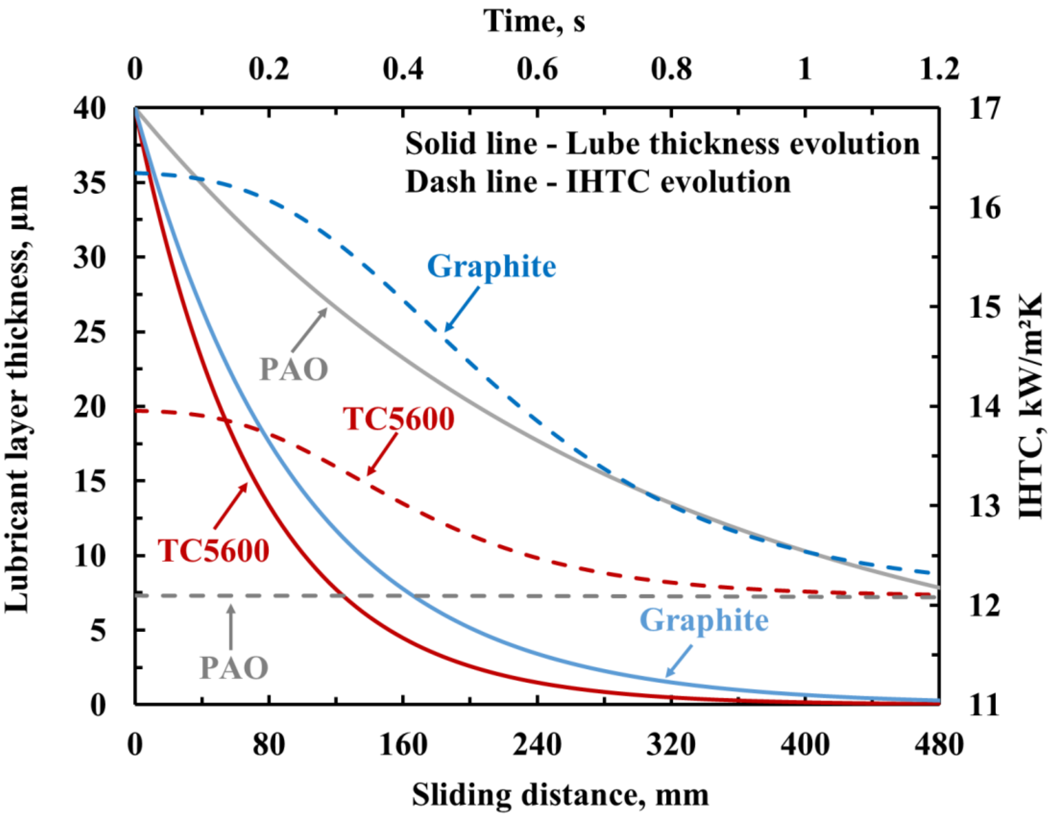

Fig. 5.4. Lubricant layer thickness diminutions and the IHTC diminutions for the 3 mm thick AA6082 specimens, with sliding distance and time using different lubricants for a contact pressure of 10 MPa and a sliding speed of 400 mm/s.

Therefore, the interactive IHTC model enables the identification and the application of different lubricants to achieve different forming processing requirements. The lubricants with high thermal conductivities and viscosities, e.g. graphite, can be applied to increase the IHTC, achieve the required high critical cooling rates, and also increase the lubricant and tool service lives, whilst those with low thermal conductivities and high viscosities, e.g. PAO, can be applied to reduce the friction and meanwhile prevent the IHTC from increasing, thus avoiding a large temperature loss from blanks. When the thermal conductivities and viscosities of different lubricants are implemented into the model, the IHTC and lubricant evolutions can therefore be successfully predicted as a function of sliding distance (time) at different contact pressures and sliding speeds.

5.3 Functional predictions by the IHTC model

The developed mechanism-based IHTC model is capable of predicting the IHTC values between two metallic materials. For example, Fig. 5.5 (a) shows the predicted IHTC evolutions between 7075 aluminium alloy and P20 tool steel as a function of contact pressure under both dry and full-lubricated conditions. In order to verify this functional prediction by the model, these predicted IHTC evolutions as a function of contact pressure were implemented in the FE simulation to simulate the temperature evolutions of the AA7075 specimens when using the P20 tools at a contact pressure of 3 MPa under dry conditions, and 13 MPa under full-lubricated conditions. Meanwhile, new IHTC tests were conducted under the same conditions as those of the simulations with three repeat tests for each condition. As shown in Fig. 5.5 (b), it was evident that the simulated temperature evolutions were in close agreement with the experimental curves, indicating the IHTC values between AA7075 and P20 under both dry and full-lubricated conditions were accurately predicted.

Meanwhile, it was found that the peak IHTC value between AA7075 and P20 under dry conditions, 11 kW/m^{2}K, lay between the peak values obtained when using H13 and cast-iron G3500 tools, and the thermal conductivity of P20 (0.0315 kW/mK) was also in between both H13 and cast-iron G3500. This once again identified the effect of the tool material on the IHTC, i.e. the IHTC increases with increasing thermal conductivity of the tool.

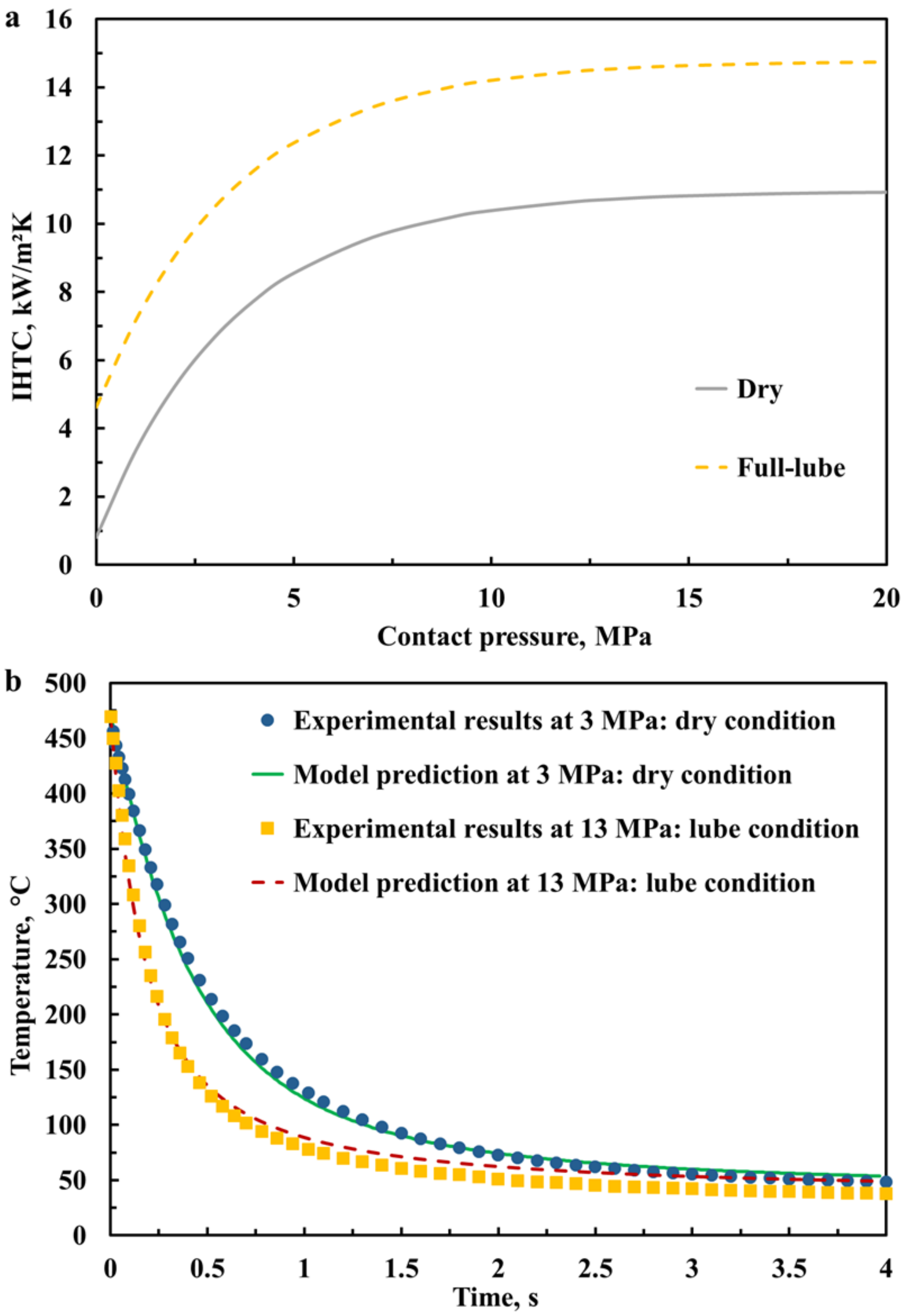

Fig. 5.5. (a) Predicted IHTC evolutions between AA7075 and P20 with contact pressure under dry and full-lubricated conditions; (b) Comparisons between the experimental and simulated temperature evolutions of the AA7075 specimens at 3 MPa under dry conditions and 13 MPa under full-lubricated conditions.

In addition, the IHTC evolution at an initial blank temperature of 300°C when using the WC-coated tools was predicted and then compared with the experimental results. As shown in Fig. 5.6, the rapid-increasing stage and the plateau of the IHTC were precisely predicted. The excellent agreement between the experimental and predicted IHTC evolutions under different conditions indicated that the developed IHTC model enables the accurate prediction of the IHTC as a function of the initial blank temperature as well.

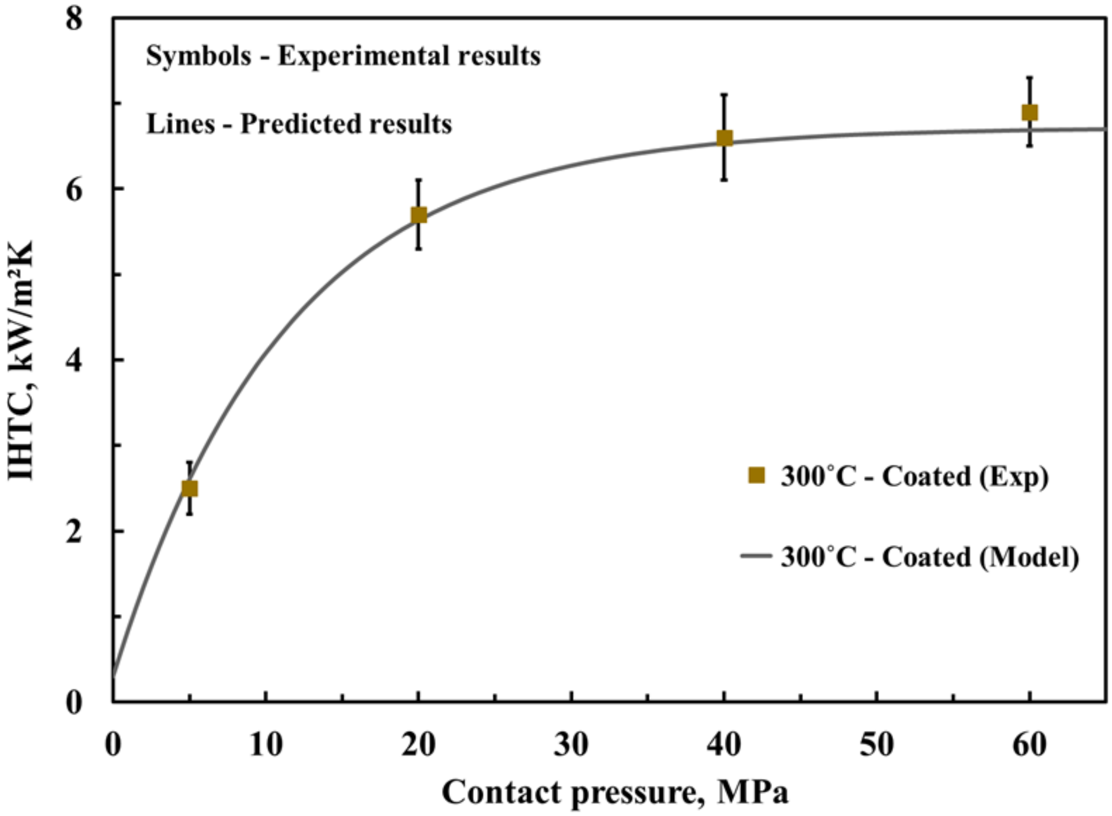

Fig. 5.6. Experimental and predicted IHTC evolutions at an initial blank temperature of 300˚C when using WC-coated D6510 tools.

Furthermore, if specimens with higher thermal conductivities are used, the corresponding IHTC will have higher values due to a greater amount of heat transfer between the two contact solids. Fig. 5.7 shows another functional prediction by the IHTC model, in which the IHTC evolutions as a function of the thermal conductivity of the tool and specimen, at a constant contact pressure of 15 MPa and surface roughness of 810 and 340 nm for the tool and specimen respectively, under dry and full-lubricated conditions, were predicted. The results of the H13, P20 and AA7075 were experimentally verified.

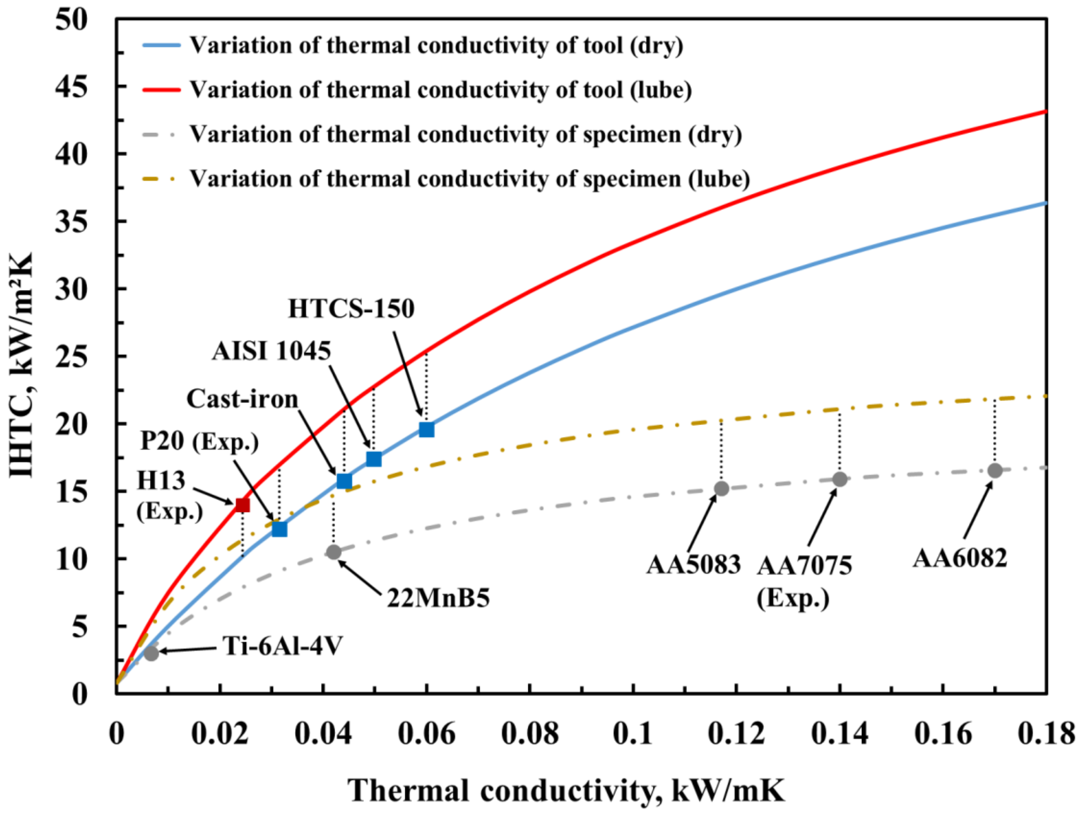

Fig. 5.7. Predicted IHTC evolutions with the thermal conductivity of the tool and specimen.

The IHTC values for AA7075 using tools with a greater thermal conductivity than that of the cast-iron, e.g. AISI 1045 [84] and HTCS-150 tool steels [85], will therefore be higher. When using the cast-iron, the IHTC values for aluminium alloys with a smaller thermal conductivity than that of AA7075, e.g. AA5083 [10], will thus be lower under the same conditions. Furthermore, the model also has a considerable potential to predict the IHTC values for different metallic materials if their properties are given and substituted into the model.

In addition, the application of lubricant enhances the IHTC values, indicating that using tools with lower thermal conductivities, e.g. H13, under lubricated conditions could achieve similar results to using tools with higher thermal conductivities, e.g. cast-iron, under dry conditions. This feature would be beneficial to the reduction of the requirements of the forming press capabilities, as lower contact pressures could consequently be applied.

Theoretically, this model is also able to predict the effect of the surface roughness on the IHTC. Fig. 5.8 shows the predicted IHTC evolutions as a function of the surface roughness of the tool and specimen at a constant contact pressure of 15 MPa and thermal conductivities of 0.0244 and 0.14 kW/mK for the tool and specimen respectively, under dry conditions. The results of the H13 and AA7075 were experimentally verified. In general, the IHTC evolutions decrease with increasing surface roughness of the tool and specimen, because the real contact area has an inverse relationship with the surface roughness. As discussed earlier, the surface roughness of the specimen approaches the value of that for the tools during a hot stamping process, due to the higher strength of the tools. The initial surface roughness of the tools before stamping is therefore crucial, whereas the value for the specimen has a marginal effect on the IHTC. The meshing between the two contact surfaces decreases with increasing initial surface roughness of tools. Consequently, the real contact area and the IHTC values decrease. These predictions agree with the previous theoretical analysis.

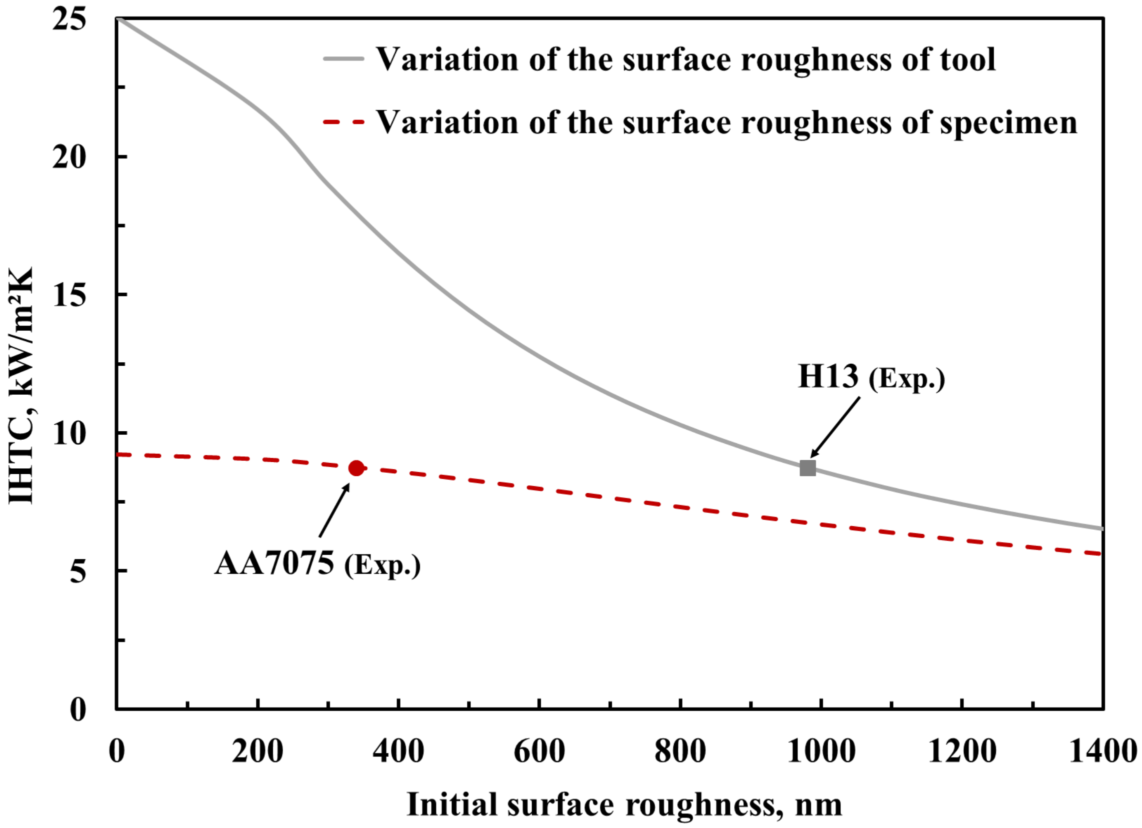

Fig. 5.8. Predicted IHTC evolutions with the initial surface roughness of tool and specimen.

5.4 Summary

The key findings of this chapter were summarised below:

- A mechanical-based IHTC model was developed to predict the IHTC evolutions as a function of contact pressure, tool material, coating material, specimen thickness, lubricant and initial blank temperature for different aluminium alloys.

- Furthermore, the developed IHTC model provides an interactive method to predict the lubricant layer thickness diminution and the corresponding IHTC evolutions with sliding distance (time) at different contact pressures and sliding speeds, and it also enables the identification and application of different lubricants to achieve the desired forming processing requirements.
- In addition, the IHTC values between different metallic materials with different initial surface roughness were predicted to demonstrate the functional predictions by the developed IHTC model.
- Therefore, the selection of tool and coating materials, and the optimisation of instantaneous processing parameters, e.g. contact pressure, sliding speed and lubricant layer thickness, could ensure that the critical cooling rate can be satisfied in the hot stamping processes to achieve the desired post-form mechanical strength of formed components and optimise the production rate correspondingly.

Chapter 6

Case studies of the application of the IHTC model[6]

This chapter presents the case studies of the application of the IHTC model, which validated the experimental IHTC results and developed IHTC model. In practical hot stamping processes of complex-shaped components, the contact pressure may change over extremely short periods of time, leading to abrupt changes in the IHTC and the consequent temperature evolutions of the specimen. In this chapter, the IHTC test under variable contact pressure conditions was firstly conducted to verify that the IHTC values determined under constant contact pressure conditions could be used to simulate the temperature evolution of the specimen under variable contact pressure conditions. Subsequently, hemispherical dome and B-pillar forming tests were conducted to form different aluminium alloys to verify that the IHTC evolutions were accurately predicted by the developed IHTC model and thus enable the prediction of the temperature evolutions of materials in practical hot stamping processes. The last cast study is a CRRC Sifang project, the hot stamping of high strength aluminium panel components with complex structures.

---

[6] Chapter 6 was reproduced from two papers:

Liu, X., Ji, K., Fakir, O. El, Fang, H., Gharbi, M. M., Wang, L., 2017. Determination of interfacial heat transfer coefficient for a hot aluminium stamping process. J. Mater. Process. Technol. 247, 158–170. doi:10.1016/j.jmatprotec.2017.04.005

Liu, J., Wang, A., Zheng, Y., **Liu, X.**, Gandra, J., Beamish, K., 2017. Hot stamping of AA6082 tailor welded blanks for automotive applications. Procedia Eng. 0, 17–22. doi:10.1016/j.proeng.2017.10.820

6.1 IHTC test under variable contact pressure conditions

6.1.1 3-stage variable contact pressure

The data-driven approach was used in this research to determine the representative variable contact pressure conditions in practical hot stamping processes. Similar to that used in the study of Wang et al. [59], the data-driven approach still works in four stages, i.e. data acquisition, data storage, data processing and data analysis, as shown in Fig. 6.1. After processing the data, distributions of the contact pressure and contact area of the blank during hot stamping processes were generated as shown in Fig. 6.2, which includes the holding, stamping and quenching stages. The progression of the hot stamping process from 0 to 0.4 represents the holding stage, in which only the blankholder compresses the blank and thus the normalised contact area is small. A contact pressure of 0.7 MPa dominates in terms of probability during the holding stage. In the subsequent progression of the process from 0.4 to 0.75, the stamping stage occurs, and thus the normalised contact area increases dramatically. During this stage, a contact pressure of 4 MPa has the largest probability. When the blank is continually deformed and quenched after the process progression of 0.75, the normalised contact area reaches its maximum value, and the representative contact pressure with the largest probability is 15 MPa. A 3-stage variable contact pressure trend determined from these dominant contact pressure values could therefore represent the variable contact pressure conditions during hot stamping processes. Specifically, the contact pressure abruptly changes from 0.7 to 4 and finally to 15 MPa over the duration of a hot stamping process, as shown in Fig. 6.3 (a). Big data was obtained from the existing verified hot stamping simulations run under different forming conditions, which covered all possible contact pressures, leading to dilute probabilities. As shown in Fig. 2.11, the largest probabilities of the temperature and strain rate in the hot stamping were only 16% and 12% respectively. Although their absolute values were not high, the relative values were still the largest compared to other probabilities, demonstrating their important shares in those distributions.

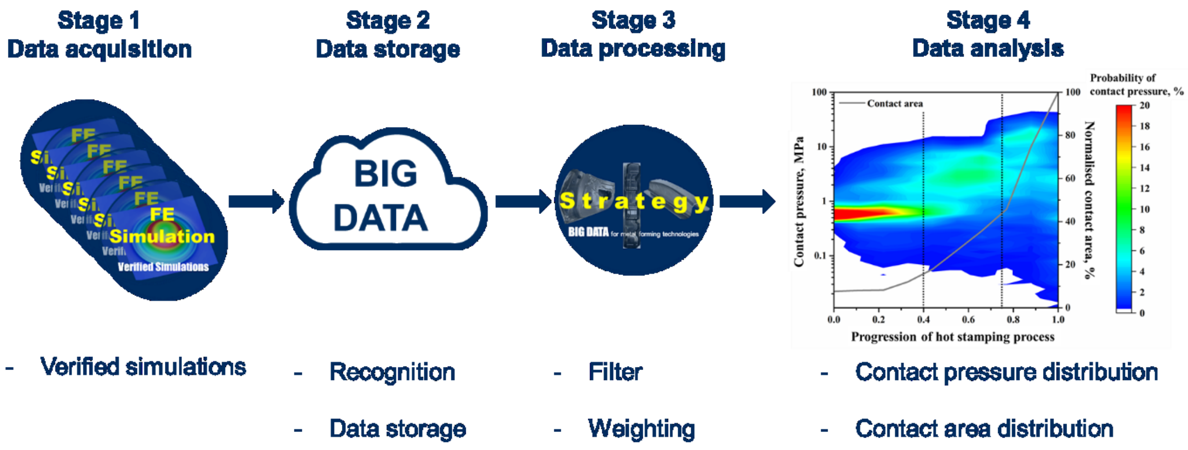

Fig. 6.1. Methodology of the data-driven approach.

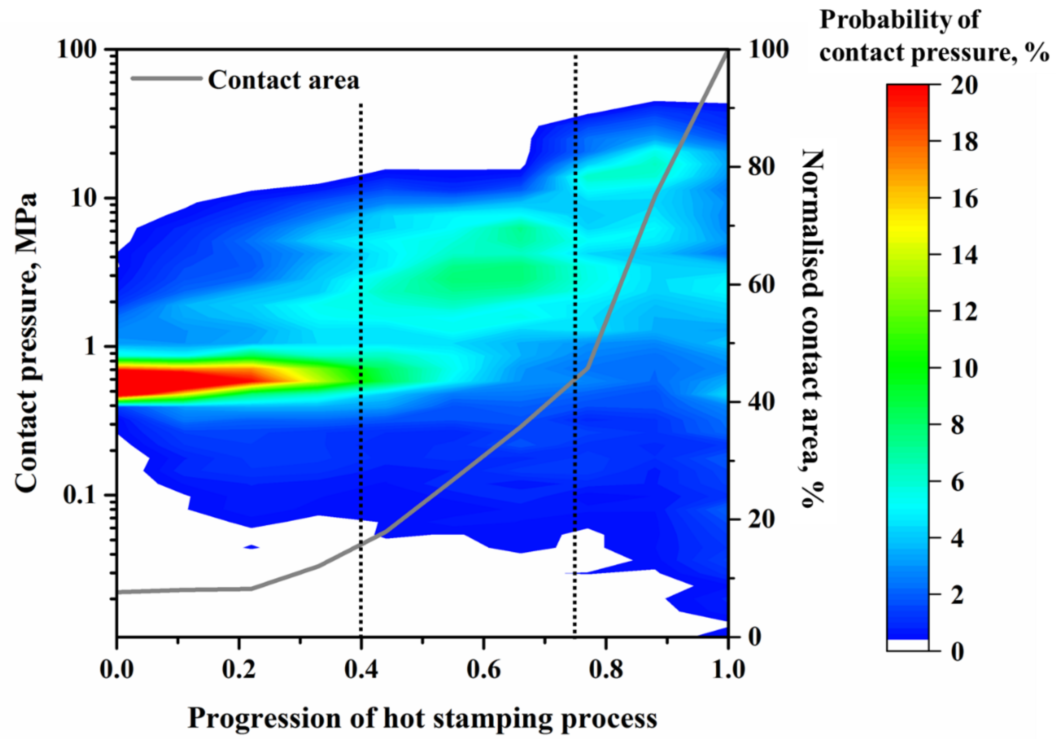

Fig. 6.2. Probability distribution of the contact pressure and the contact area evolution in the progression of the hot stamping process.

6.1.2 The IHTC and temperature evolutions under variable contact pressure conditions

The IHTC test was conducted with the defined 3-stage variable contact pressure trend using AlCrN-coated Substrate 1 to obtain the experimental temperature evolution of the AA7075 specimen. Meanwhile, the predicted IHTC evolution as a function of contact pressure and the same 3-stage variable contact pressure trend were assigned into the FE simulation of the IHTC test to simulate the temperature evolution of the specimen under the same experimental conditions.

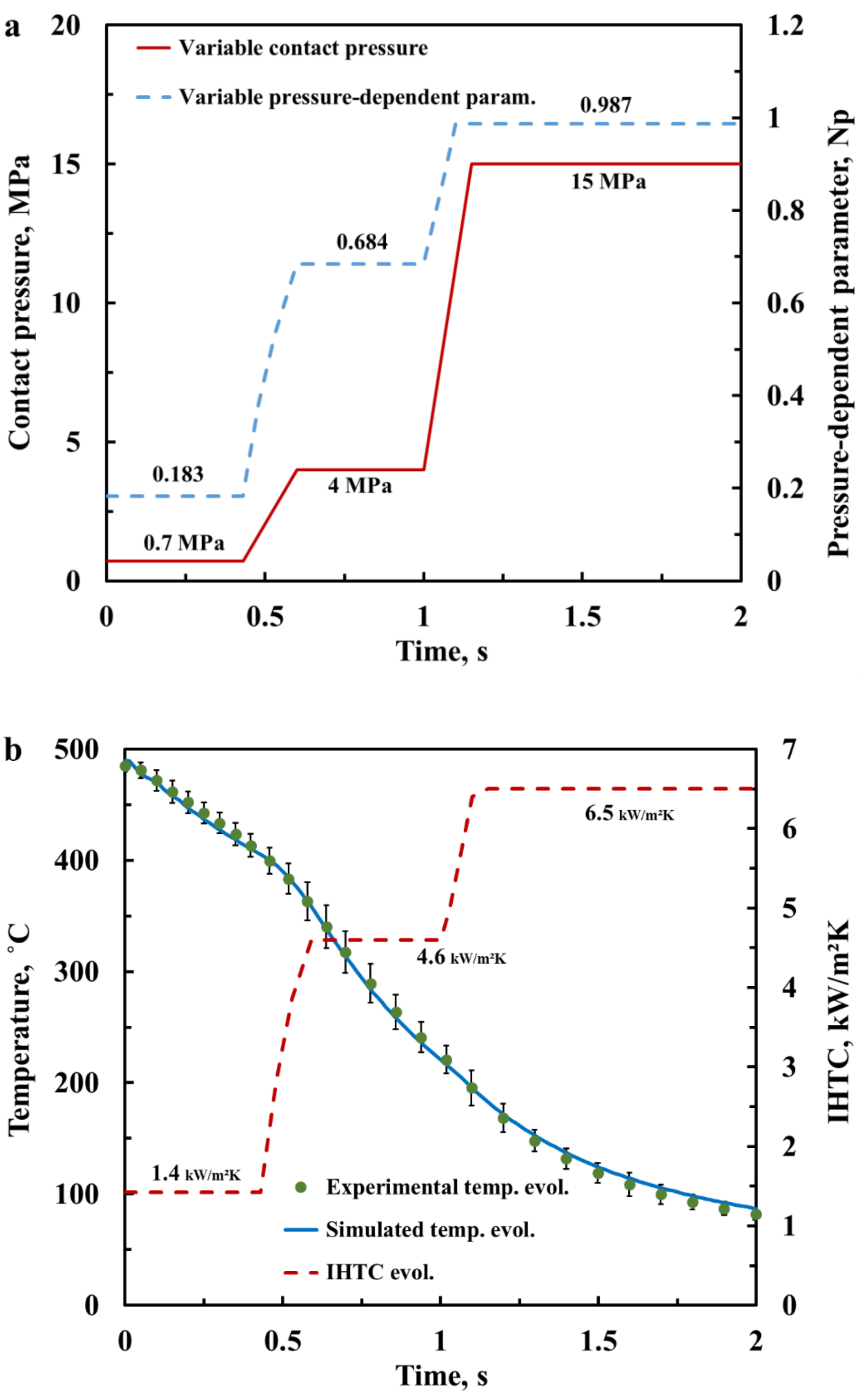

Fig. 6.3. (a) Applied variable contact pressure and the pressure-dependent parameter evolutions; (b) IHTC evolution for AA7075 and the comparison between the experimental and simulated temperature evolutions with variable contact pressure using AlCrN-coated Substrate 1.

As shown in Fig. 6.3 (a), when the contact pressure increased from 0.7 to 4 MPa at 0.43 seconds, the pressure-dependent parameter N_P was increased from 0.183 to 0.684, leading to the increasing overall IHTC value from 1.4 to 4.6 kW/m^{2}K, as shown in Fig. 6.3 (b). Consequently, the temperature decreasing rate was enhanced suddenly at 0.43 seconds. When the contact pressure increased from 4 to 15 MPa at 1 second, the pressure-dependent parameter N_P and thus the overall IHTC value increased further from 0.684 to 0.987, and from 4.6 to 6.5 kW/m^{2}K respectively. The decreasing rate of the specimen temperature was therefore increased suddenly again at 1 second. It should be noticed that the contact pressure could not be changed immediately, and its adjustment in the Gleeble machine was completed within 0.1 to 0.2 seconds.

The sudden changes of the temperature evolution at both 0.43 and 1 seconds were successfully captured by IHTC-mate 2.0 and accurately predicted by the FE simulation. The good agreement between the experimental and simulated temperature evolutions verified that the IHTC values determined under constant contact pressure could be applied to simulate the temperature evolution of the specimen under variable contact pressure conditions. Furthermore, it was also verified that IHTC-mate 2.0 enabled the application of variable contact pressure conditions and the measurement of pressure-sensitive temperature evolutions of the specimen over extremely short time periods.

6.2 Hemispherical dome forming tests

6.2.1 Hemispherical dome test procedure

Hemispherical dome forming tests were conducted to measure the temperature evolutions of the blanks during forming and validate the developed IHTC model further by implementing it in simulations of the tests. The tools used for the hemispherical dome forming tests were assembled in a 25 tonne ESH high-speed press and comprised a hemispherical die with a 100 mm diameter made from P20 tool steel, a blank with a contact surface of 180 x 180 mm^2, and a top and bottom blankholder, which were developed in the study of Fakir et al. [86], as shown in Fig. 6.4.

In order to monitor the temperature for each test, a pair of thermocouple was embedded in the middle of the blank and then connected to a thermometer. An AA7075 blank was initially heated up to its SHT temperature (490℃) and soaked for 3 minutes in a furnace. The hot AA7075 blank was then transferred rapidly onto the bottom blankholder within 10 seconds. Once the blank temperature dropped to around 430℃, the top blankholder was instantly actuated to move towards the blank and compress it against the bottom blankholder; a blankholding force of 20 kN was maintained by two gas springs. The compressed blankholders continuously moved towards the cold static die at a speed of 75 mm/s to deform the blank into a dome height of 10 mm. After a quenching period of 20 seconds, the top and bottom blankholders were returned to their initial positions. The temperature evolutions were recorded under both dry and lubricated conditions. For the latter, the same grease-based graphite lubricant used in the IHTC tests was sufficiently applied with great care onto the tool surfaces, ensuring the peak IHTC value was reached. Three repeat tests were conducted for each condition.

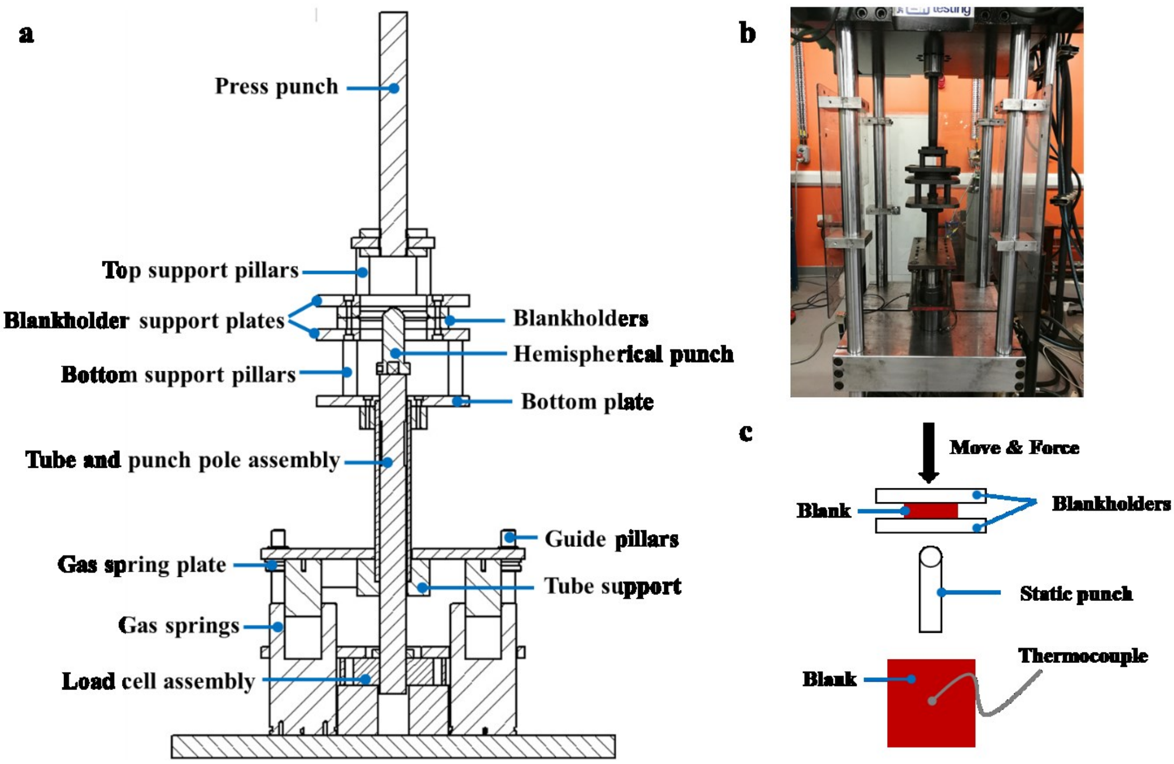

Fig. 6.4. (a) Section view of the forming tools; (b) Tool assembly in the 25-tonne ESH press; (c) Schematic diagram of the press movement and the location of the thermocouple on the blank.

6.2.2 FE simulation setup of the hemispherical dome test

In order to simulate the hemispherical dome forming tests, a FE model was developed in PAM-STAMP. The dimensions of the blank and tools were the same as those used in the experiments, as shown in Fig. 6.5. Quadrangle thermal shell elements with a size of 2 mm were used for the blank in the hemispherical dome FE simulations, which were identical to those used in the IHTC simulations. The initial temperature of the blank for the FE simulation was also set to the same value as that in the experiment, and the predicted IHTC evolutions with contact pressure using P20 tools under both dry and lubricated conditions were implemented in the FE simulation. The temperature evolutions of the blank under both dry and lubricated conditions were then simulated and compared with the experimental curves. It should be noticed that PAM-STAMP was not able to simulate the application of a lubricant in a hot stamping process. Instead, the corresponding IHTC evolution as a function of contact pressure under lubricated conditions was implemented in the FE simulation to represent the effect of the lubricant.

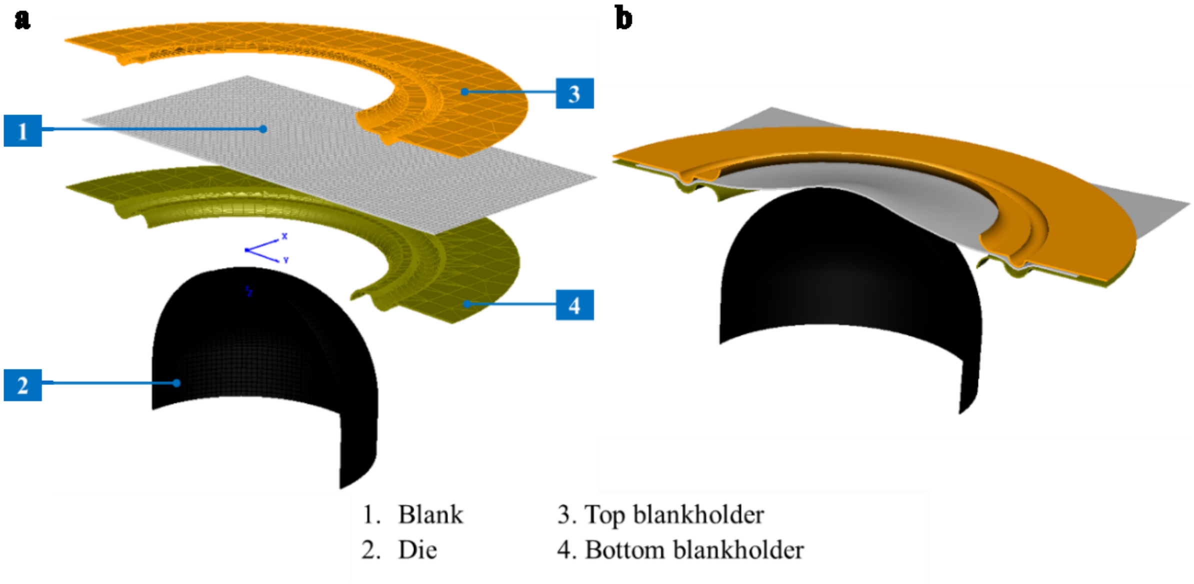

Fig. 6.5. FE model of the hemispherical dome test in PAM-STAMP (cross-sectional view), under (a) the loading condition; (b) the forming condition.

As shown in Fig. 6.6, the deformation of the blank was completed within 0.1 to 0.2 seconds, leading to a small temperature decreasing. In contrast, the temperature of the blank decreased dramatically in the subsequent quenching stage, resulting into high post-form strength of the formed components. Meanwhile, the application of the lubricant enhanced the quenching rate significantly due to the increased IHTC value. This proved that the application of a lubricant with high thermal conductivity is beneficial for achieving a larger IHTC value and reducing the requirement of the press machine. Furthermore, the good agreement between the simulated and experimental temperature evolutions shown in Fig. 6.6 indicated that the predicted IHTC evolutions for AA7075 and thus the IHTC model were validated by the hemispherical dome forming tests.

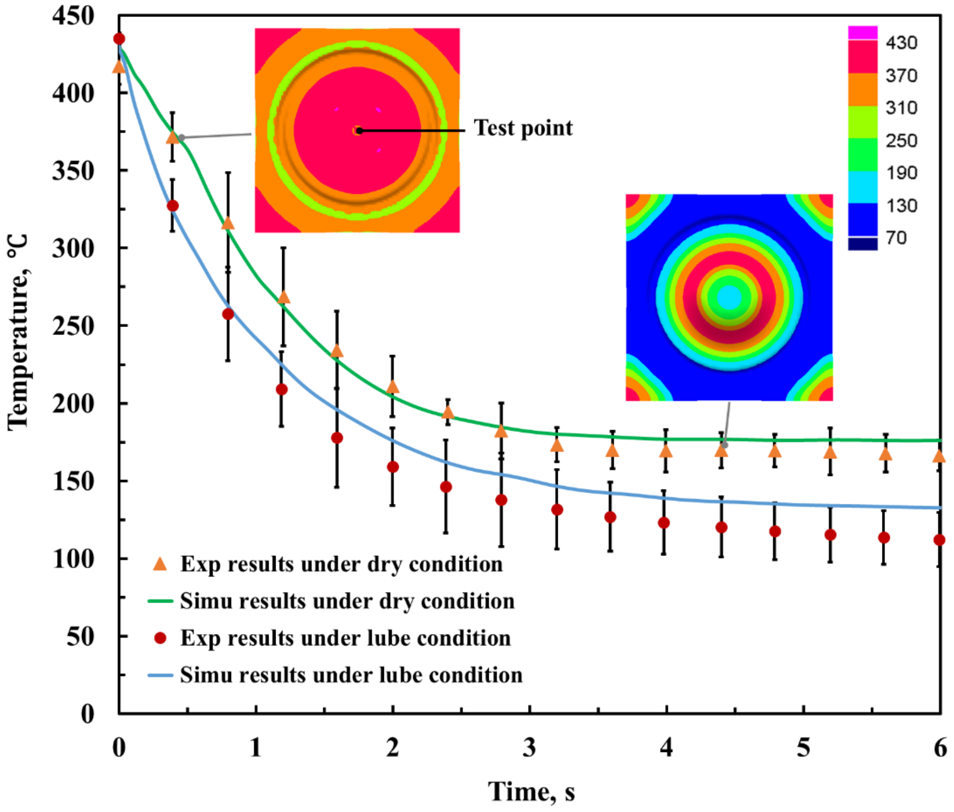

Fig. 6.6. Experimental and simulated temperature evolutions for the hemispherical dome forming tests under dry and lubricated conditions for AA7075.

6.3 B-pillar forming tests

6.3.1 B-pillar test procedure

As shown in Fig. 6.7, the tools developed by Liu et al. [19] for the B-pillar forming tests comprised a blank with a contact surface of 310 x 200 mm^2, a blankholder, a punch and a die. In order to monitor the temperature for each test, a pair of thermocouples was embedded 110 mm away from the short edge and 10 mm away from the long edge of the blank, and then connected to a thermometer. Prior to each forming test, the same graphite lubricant was sufficiently applied onto the tool surfaces, ensuring that the peak IHTC value could be reached. Dry conditions were not applied in the B-pillar forming tests to avoid damage to the tools.

The experimental procedures of the B-pillar forming tests were similar to those of the hemispherical dome tests. A blank was firstly heated up to its SHT temperature, soaked for several minutes in a furnace, and then transferred quickly onto the blankholder. When the temperature of the AA7075 blank decreased to 420℃, the punch was instantly moved towards the static cold die at a stamping speed of 400 mm/s. Subsequently, the blank was compressed between the punch and blankholder, and then deformed by the static die into a B-pillar shape. After compression for 20 seconds, the punch and the blankholder were moved back to their initial positions. Forming trials were also conducted on AA6082 at a temperature of 490℃ and stamping speed of 75 mm/s. The initial temperature of the tools was maintained at 25˚C before each forming test.

Table 6.1. Processing parameters in the hemispherical dome and B-pillar FE simulations

Processing parameters	Hemispherical dome	B-pillar
Quenching duration (s)	20	
Friction	0.3	
Initial tool temperature (˚C)	25	
Blankholding force (kN)	20	
Die closing force (kN)	50	100
Initial blank temperature (˚C)	430 (AA7075)	420 (AA7075) 490 (AA6082)
Stamping speed (mm/s)	75 (AA7075)	400 (AA7075) 75 (AA6082)

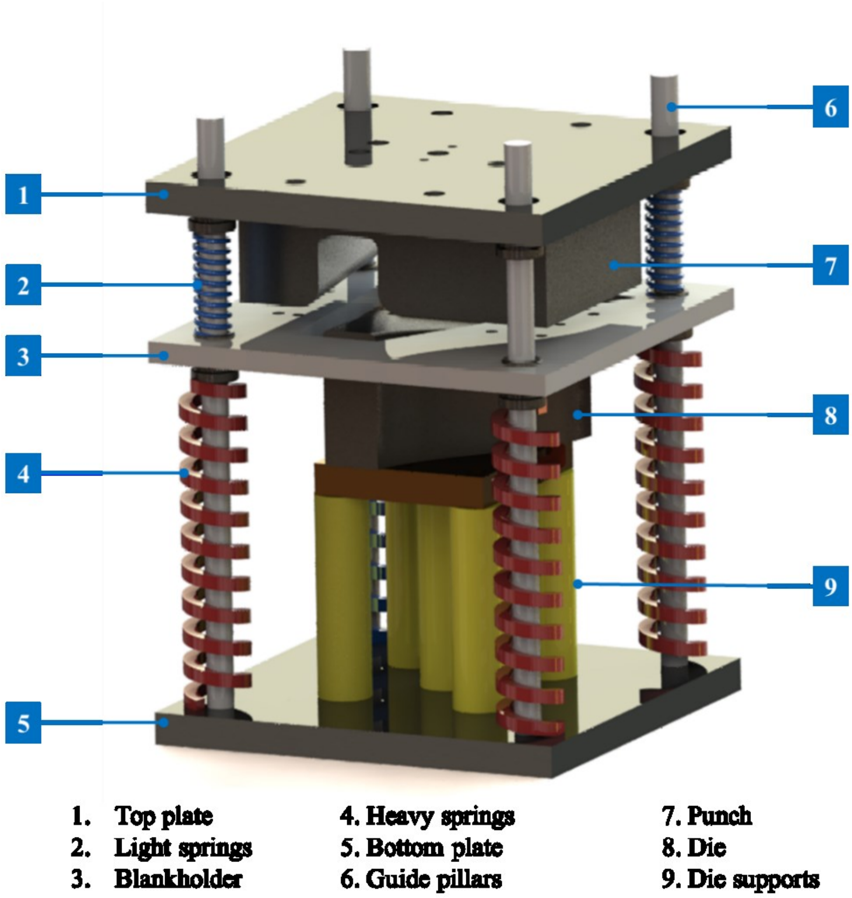

Fig. 6.7. Structure of the B-pillar forming tools.

6.3.2 FE simulation setup of the B-pillar tests

In order to simulate the B-pillar forming tests, a FE model was also built up in PAM-STAMP. The dimensions of the blank and tools were the same as those used in the experiments, as shown in Fig. 6.8. The same quadrangle thermal shell elements with a size of 2 mm were used for the blanks in the FE simulations of the B-pillar tests. The processing parameters in the FE simulations, e.g. initial temperature, stamping speed, and blankholding and die closing forces, were also the same as those in the experiments, as shown in Table 6.1. Meanwhile, the predicted IHTC evolutions for AA7075 and AA6082 with contact pressure using P20 tools under fully-lubricated conditions were implemented in the FE simulations to simulate the temperature evolutions of the blank during forming. Although the friction coefficient affected the drawability of the blank during forming, its influence was of no interest to the present research.

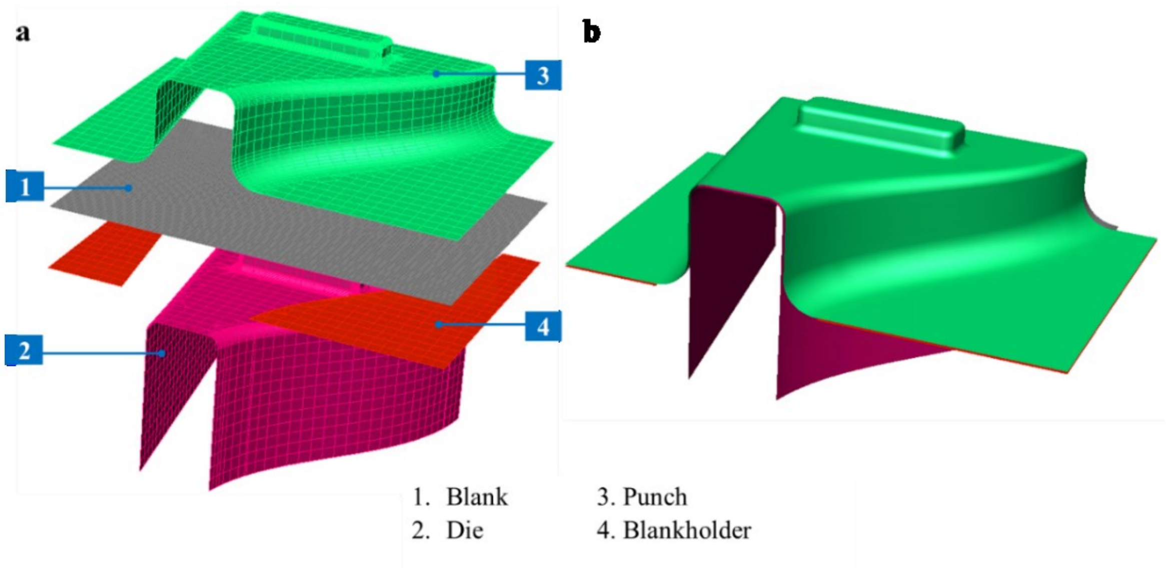

Fig. 6.8. FE model of the B-pillar forming test in PAM-STAMP under (a) the loading condition; (b) the forming condition.

As shown in Figs. 6.9 and 6.10, the stamping period of the B-pillar forming was longer than that of the hemispherical dome forming due to a larger forming depth. Similarly, the cooling rate of the B-pillar components during the stamping stage was small and became considerable during the subsequent quenching stage. Furthermore, the simulated temperature evolutions for the AA7075 and AA6082 blanks agreed well with the experimental curves, indicating that the IHTC evolutions for different aluminium alloys were accurately predicted by the IHTC model. It should be noted that the temperature dropped faster for AA7075 due to its larger thermal conductivities. In addition, AA6082 blanks used in this section were tailor-welded, leading to the uniform temperature distribution shown in Fig. 6.10.

The determined IHTC results and the developed IHTC model were validated by the IHTC tests with the 3-stage variable contact pressure, as well as the hemispherical dome and B-pillar forming tests. Therefore, the developed IHTC model enables the accurate predictions of IHTC evolutions for aluminium alloys under different conditions, which could be then implemented in FE simulations to simulate quenching processes precisely.

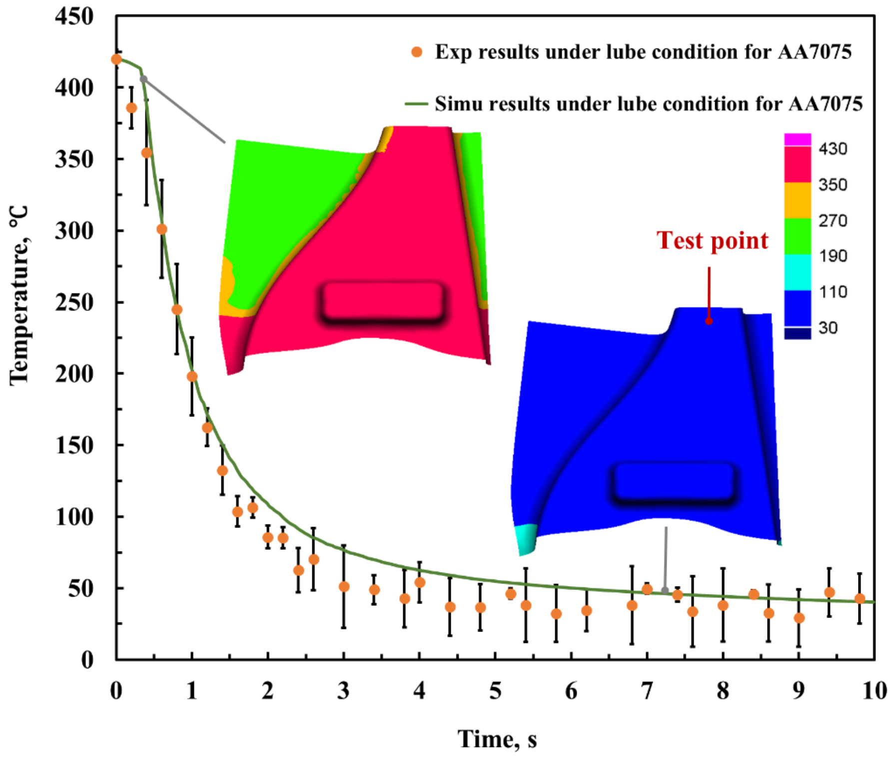

Fig. 6.9. Experimental and simulated temperature evolutions for the B-pillar forming tests under fully-lubricated conditions for AA7075.

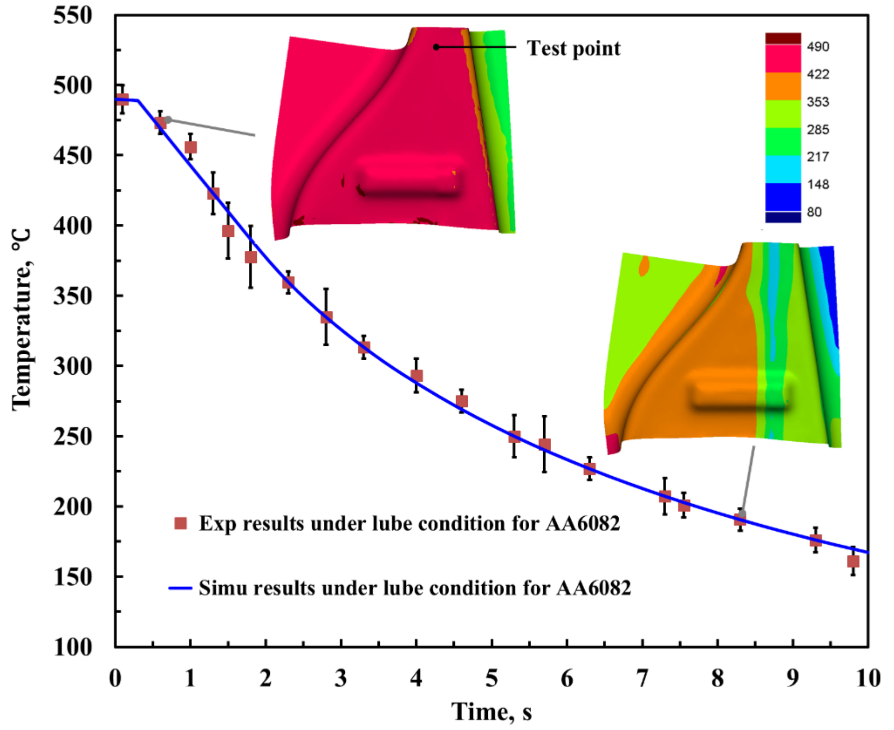

Fig. 6.10. Experimental and simulated temperature evolutions for the B-pillar forming tests under fully-lubricated conditions for AA6082.

6.4 Hot stamping of high strength aluminium panel components with complex structures

This case study aimed to successfully form a complex-shaped panel component using HFQ. This involved characterisation of the properties of the material provided, as well as other parameters of the forming process, the results of which were used in the development of advanced predictive models. These models could subsequently be input into FE simulations of the HFQ process to enhance the accuracy and reliability of the results. As the full-sized component could not be formed given the available facilities, a scaled down demo component was designed, and tooling was prepared such that forming trials could be conducted. Upon verification of the developed FE and predictive models using a successfully formed demo component, a processing window was proposed for producing the full-sized component on an industrial scale. The HFQ process was first detailed, followed by the material property tests that were conducted on the provided material. Uniaxial tensile tests at elevated and room temperatures were carried out to determine the flow stresses at different temperatures and strain rates. The stress-strain data were then used to calibrate a viscoplastic dislocation-density based constitutive model, for input in a FE simulation of the forming process for the component. Formability tests at different elevated temperatures and stamping speeds were also conducted, providing the forming limit under various conditions, and the results of which were used to calibrate a unified viscoplastic Hosford M-K model for predicting the incidence of necking. Interfacial heat transfer coefficient (IHTC) and friction tests were described subsequently, the results of which were used to assign the IHTC and friction coefficient values in the FE simulations to accurately predict temperature evolution and lubricant wear. Ageing tests were also covered to confirm whether a high post-form strength in the formed component was obtained. This was followed by the development of a demo component that represented a scaled-down version of the panel component, for which simulations were conducted to determine the optimal forming parameters and blank shape. Upon validation of the predictive and FE models, the HFQ forming process of the full-sized panel component could be simulated. The full setup of the model and the numerous simulations performed to optimise the blank shape, drawbeads and other parameters, to achieve a formed component with high geometrical accuracy and acceptable levels of thinning and wrinkling, were covered. Only partial results are shown in this section due to the confidentiality agreement.

6.4.1 Stress-strain curves and modelling

Tensile tests at elevated temperature were carried out on a Gleeble 3800 thermo-mechanical testing machine such that stress-strain results can be generated for the material efficiently. However, the Gleeble is only suitable for high-temperature conditions under which significant deformation occurs. At room temperature, particularly for a higher strength alloy such as AA6082 where the failure strains are lower, better results could be obtained by conducting the tensile test on an Instron machine using DIC techniques.

According to the standard of BS EN ISO 6892-1, the specimen was machined into a dog-bone shape using laser cutting from the AA6082 sheet. Prior to each test, the width and thickness of the specimen were measured at three different locations and recorded, such that the stress and strain during each test could be calculated after post-processing of the results. After each test, the evolution of the gauge length measured and recorded using the DIC software ARAMIS was used to calculate the average strain, using the following equations:

Engineering strain, $e = \frac{\left(L - L_0\right)}{L_0}$ (6.1)

True strain, $\varepsilon = \ln(1+e)$ (6.2)

Load-displacement data, recorded by the oscilloscope, was used to calculate the stress.

Engineering stress, $\delta = \frac{F}{A_0}$ (6.3)

True stress, $\sigma = \delta(1+e)$ (6.4)

Fig. 6.11 demonstrates an AA6082 tensile test result at room temperature at a strain rate of 0.001/s. The tensile strength and proof stress at 0.01 strain were 308 and 338 MPa respectively, significantly larger than those at elevated temperatures. However, the failure strain was only 0.16. The tensile tests at elevated temperatures were conducted using a Gleeble 3800 machine. Fig. 6.12 displayed the stress-strain curves at different deformation temperatures at a strain rate of 1 s^{-1}. The flow stress and strain hardening decreased with increasing temperature, while the failure strain increased. The proof stress at a true strain of 0.1 decreased from approximately 84.1 MPa to 39.3 MPa as the deformation temperature increased from 350°C to 535°C; a similar trend was also observed for the evolution of the tensile strength with temperature. The ductility of the material increased, and the flow stress decreased with increasing temperature due to thermally activated mechanisms that became more prominent as the temperature was increased, such as grain boundary sliding and recovery processes.

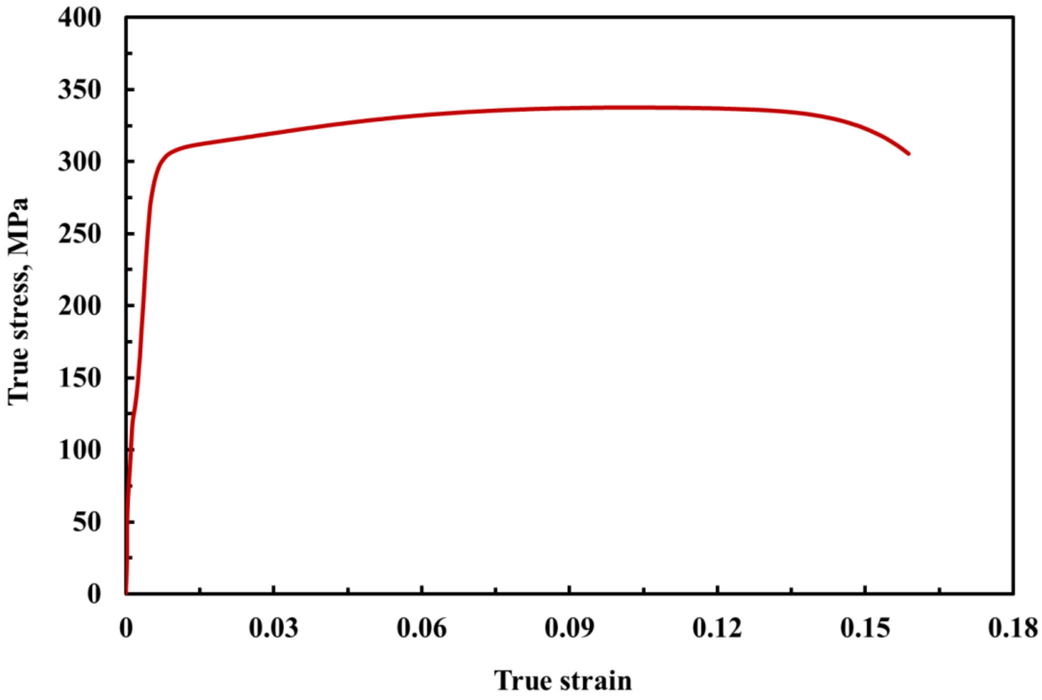

Fig. 6.11. AA6082 tensile test result at room temperature at a strain rate of 0.001/s.

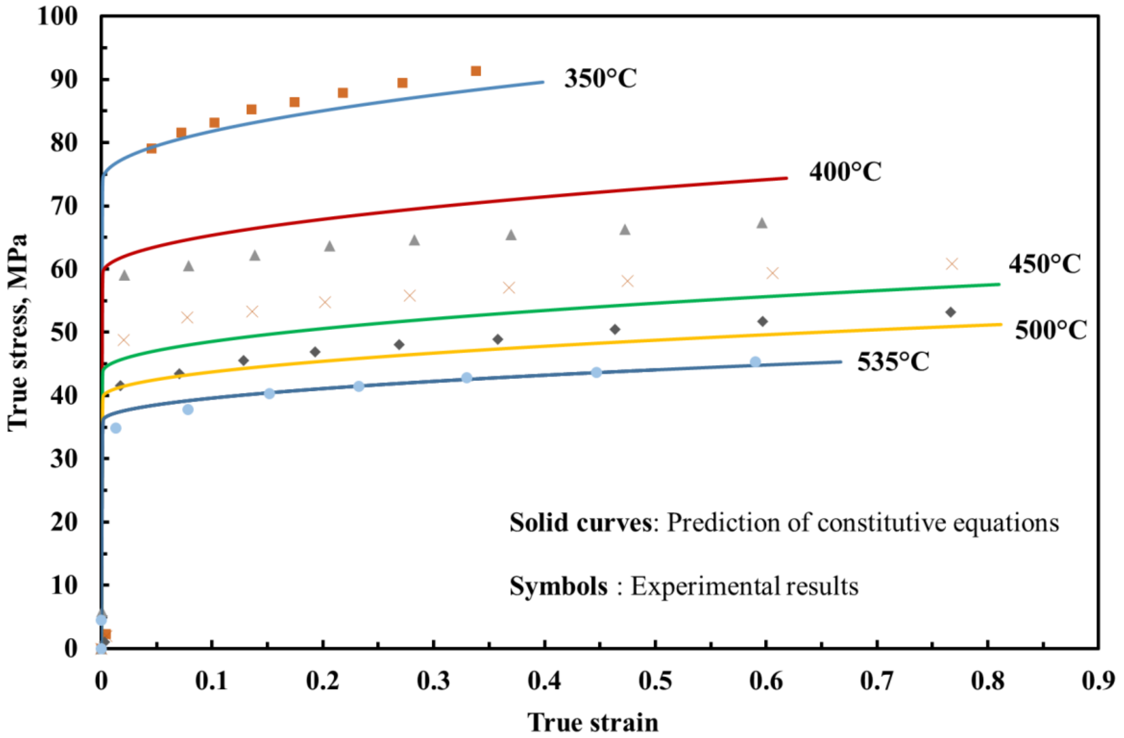

Fig. 6.12. Predicted and experimental stress-strain curves for AA6082 at a strain rate of 1/s at different temperatures.

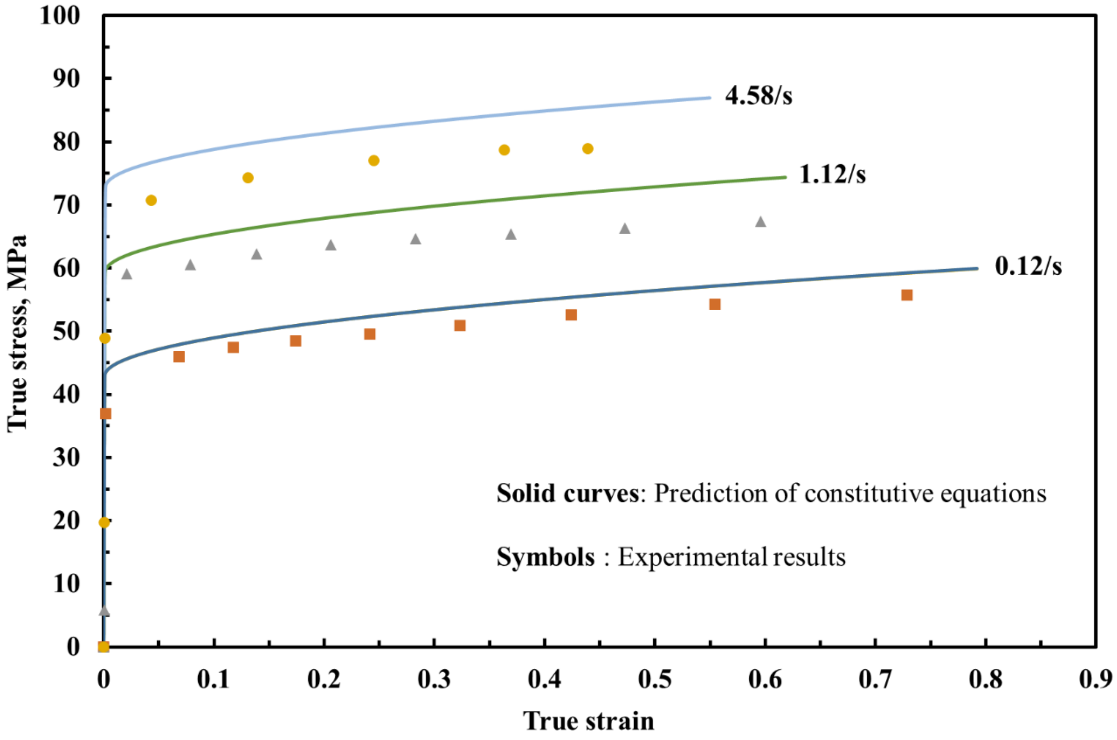

Fig. 6.13. Predicted and experimental stress-strain curves for AA6082 at 400°C at different strain rates.

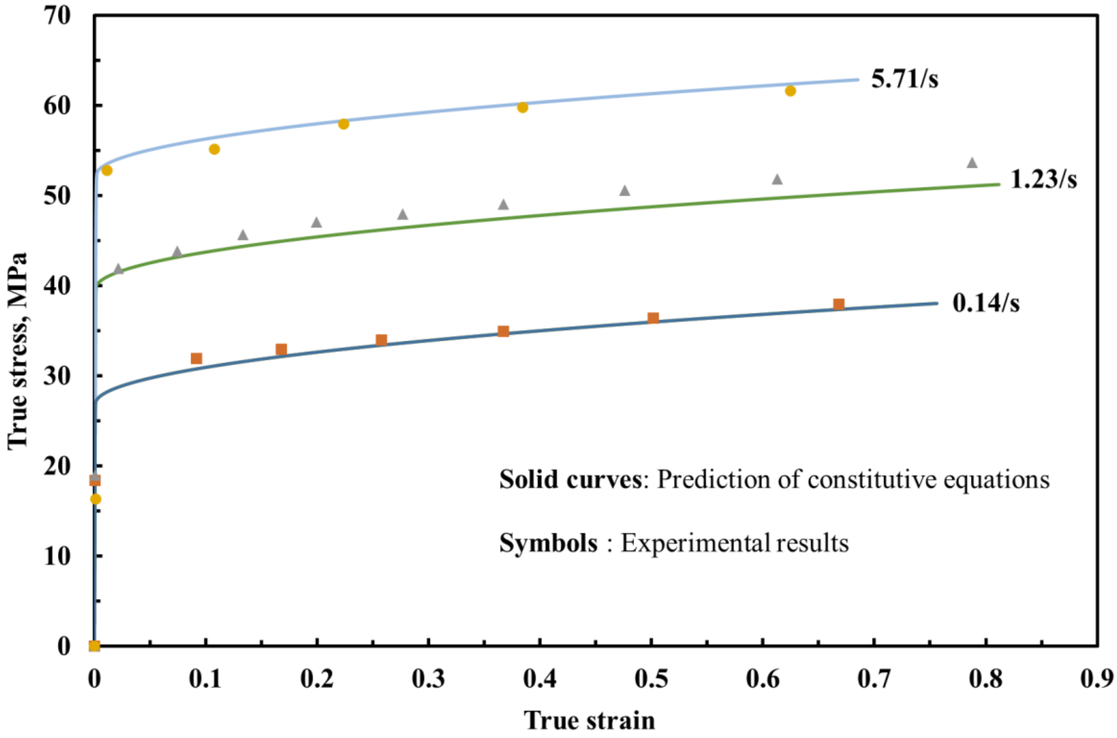

Fig. 6.14. Predicted and experimental stress-strain curves for AA6082 at 500°C at different strain rates.

Figs 6.13 and 6.14 showed the tensile test results at different strain rates at the deformation temperatures of 400°C and 500°C respectively. The higher flow stresses with increasing strain rate demonstrated the viscoplastic behaviour of the material. At 400°C, the proof stress at 0.1 true strain increased from approximately 46.8 MPa to 73.1 MPa as the strain rate increased from 0.1 to 5 s^{-1}, while at 500°C, it increased from 32 MPa to 54.9 MPa. This was the characteristic of strain rate hardening, and a similar trend was also observed in the evolution of the tensile strength with strain rate.

At higher strain rates, there was less time for recovery processes to occur; consequently, the material was stronger. The increasing accumulation of dislocations also resulted in greater hardening, leading to higher tensile strengths at higher strain rates. At lower strain rates, the increased grain growth competed with other mechanisms and resulted in a lower ductility. As the strain rate increased further to 5 s^{-1}, the mechanism of increased hardening dominated, and the ductility slightly decreased.

The equations used in this work formed part of a unified set of viscoplastic equations developed previously by Lin et al. [87], which was based on dislocation density hardening laws and incorporated thermally activated mechanisms. The temperature-dependent constants of the equations were able to capture the variation in the behaviour of the material at elevated anisothermal temperatures experienced during the HFQ forming.

The equations were derived by assuming that the flow stress of the material could be described as a function of both the plastic strain and plastic strain rate using a power law.

$$\bar{\sigma} = K\bar{\varepsilon}_p{}^{n}\dot{\varepsilon} \tag{6.5}$$

where K is a temperature-dependent material constant, n is the strain-hardening exponent and m is the strain-rate hardening exponent. The viscoplastic flow rule was obtained by rearranging Eq. 6.6 as follows.

$$\dot{\varepsilon} \qquad \bar{\varepsilon}_P^{n})^{1/m} \tag{6.6}$$

To account for dislocation density-based hardening and thermally activated mechanisms, the isotropic hardening variable R and dynamic yield point k were incorporated in the viscoplastic flow.

$$[illegible] \left(\frac{R-k}{K} \right)^{n_1} \tag{6.7}$$

Garrett et al. [4] expressed the isotropic hardening *R* as a function of the evolution of the normalised dislocation density $\bar{\rho}$ in the material, which varies from 0 in the initial state to 1 in the saturated state. This expression was integrated to obtain Eq. 6.8, which presented a proportional relationship between the isotropic hardening and dislocation density.

$$R = B\bar{\rho}^{0.5} \tag{6.8}$$

where *B* is a temperature-dependent material constant.

The rate of the change of the normalised dislocation density was expressed by Eq. 6.9, where *C* is a temperature-dependent material constant, and *A* and n_2 are temperature-independent constants. The effects of dynamic recovery and plastic strain on the dislocation density were captured by the term on the left, while the static recovery was represented by the term on the right.

[illegible] (6.9)

The resulting flow stresses were calculated according to Eq. 6.10, where *E* is Young's modulus of the material at elevated temperatures.

$$\bar{\sigma} = E(\bar{\varepsilon} - \bar{\varepsilon}_{\mathrm{P}}) \tag{6.10}$$

Arrhenius equations were used to express the temperature-dependent constants, which could be calibrated using the results of the uniaxial tension tests.

The results of the uniaxial tensile tests on AA6082 were used to calibrate the equations and determine the fourteen unknown constants. This was done by solving the equations using an explicit forward Euler method and varying the constants to obtain the best fit to the data, the resulting values for which were presented in Table 6.2.

Figs 6.12 to 6.14 showed the close agreement that was achieved between the experimental and numerical flow stress data, at different temperatures and strain rates. It should be noted that the final stages of deformation were not predicted as the damage was not modelled in the equations outlined above, which was done previously using continuum damage mechanics in work by Mohamed et al. [69]. However, the developed unified constitutive equations would enable the prediction of stress-strain curves at different temperatures and strain rates for AA6082.

Table 6.2. Material constants in the viscoplastic damage constitutive equations for AA6082

E_0 (MPa)	C_0 (s^{-1})	k_0 (MPa)	K_0 (MPa)	n_0 (-)
2328.55	25.51	2.83E-08	2.16	1.363
Q_E (J/mol)	Q_C (J/mol)	Q_k (J/mol)	Q_K (J/mol)	Q_B (J/mol)
14986.25	-1425.08	62598.4	18384.21	11683.86
Q_n (J/mol)	Q_A (MPa)	B_0 (MPa)	A_0 (-)	R (J/molK)
9061.22	11793.55	19.36	0.00225	8.31

6.4.2 Forming limit curves (FLC) and modelling

Fig. 6.15 (a) showed the effect of temperature on the formability of AA6082, at a forming speed of 250 mm/s. It could be deduced that the FLC was V-shaped and non-symmetric about the plane strain line, which has also been obtained from high-temperature formability tests on other aluminium alloys [88] and magnesium alloys [89] in the literature.

Formability increased with increasing temperature, with an increase of approximately 80% and 64% in the plane and biaxial major limit strains respectively as the temperature was increased from 300 to 450°C. In general, higher temperatures were conducive to achieve better ductility in AA6082, which was translated to improved formability. The strain rate hardening of the material was enhanced at higher temperatures, thus delaying the onset of localised necking. The same trend was also observed with the limit dome height measured from the specimens, which increased with increasing temperatures. The effect of forming speed on formability is shown in Fig. 6.15 (b) at a temperature of 400°C. Formability was found to increase with decreasing strain rate, although there was a small difference between the forming speeds of 400 and 250 mm/s. The plane and biaxial major limit strain increased by up to 10% and 5%

respectively when the forming speed was reduced from 400 to 250 mm/s, while they increased by 20% and 35% further respectively when the forming speed was decreased to 75 mm/s. This trend was again captured by the limit dome height measurements, which had a decreasing trend with increasing forming speed.

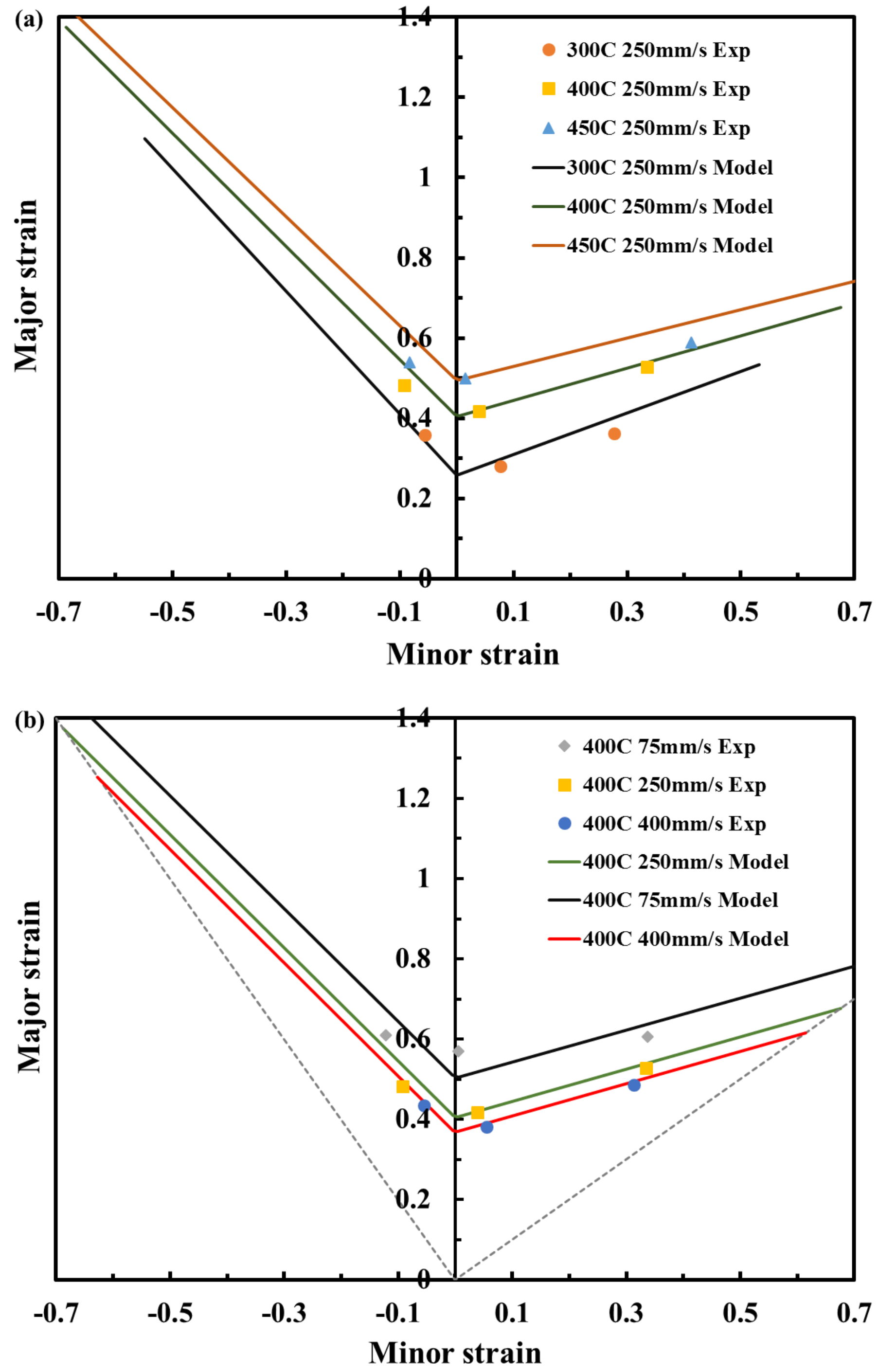

Fig. 6. 15. FLDs for AA6082 (a) at different elevated temperatures; and (b) at different forming speeds.

The results of the formability tests were used to calibrate a developed model for the prediction of necking, as described in the following section. This model would greatly enhance the accuracy and reliability of the FE simulations conducted on the HFQ forming of the locomotive component. The M-K model, developed by Marciniak and Kuczynski in 1967 [90], is the most widely used approach for the generation of FLCs for highly ductile alloys [91], in which the nature of fracture is due to diffuse necking. In the M-K model, a pre-existing imperfection zone was assumed, where the material thickness in this region, designated zone B, was less than that of the rest of the material, designated zone A.

The initial discrepancy in the thickness was accounted for through the use of a non-homogeneity coefficient or imperfect factor *f*. To determine the evolution of the strains in zone B, it was assumed that there was compatibility of strains at the interface between zones A and B where the minor strains were equal to each other and that there was mechanical equilibrium along with their interface. The strains in both zones were calculated until the ratio of the major strain increment or the thickness strain increment between zones B and A reached a critical value of 10, as adopted by Graf and Hosford [92], and Cao et al. [93]. At this point, deformation in zone B increased at a much faster rate than zone A, resulting in necking and subsequent failure. The defining equations of the M-K model are therefore as follows.

$$\varepsilon_{2A} = \varepsilon_{2B} \tag{6.11}$$

$$\sigma_{1A} = f\sigma_{1B} \tag{6.12}$$

$$f = t_B / t_A \tag{6.13}$$

$$f = f_0 \exp(\varepsilon_{3B} - \varepsilon_{3A}) \tag{6.14}$$

$$\frac{d\varepsilon_{1B}}{d\varepsilon_{1A}} \geq 10, or \frac{d\varepsilon_{3B}}{d\varepsilon_{3A}} \geq 10 \tag{6.15}$$

The model that was used in this work for the prediction of necking and subsequently the FLDs, under varying temperature, strain rate and strain path conditions, unified the viscoplastic, Hosford and M-K model equations [6]. The viscoplastic equations were modified such that they could be applied to both zones A and B, and therefore had the variables *'A, B'* in their indices, and combined and solved simultaneously with the M-K model equations, in order to determine the strains and stresses.

$$\left(\frac{\bar{\sigma}_{(A,B)} - R_{(A,B)} - k}{K} \right)^{n_1} \tag{6.16}$$

$$R_{(A,B)} = B\bar{\rho}_{(A,B)}^{0.5} \tag{6.17}$$

(6.18)

$$\bar{\sigma}_{(A,B)} = E(\bar{\varepsilon}_{(A,B)} - \bar{\varepsilon}_{\mathrm{P}(A,B)}) \tag{6.19}$$

In the calculation procedure, the major strain in zone A was first incremented at each time step according to the major strain rate using an explicit forward Euler method. The minor strain was calculated at each time step using the value for β, which was the ratio between the minor and major strain increments (the principal strain ratio). This was set to the required constant value according to the strain condition being investigated (e.g. -0.5 for uniaxial, 0 for plain or 1 for biaxial strain) for the construction of FLCs where a linear strain path was assumed. However, in general, the expression for the principal strain ratio could be used to account for the non-linear strain paths and non-constant values of β that occurred in real forming processes. The equations that modelled the viscoplastic deformation of the material were subsequently solved at the temperature of interest.

By assuming plane stress conditions, the stress in the thickness direction was set to zero, and the minor stress could be calculated. Thus, all the strain and stress components in zones A and B could be determined using these equations, and Eq. 6.15 was solved to determine whether necking or failure has occurred. This process was repeated to generate different points on the FLC. Through assigning a value of imperfect factor f, the FLDs for AA6082 were predicted successfully at different temperatures and forming speeds with good agreement with the experimental results, as shown in Fig 6.15, enabling the accurate prediction of failure in the simulations. The imperfect factor f values under different conditions are shown in Table 6.3.

$$f = 1.045 + 7.2e - 5 \cdot T - 0.028 \cdot \log(T) - 0.0145 \cdot \log(SR) \tag{6.20}$$

where T is the temperature and SR is the strain rate.

Subsequently, the equation of '*f*' as a function of temperature and strain rate was calibrated and shown in Eq. 6.20. This would enable the limit strains to be determined for other combinations of forming temperature and speed.

Table 6.3. The imperfect factor *f* under different conditions.

Speed (mm/s)	**Temperature**	**Strain rate**	***f***
250	300	5.97	0.986
75	400	2.04	0.995
250	400	5.91	0.99
400	400	8.82	0.987
250	450	6.11	0.992

6.4.3 Friction test

The friction tests were conducted using an Anton Paar pin-on-disc tribometer. It was found that the evolution of friction can be divided into three stages according to the different coefficients of friction. In Stage I, the coefficient of friction was low and stable, with an average value of approximately 0.2, as shown in Fig. 6.16. No wear scar was observed in this stage.

In Stage II, the coefficient of friction started rising rapidly from about 0.2 and gradually slowed down to a value of 0.7. In this regime, the coefficient of friction was highly variable and unstable because the friction stems from fracture phenomena at the surface. The friction force was supposed to be generated from interacting asperities, which were mainly caused by the asperities deforming and fracturing into wear particles. These were entrapped and generated ploughing tracks as the ball penetrates and moves along the wear track. It was found that the adhesive friction between the ball and the aluminium alloy disc did not play an important role in the present research since the material transfer between them was hardly observed by a microscope in the tested sliding distance. Both Stages II and III were dominated by ploughing friction due to the large hardness difference between tool steel and aluminium: the disc surface was ploughed by the hard asperities on the ball as well as the wear debris.

In Stage III, the coefficient of friction reached a plateau with an average value of 0.7. With the severe ploughing damage on the surface, many large-sized wear particles were generated and entrapped in the wear track during sliding wear. It was expected that the quantity and size of the particles generated on the track reached a dynamic balance, which might indicate the quantity of entrapped particles was equal to that being ejected from the wear track, leading to a relatively stable third body condition and a stable coefficient of friction [39].

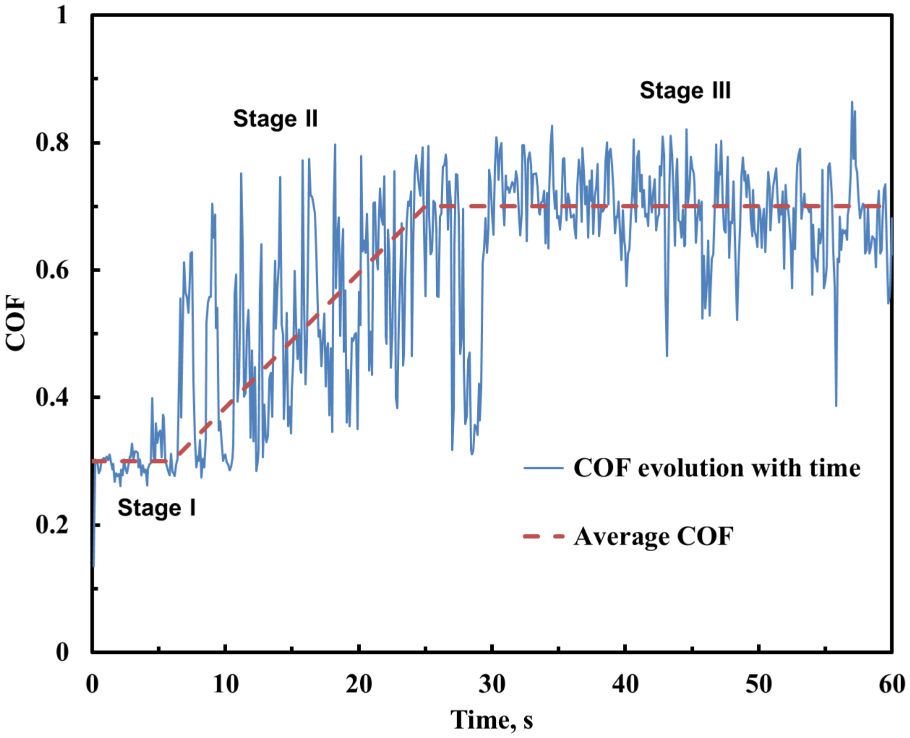

Fig. 6.16. Coefficient of friction evolution with sliding time under dry conditions.

It was found that the evolution of friction could also be divided into three stages when lubricant was applied, as shown in Fig. 6.17. In Stage I, the coefficient of friction was stable at a value of approximately 0.15, in which the two surfaces were fully separated by the lubricant film. The friction in Stage I might be primarily generated by the internal fluid shear stress of the lubricant at the interface. During sliding, the thickness of the lubricant film gradually decreased due to lubricant transferred from the ball to the aluminium disc and the lubrication mode changed from full film lubrication to a mixed lubrication regime, which was defined as a transition state between full film lubrication and boundary lubrication and in which two lubrication mechanisms might be functioning.

At the beginning of Stage II, the thickness of the lubricant decreased to the height of peaks on the aluminium surface, and the friction force consisted of two components: the friction force generated from interacting asperities, and the shearing of the remaining lubricant [94]. In Stage III, the coefficient of friction reached a plateau of 0.3. In this stage, the lubricant was almost completely removed from the contact interface and hence ploughing friction played an important role in the overall friction force.

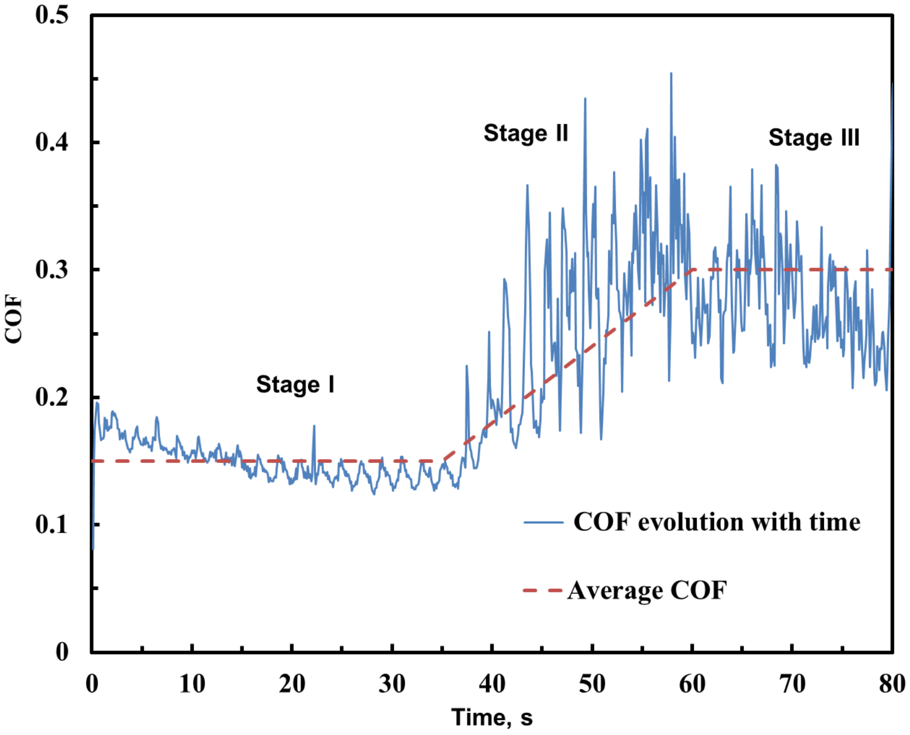

Fig. 6.17. Coefficient of friction evolution with sliding time under lubricated conditions.

When the friction test was conducted at an elevated temperature, the coefficient of friction increased dramatically at the initial stage, instead of occurring through a stable stage, as shown in Fig. 6.18. This was because the viscosity of graphite lubricant was very low at elevated temperatures, leading to a rapid decrease of the lubricant thickness at the initial stage. When the lubricant was almost removed from the contact interface, the material started transferring from the aluminium disc to the tool steel ball due to galling. This changed the contact interface conditions severely, and the coefficient of friction increased dramatically. This indicated that the lubricant service life at elevated temperatures is very short.

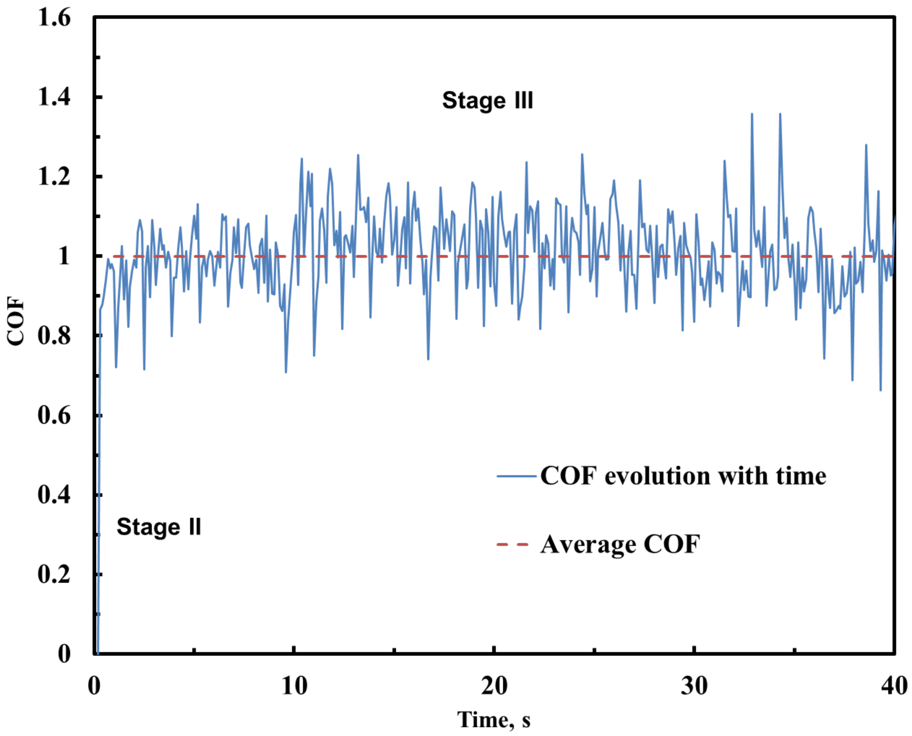

Fig. 6.18. Coefficient of friction evolution with sliding time under lubricated conditions at elevated temperature.

6.4.4 FE simulation of the hot stamping of the aluminium panel component

The die was imported as an IGS file and meshed with PAM-STAMP's meshing module, DeltaMESH, according to the selected simulation strategy. The blankholder and punch were created by offsetting the surfaces of the die geometry. The mesh size for the tools was set to 10 mm; this ensured that the complex geometry of the part could be captured and that the heat transfer and contact between the blank and the tool parts could be modelled as accurately as possible. The tool parts were set up as rigid bodies such that they would not undergo any deformation, hence saving on computational time, as shown in Fig. 6.19.

The blank was meshed with 4-node Belytschko-Tsay shell elements with an initial size of 3 mm, and the initial shape of the blank was designed by creating an outline that was offset from the edges of the die cavity and imported into PAM-STAMP as an IGS curve. The selected element size was sufficient for capturing the curvature of the outline, and thus the blank could be successfully meshed. The created blank was positioned in the forming tool as shown in Fig. 6.20. A new coordinate system was also created with positive z-axis in the stamping direction, which was required by the software. Three positioning tabs were also added to the blank shape to ensure that the positioning of the blank in the experiments and the simulations was as accurate and consistent as possible. The tabs would not have a significant effect on the deformation of the blank during the forming process.

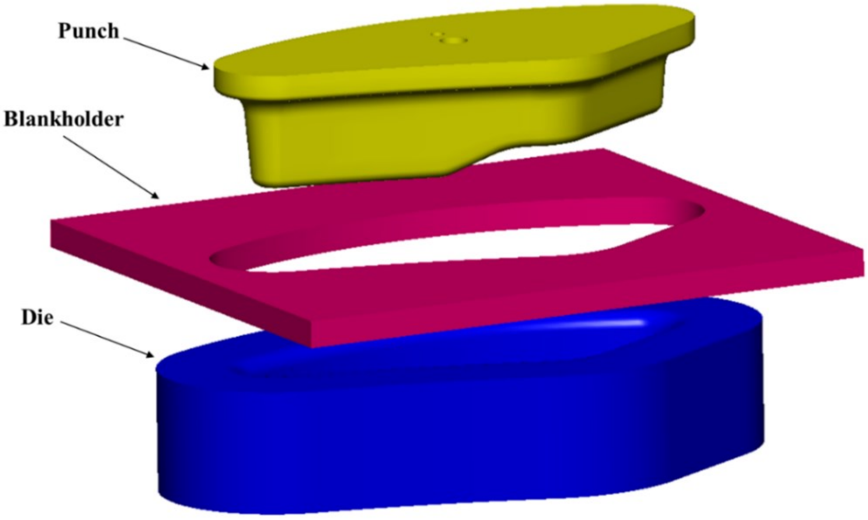

Fig. 6.19. The FE model of the tool setup.

Simulations in PAM-STAMP were divided into multiple stages that covered different aspects of a forming process; the results of each stage constituted the initial conditions of the subsequent stage. In the gravity stage, the blank was firstly positioned on the bottom blankholder, and any sagging was accounted for. This was followed by the holding stage, which simulated the action of the top blankholder moving towards the bottom blankholder and clamping the blank in-between. The top blankholder was assigned a velocity that equalled to the forming speed being simulated, and the stage was terminated according to a ‘pinch test’; this detected when a node in the blank was being pinched between the two tool parts and thus stopped the calculation. The final stage was the stamping stage, which simulated the action of the punch deforming the blank and was terminated according to the specified punch displacement.

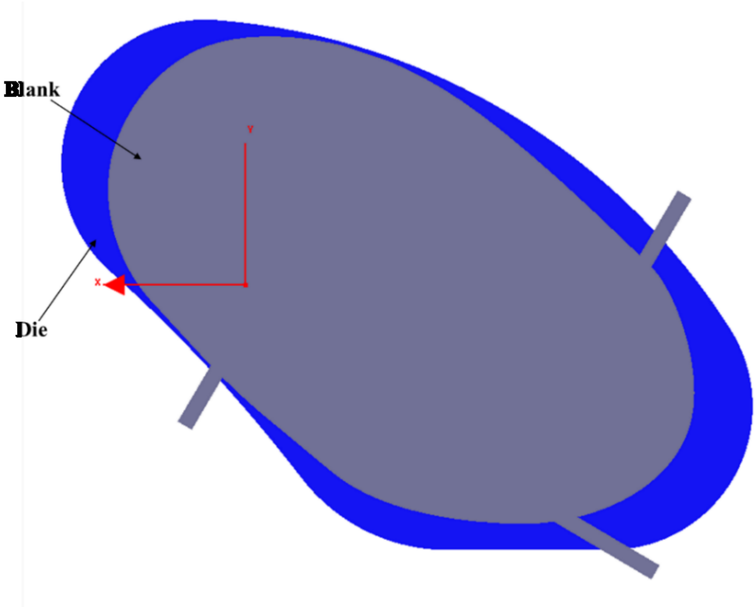

Fig. 6.20. The position of blank on the die.

Table 6.4. Simulation processing parameters

Parameter	**Amount**	**Unit**
Friction	0.3	---
Temperature of tools	20	˚C
Blankholder speed	250	mm/s
Blankholding force	5	kN
Punch speed	400	mm/s
IHTC	Model prediction	

The blank material properties were based on the models developed from the uniaxial tension and formability tests, while the tool properties were set as a tool steel from the available PAM-STAMP material library. The parameters of the simulation were set up according to the HFQ forming process and are shown in Table 6.4.

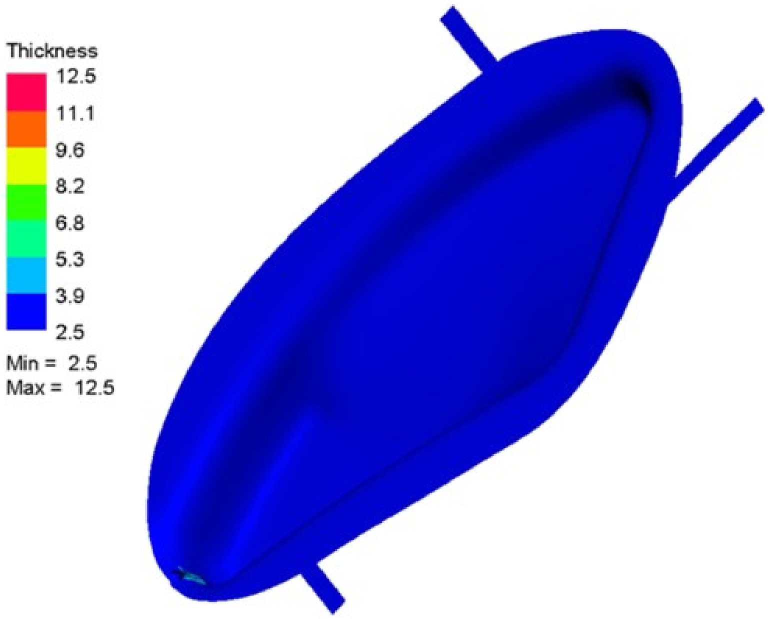

Fig. 6.21. Thinning distribution over the formed component using the initial blank shape.

The material flow and thinning during the stamping process is very sensitive to the initial blank shape. Therefore, the optimisation of the initial blank shape before conducting the real forming trials is critical. Fig. 6.21 showed the thickness distribution of the component after deformation, using the first version of the initial blank shape. Severe wrinkling occurred in the corner with larger depth, caused by the insufficient material around that area. Severe wrinkling must be avoided, in order to protect the tools and improve the component quality. This can usually be resolved by increasing the amount of material in such areas; however, this could also result in an increase in thinning due to the drawability of the material being restricted. Therefore, the optimisation process should be performed very carefully, not only to remove wrinkling but also to minimise the thinning.

After simulating tens of different blank shapes to minimise the wrinkling and thinning, an optimal solution was identified. The thinning distribution of the component using the optimised blank shape is shown in Fig. 6.22. The maximum thinning occurring at the corner with a larger depth reached approximately 47%, while the thinning at the opposite corner reached approximately 28%. Slight wrinkling of a 34% increase in the thickness was still visible at the top edge of the corner. Through the simulation of the numerous blank shapes, it was concluded that the wrinkling could not be completely eliminated when forming a geometry with deep pockets and narrow closed ends. However, as the wrinkling was confined to the blankholding area, this could be trimmed off following forming without affecting the geometry of the region of interest of the component. With the optimised solution identified, the AA6082 sheets were cut into the final blank shapes using laser cutting for use in the HFQ forming trials.

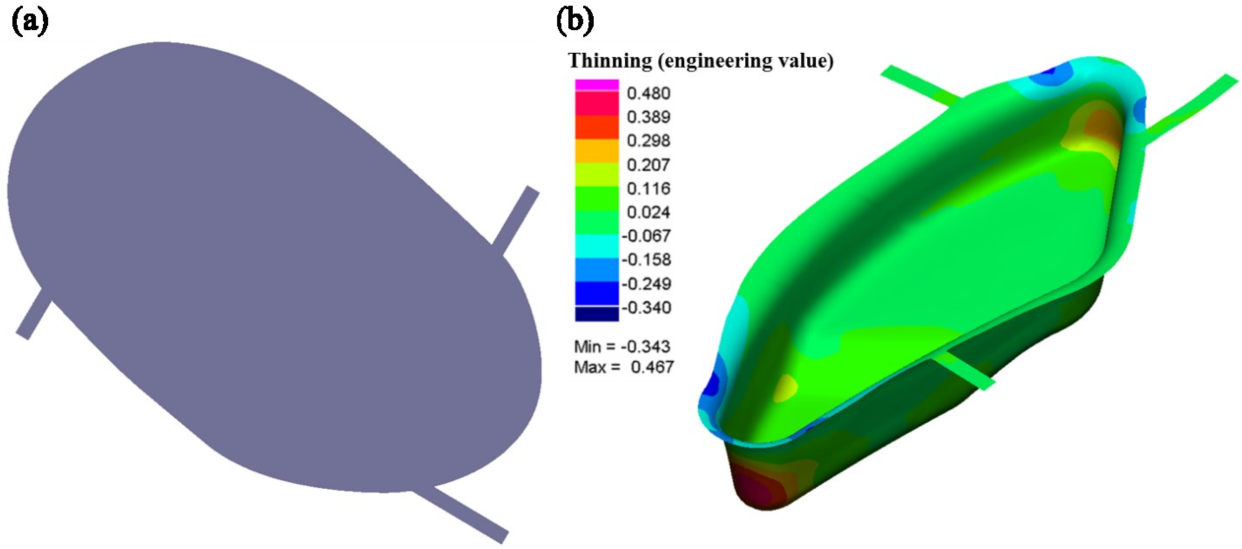

Fig. 6.22. (a) The optimised initial blank shape; (b) The thinning distribution over the formed component.

6.4.5 Hot stamping processes of the panel component

The design of the tooling for the demo component was based on an existing tool used for the forming of a B-pillar component. The tool was previously operated by placing it on the bed of a 25-tonne ESH press, which was also used for conducting the formability test. During the forming operation, the arm of the press would make contact with the top plate of the tool and provide the forming load. The setup is shown in Fig. 6.23 below. The forming speed of 400 mm/s and total stroke required to form the component was input into the control system of the press, and the SHT and ageing furnaces pre-heated to 535˚C and 190˚C respectively.

A spacer block was used to enhance the safety of the process for the operator; when it was not in place, the tooling could be lubricated, and the blank was positioned, without any danger of the tool closing, as the maximum stroke of the press arm alone would not be sufficient to reach the tool. When deformation was initiated with the block in position, the die was pressed against the blank, which was placed on the blankholder. As the springs of the tool frame were compressed, a blankholding force was provided that held the blank in between the die and the blankholder. As the die and blankholder moved further down, the blank made contact with the rigidly fixed punch, forming the blank into the desired demo component geometry.

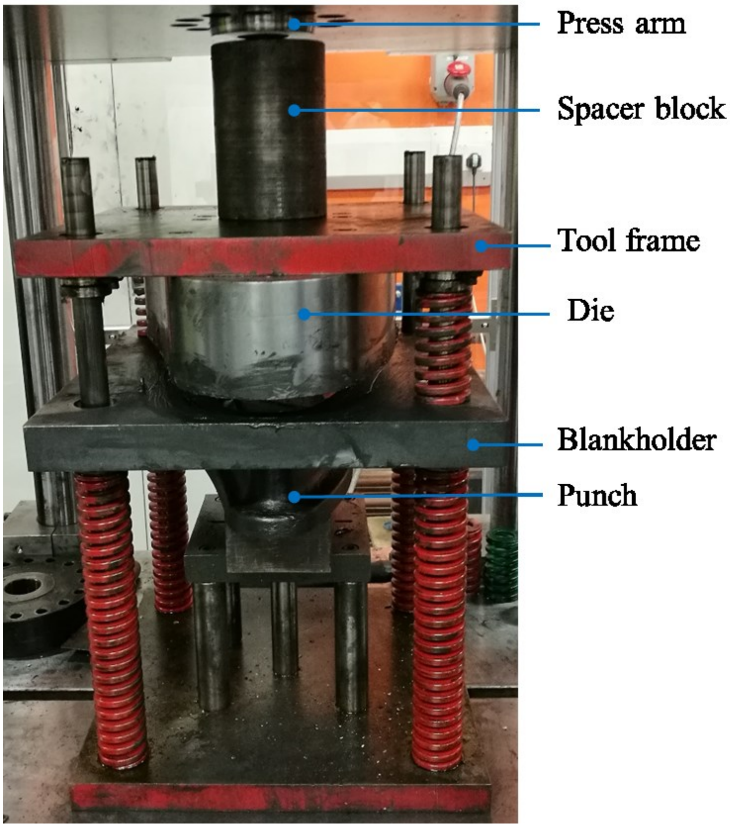

Fig. 6.23. Demo component tool setup.

The forming operation consisted of four stages. In the first stage, the blank was transferred to the SHT furnace, heated to its SHT temperature of 535˚C and soaked for two minutes, as shown in Fig. 6.24 (a). The temperature of the blank was monitored by using a thermometer. Once heated, the blank was rapidly transferred from the furnace to the press and forming immediately initiated to minimise the amount of heat loss. Once formed, the component was held under a load for 10 seconds to quench it to a low temperature; the load was subsequently removed and the component removed, as shown in Fig. 6.24 (b). The component was then transferred to the ageing oven and soaked for 6 hours to achieve its peak strength, as shown in Fig. 6.24 (c). Before each forming trial, all the surfaces of the tools were lubricated sufficiently with Omega-35 lubricant. Additionally, high-temperature gloves and other safety equipment were utilised at all times, particularly when transferring the materials at high temperature.

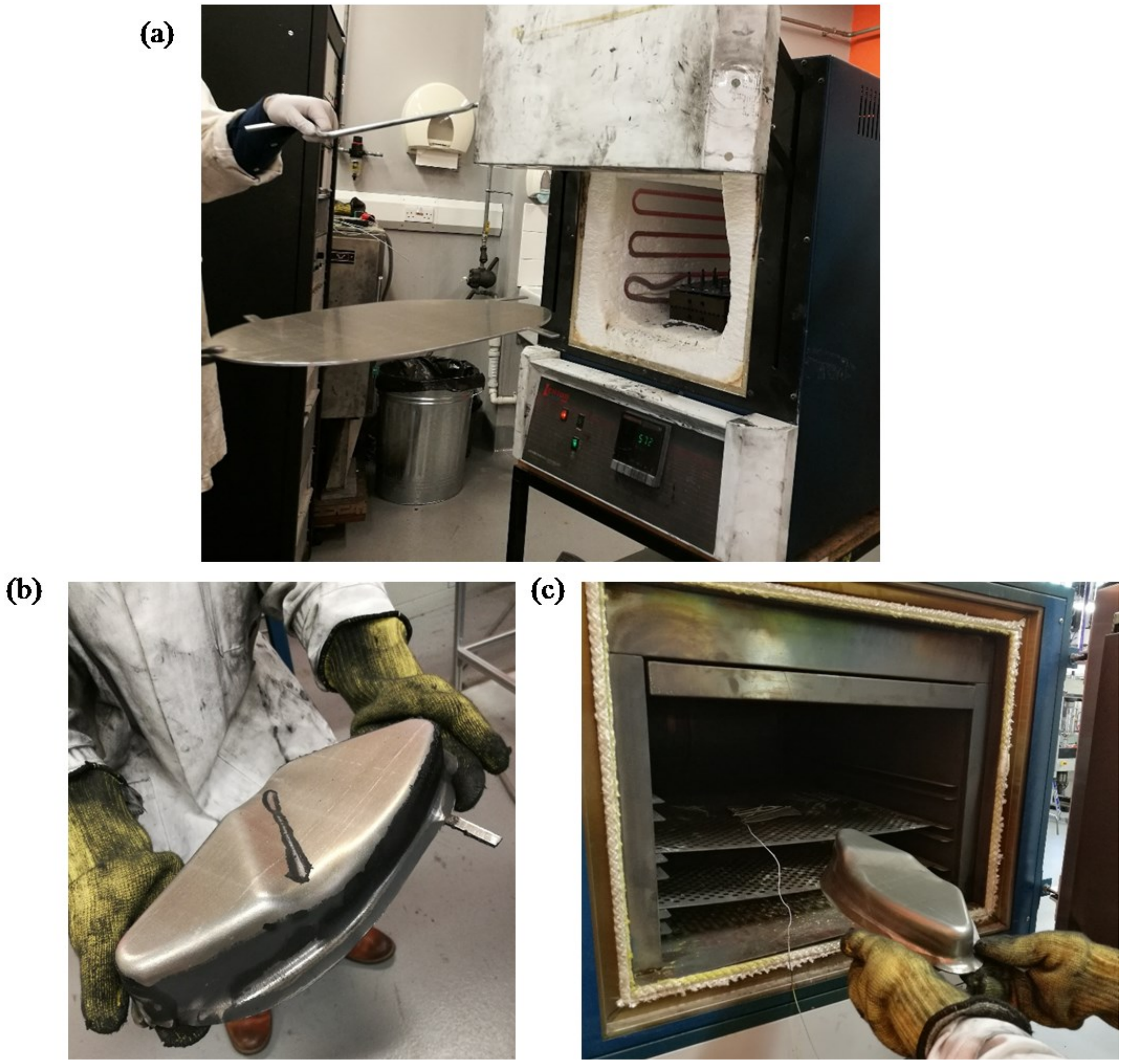

Fig. 6.24. (a) Blank heating in the furnace; (b) Example of a formed component; (c) Ageing of the formed component.

The first forming trial was conducted under cold forming conditions to highlight that the blank material could not be formed successfully at room temperature. Due to the poor formability at the room temperature, the component was severely damaged and fractured into two pieces, as shown in Fig. 6.25 (a). This indicated that the headlamp structure cannot be formed using cold forming and requires the HFQ process, which is capable of forming components with such complex shapes.

Following significant efforts to optimise the processing parameters and blank shape, the component shown in Fig. 6.25 (b) was successfully formed with a heating temperature of 535˚C, a stamping speed of 400 mm/s and a blankholding force of 5 kN. No cracking or necking occurred under such conditions. It was not possible to completely eliminate wrinkling when forming a component with narrow closed ends. The blankholder regions of the components were trimmed off along the marked line, as shown in Fig. 6.25 (c), such that the final component would be free of any wrinkling.

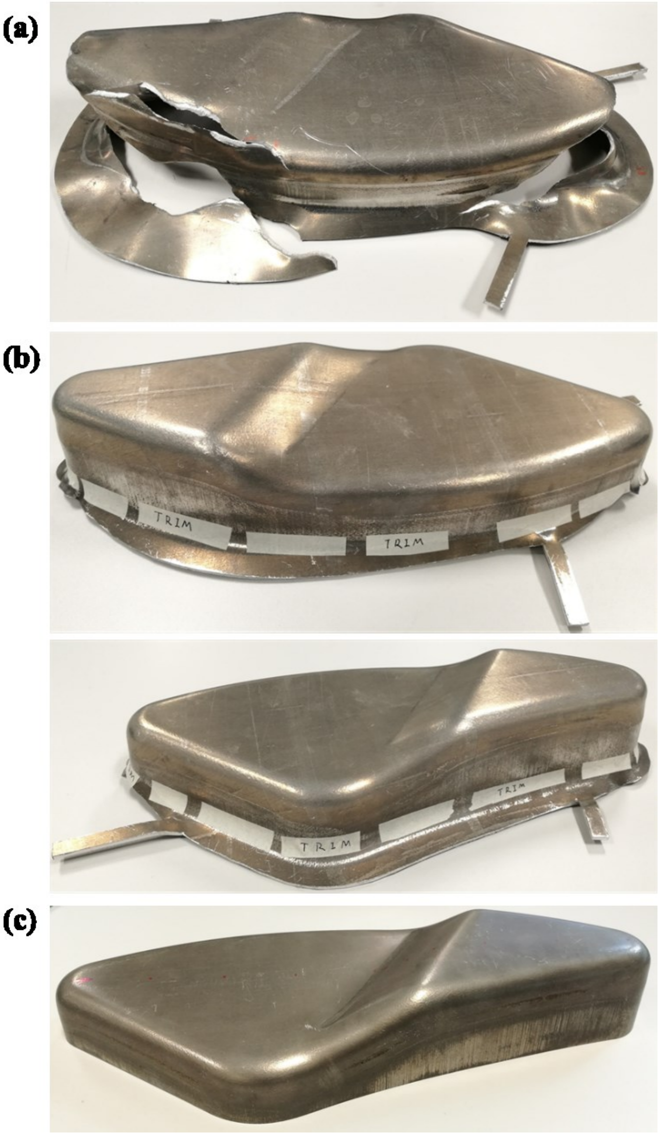

Fig. 6.25. The components formed (a) under room temperature conditions; (b) under successful forming conditions before trimming; and (c) under successful forming conditions after trimming.

6.4.6 Post-form strength and geometry

In order to verify that the demo components were successfully formed, the post-form strength, hardness and geometry of the formed components were measured. The tensile tests at room temperature and a strain rate of 0.001 s^{-1} were firstly conducted in an Instron machine. As shown in Fig. 6.26, the stress-strain curve of the post-form material was very close to that of the as-received material. The post-form proof strength at a true strain of 0.1% was increased from 79 to 90 MPa. However, the post-form ultimate tensile strength was decreased by only 8.7% from 335 to 306 MPa. The loss in the ultimate tensile strength was marginal and reasonable.

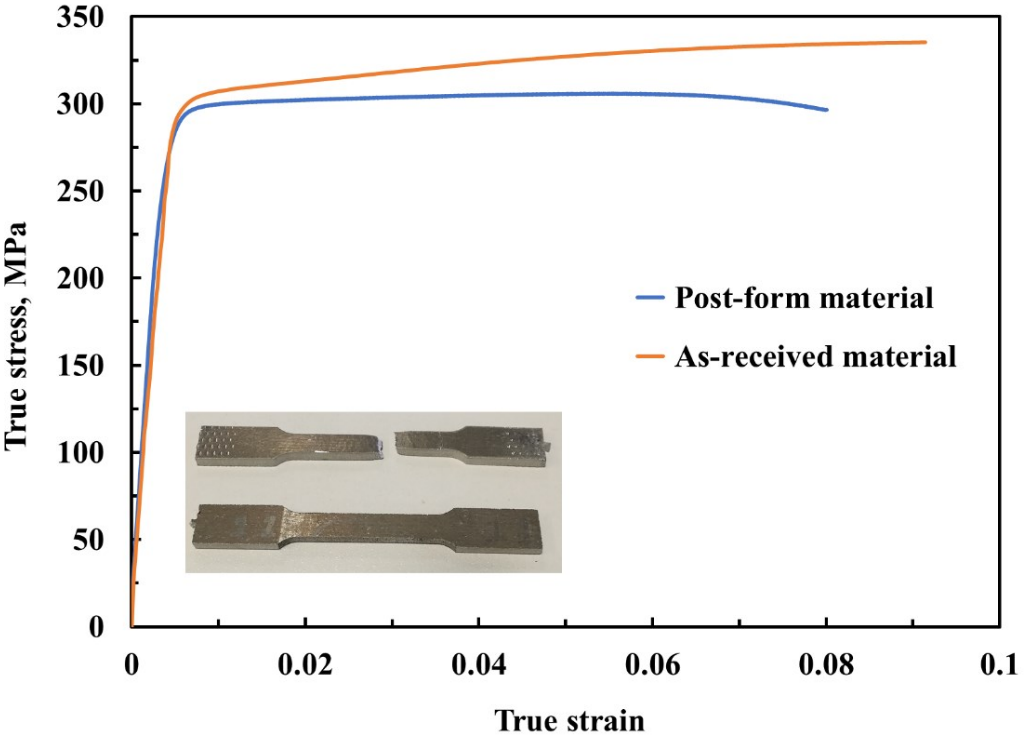

Fig. 6.26. Stress-strain curves of the post-form and as-received materials at room temperature and a strain rate of 0.001 s^{-1}.

The post-form hardness of the formed components was measured by the Equotip portable metal hardness tester Leeb. The difference in hardness between the post-form and as-received materials was within 10%, as shown in Table 6.5. The hardness of some post-form materials was even higher than that of the as-received material. The measured post-form strength and hardness indicated that the full mechanical strength of the panel component could be retained when using the HFQ forming process.

Table 6.5. Hardness of the post-form and as-received materials.

No.	As-received	1	2	3	4	5	6	7
Hardness, HV	104.3	107	106.5	97.2	109.4	102.2	98.6	105.6
Difference, %	---	2.6	2.1	-6.8	4.9	-2.0	-5.5	1.2

The post-form geometry of a trimmed component was measured using a LK G90C coordinate measurement machine. As shown in Fig 6.27, the measured evolution of the component's height agreed well with the original design, with the largest difference of 8%, indicating that the component was fully closed by the tools, and thus the geometry of the formed component achieved the desired shape.

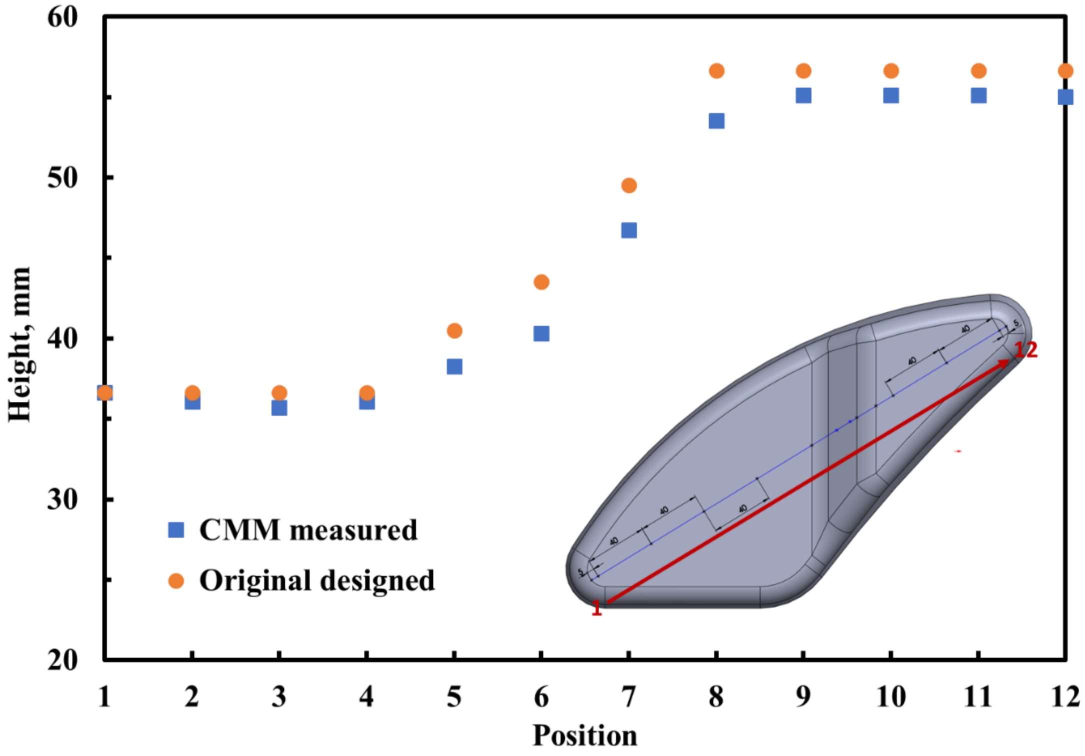

Fig. 6.27. The height evolution of the trimmed component.

6.5 Summary

The case studies in this chapter were summarised as follows:

- A 3-stage variable contact pressure determined by the data-driven approach was applied in the IHTC test to represent the abrupt contact pressure changes that occur in practical hot stamping processes. The resulting abrupt changes of the temperature evolution were accurately predicted by the FE simulation and successfully captured by IHTC-mate 2.0, verifying that it enabled the application of variable contact pressure conditions and the measurement of pressure-sensitive temperature evolutions of the specimen over extremely short time periods.

- Subsequently, hemispherical dome and B-pillar forming tests were conducted to form different aluminium alloys. The good agreements between the experimental and simulated temperature evolutions of the components being formed validated that the IHTC evolutions assigned in the FE simulations were accurately predicted by the developed mechanism-based IHTC model.
- The last cast study applied the solution Heat treatment, Forming and in-die Quenching (HFQ) process to the forming of a complex-shaped component for a locomotive vehicle. Uniaxial tension and formability tests, at various elevated temperatures and strain rates, were conducted. Advanced material predictive models were subsequently developed and calibrated using the results of these tests. An improved understanding of friction was gained by observing the evolution of the coefficient of friction during sliding under both dry and lubricated conditions, which could be used in FE simulations as well. Finally, the artificial ageing tests revealed the optimal conditions for maximising the mechanical strength of the HFQ formed component after forming. After designing and manufacturing the tooling for the demo component, further HFQ forming trials were conducted to produce the components successfully, with thinning and wrinkling minimised. After artificial ageing of the component, approximately 91% of the original material strength was retained.

Chapter 7

Conclusions

7.1 Research findings

In the present research, the IHTCs for different aluminium alloys were determined by using a dedicated test facility, and their evolutions as a function of the contact pressure, tool material, coating material, specimen thickness and lubricant were identified, quantitatively studied and modelled. These models could then be implemented in FE simulations of forming processes to simulate the temperature evolutions of the components being formed. The findings of this research are summarised below:

(1) A dedicated, novel IHTC test facility, IHTC-mate 2.0, was developed to precisely measure the temperature evolutions of a specimen and thus determine its IHTC values under different experimental conditions with high accuracy, repeatability and stability.

(2) The evolutions of the IHTC for aluminium alloys with contact pressure when using different uncoated/coated tools were found to be similar, i.e. a sharp increase followed by a plateau when the contact pressure was larger than the convergent value, which was caused by the surface of the specimen being deformed and its surface condition becoming meshed with that of the tools.

(3) The IHTC can be increased by the application of tools with higher thermal conductivities due to the heat transfer occurring at a higher rate. Tool materials with high thermal conductivities, e.g. cast-iron, can be used for the punch and die for manufacturing quenching rate sensitive materials, while materials with low thermal conductivities, e.g. H13, can be used for blankholders to prevent the temperature of a specimen from dropping significantly in the blankholding regions.

(4) In the modelling the IHTC evolution and the effect of coatings, the value of the term $\delta_c \ln(k_c/k_t)$, which is a function of the coating thickness δ_c and thermal conductivity ratio of the coating k_c to the tool (substrate) k_t, was found to determine the coating thermal

performance and its effect on the IHTC. Coatings with lower thermal conductivities, e.g. AlCrN and CrN, can be applied onto blankholders to prevent the temperature of the blank from decreasing rapidly, whilst those with high thermal conductivities, e.g. TiN, can be applied onto punches and dies to reduce tool wear and meanwhile provide high IHTC values.

(5) The IHTC increases with increasing specimen thickness due to the larger amount of internal thermal energy being stored in the thicker specimens. The concept of an engineering IHTC was therefore proposed to accurately predict the temperature evolutions of specimens with different thicknesses in FE simulations of hot stamping processes.

(6) The IHTC is increased when a graphite lubricant is applied and fills up the vacancies of the asperities at the contact interface due to the thermal conductivity of the lubricant being higher than that of air. In addition, it was also found that the IHTC decreases dramatically from a stable value when the lubricant layer thickness is lower than its convergent value.

(7) The effect of the initial blank temperature was consequently identified as a combination of two mechanisms; the effects of the material strength and thermal conductivity. The IHTC was affected by the strength of the specimen when the contact pressure was lower than its convergent value, i.e. the IHTC increased with decreasing material strength due to a larger deformation occurring at a higher initial blank temperature. However, the effect of the material strength became negligible after the convergent contact pressure, while the increasing thermal conductivity of the specimen became the dominant mechanism, further increasing the IHTC values.

(8) The developed mechanism-based IHTC model enables the prediction of the IHTC evolutions as a function of the contact pressure, tool material, coating material, specimen thickness and lubricant layer thickness, and furthermore provides an interactive method to predict the lubricant layer thickness diminution and the corresponding IHTC evolutions with sliding distance (time) at different contact pressures and sliding speeds. Meanwhile, it also enables the identification and the application of different lubricants to achieve different forming processing requirements.

(9) It was deduced that the interaction between the lubricant and the IHTC consists of three stages; namely stage I (excessive stage), in which the lubricant is applied excessively and the IHTC is plateaued, stage II (consumption stage), in which the lubricant diminishes

during sliding and the IHTC decreases rapidly, and stage III (breakdown stage), in which lubricant breakdown occurs and the IHTC is equal to its values under dry conditions.

(10) A 3-stage variable contact pressure was used in the IHTC test to represent the contact pressure with abrupt changes in the practical hot stamping processes. The abrupt changes of the temperature evolution were successfully captured by IHTC-mate 2.0 and accurately predicted by the FE simulation. In addition, the hemispherical dome and B-pillar forming tests were conducted to form different aluminium alloys. The good agreements between the experimental and simulated temperature evolutions of the components being formed validated that the IHTC evolutions assigned in the FE simulations were accurately predicted by the developed mechanism-based IHTC model.

7.2 Key contributions

1) The developed IHTC test facility is easier to be operated to determine the IHTC values with higher accuracy and repeatability.
2) The most important influential factors on the IHTC were comprehensively studied. Their interactions were found and clearly stated for the first time.
3) The novel IHTC model is able to explain the dominant heat transfer mechanisms and predict the IHTC evolutions as a function of those influential factors.
4) The hot stamping of complex-shaped components validated the determined results and the developed model, enabling their accurate application in the FE simulations.

7.3 Future work

IHTC-mate 3.0 will be applied to determine the IHTC values for materials with high solution heat treatment temperatures, e.g. titanium alloys and steels. Furthermore, tools with specific geometries will be manufactured and assembled in IHTC-mate 3.0 to realise the hot stamping of laboratory-scale components to optimise the processing window, including initial forming temperature, heating rate, soaking time and die-closing force.

In addition to the influential factors studied in the present research, the surface roughness obviously affects the IHTC, requiring further mechanism studies and quantitative investigations. Meanwhile, the developed IHTC model also has significant potential to enable the predictions of the IHTC evolutions as a function of the surface roughness, which will be characterised in future work.

The interaction between the IHTC and lubricant diminution during sliding was predicted by the developed model without experimental validations. The development of a dedicated rig is currently in process to enable relative sliding between a hot specimen and a lubricated tool at different pre-defined contact pressures. The evolutions of the temperature and lubricant layer thickness will be monitored and then compared with the predicted results to completely verify the developed interactive IHTC model.

Reference

[1] EU Commission, “Commission regulation (EU) No 582/2011 of 25 May 2011,” 2011.

[2] S. Brett, A. Spulber, S. Modi, and T. Fiorelli, “Technology roadmaps: Intelligent mobility technology, materials and manufacturing processes, and light duty vehicle propulsion,” *Cent. Automot. Res.*, 2017.

[3] C. Ungureanu, S. Das, and I. S. Jawahir, “Life-cycle cost analysis : aluminum versus steel in passenger cars,” *Miner. Met. Mater. Soc.*, pp. 11–24, 2007.

[4] R. P. Garrett, J. Lin, and T. A. Dean, “An investigation of the effects of solution heat treatment on mechanical properties for AA 6xxx alloys: Experimentation and modelling,” *Int. J. Plast.*, vol. 21, no. 8, pp. 1640–1657, 2005.

[5] B. Milkereit, O. Kessler, and C. Schick, “Recording of continuous cooling precipitation diagrams of aluminium alloys,” *Thermochim. Acta*, vol. 492, no. 1–2, pp. 73–78, 2009.

[6] O. El Fakir, L. Wang, D. Balint, J. P. Dear, J. Lin, and T. A. Dean, “Experimental and numerical studies of the solution heat treatment, forming, and in-die quenching (HFQ) process on AA5754,” *Int. J. Mach. Tools Manuf.*, vol. 87, pp. 39–48, 2014.

[7] T. Maeno, K. Mori, and R. Yachi, “Hot stamping of high-strength aluminium alloy aircraft parts using quick heating,” *CIRP Ann. - Manuf. Technol.*, vol. 66, no. 1, pp. 269–272, 2017.

[8] Q. Zhang *et al.*, “Development of the post-form strength prediction model for a highstrength 6xxx aluminium alloy with pre-existing precipitates and residual dislocations,” *Int. J. Plast.*, vol. 119, pp. 230–248, 2019.

[9] Imperial College London, “Metal forming and materials modelling.” [Online]. Available: http://www.imperial.ac.uk/metal-forming/. [Accessed: 27-Apr-2018].

[10] S. Toros, F. Ozturk, and I. Kacar, “Review of warm forming of aluminum-magnesium alloys,” *J. Mater. Process. Technol.*, vol. 207, pp. 1–12, 2008.

[11] L. Wang *et al.*, “Fast warm stamping of ultra-high strength steel sheets,” 1713741.5, 2017.

[12] G. Palumbo and L. Tricarico, “Numerical and experimental investigations on the Warm Deep Drawing process of circular aluminum alloy specimens,” *J. Mater. Process. Technol.*, vol. 184, no. 1–3, pp. 115–123, 2007.

[13] W. R. D. Wilson, S. R. Schmid, and J. Liu, “Advanced simulations for hot forging: Heat transfer model for use with the finite element method,” *J. Mater. Process. Technol.*, vol. 155–156, pp. 1912–1917, 2004.

[14] S. Bruschi, G. Buffa, A. Ducato, L. Fratini, and A. Ghiotti, “Phase evolution in hot forging of dual phase titanium alloys: Experiments and numerical analysis,” *J. Manuf. Process.*, vol. 20, pp. 382–388, 2015.

[15] C. C. Chang and A. N. Bramley, "Determination of the heat transfer coefficient at the workpiece-die interface for the forging process," *Proc. Inst. Mech. Eng.*, vol. 216, pp. 1179–1186, 2002.

[16] B. Adrian, *Heat Transfer*. New York: Chichester: Wiley, 1993.

[17] C.V. Madhusudana, *Thermal contact conductance*. New York: Springer- Verlag, 1996.

[18] B. Milkereit, N. Wanderka, C. Schick, and O. Kessler, "Continuous cooling precipitation diagrams of Al-Mg-Si alloys," *Mater. Sci. Eng. A*, vol. 550, pp. 87–96, 2012.

[19] J. Liu, A. Wang, Y. Zheng, X. Liu, J. Gandra, and K. Beamish, "Hot stamping of AA6082 tailor welded blanks for automotive applications," *Procedia Eng.*, vol. 207, pp. 729–734, 2017.

[20] E. J. F. R. Caron, K. J. Daun, and M. A. Wells, "Experimental heat transfer coefficient measurements during hot forming die quenching of boron steel at high temperatures," *Int. J. Heat Mass Transf.*, vol. 71, pp. 396–404, 2014.

[21] Y. Chang, X. Tang, K. Zhao, P. Hu, and Y. Wu, "Investigation of the factors influencing the interfacial heat transfer coefficient in hot stamping," *J. Mater. Process. Technol.*, vol. 228, pp. 25–33, 2016.

[22] L. Ying, T. Gao, M. Dai, P. Hu, and L. Shen, "Investigation of convection heat transfer coefficient of circular cross-section short pipes in hot stamping dies," *Appl. Therm. Eng.*, vol. 138, pp. 133–153, 2018.

[23] Y. Chang *et al.*, "Determination of interfacial heat transfer coefficient and analysis of influencing factors in warm forming the third-generation automotive medium-Mn steel," *Int. Commun. Heat Mass Transf.*, vol. 86, no. 2, pp. 108–116, 2017.

[24] K. Omer, C. Butcher, and M. Worswick, "Characterization of heat transfer coefficient for non-isothermal elevated temperature forming of metal alloys," *Int. J. Mater. Form.*, 2019.

[25] Q. Bai, J. Lin, L. Zhan, T. A. Dean, D. S. Balint, and Z. Zhang, "An efficient closed-form method for determining interfacial heat transfer coefficient in metal forming," *Int. J. Mach. Tools Manuf.*, vol. 56, pp. 102–110, 2012.

[26] J.-T. Yeom *et al.*, "Characterization of the interface heat transfer coefficient during non-isothermal bulk forming of Ti-6Al-4 V alloy," *Proc. Inst. Mech. Eng. Part B J. Eng. Manuf.*, vol. 225, pp. 1703–1712, 2011.

[27] G. Dour, M. Dargusch, and C. Davidson, "Recommendations and guidelines for the performance of accurate heat transfer measurements in rapid forming processes," *Int. J. Heat Mass Transf.*, vol. 49, pp. 1773–1789, 2006.

[28] K. Ji, X. Liu, O. El Fakir, J. Liu, Q. Zhang, and L. Wang, "Determination of the interfacial heat transfer coefficient in the hot stamping of AA7075," *Manuf. Rev.*, vol. 3, p. 16, 2016.

[29] B. Abdul Hay, B. Bourouga, and C. Dessain, "Thermal contact resistance estimation at the blank/tool interface: Experimental approach to simulate the blank cooling during the hot stamping process," *Int. J. Mater. Form.*, vol. 3, no. 3, pp. 147–163, 2010.

[30] N. Yukawa, Y. Nakashima, T. Ishiguro, E. Abe, T. Ishikawa, and T. Choda, "Modeling of heat transfer coefficient of oxide scale in hot forging," *Procedia Eng.*, vol. 81, pp. 492–497, 2014.

[31] K. Zhao, B. Wang, Y. Chang, X. Tang, and J. Yan, “Comparison of the methods for calculating the interfacial heat transfer coefficient in hot stamping,” *Appl. Therm. Eng.*, vol. 79, pp. 17–26, 2015.

[32] J. Mendiguren, R. Ortubay, E. S. De Argandona, and L. Galdos, “Experimental characterization of the heat transfer coefficient under different close loop controlled pressures and die temperatures,” *Appl. Therm. Eng.*, vol. 99, pp. 813–824, 2016.

[33] K. Ji, O. El Fakir, H. Gao, and L. Wang, “Determination of heat transfer coefficient for hot stamping process,” *Mater. Today Proc.*, vol. 2S, pp. S434–S439, 2015.

[34] P. Hu, L. Ying, Y. Li, and Z. Liao, “Effect of oxide scale on temperature-dependent interfacial heat transfer in hot stamping process,” *J. Mater. Process. Technol.*, vol. 213, pp. 1475–1483, 2013.

[35] Z. M. Hu, J. W. Brooks, and T. A. Dean, “The interfacial heat transfer coefficient in hot die forging of titanium alloy,” *Proc. Inst. Mech. Eng. Part C J. Mech. Eng. Sci.*, vol. 212, pp. 485–496, 1998.

[36] Y. Z. Li, C. V. Madhusudana, and E. Leonardi, “Enhancement of thermal contact conductance: effect of metallic coating,” *J. Thermophys. Heat Transf.*, vol. 14, no. 4, pp. 540–547, 2000.

[37] P. R. Burte, Y. Im, T. Altan, and S. L. Semiatin, “Measurement and analysis of heat transfer and friction during hot forging,” *J. Eng. Ind.*, vol. 112, p. 332, 1990.

[38] X. Z. Zhang, L. W. Zhang, and L. Xing, “Study of thermal interfacial resistance between TC11 / glass lubrication / K403 joint,” *Exp. Therm. Fluid Sci.*, vol. 34, no. 1, pp. 48–52, 2010.

[39] G. Ma, L. Wang, H. Gao, J. Zhang, and T. Reddyhoff, “The friction coefficient evolution of a TiN coated contact during sliding wear,” *Appl. Surf. Sci.*, vol. 345, pp. 109–115, 2015.

[40] T. S. Kumar, S. B. Prabu, G. Manivasagam, and K. A. Padmanabhan, “Comparison of TiAlN, AlCrN, and AlCrN/TiAlN coatings for cutting-tool applications,” *Int. J. Miner. Metall. Mater.*, vol. 21, no. 8, pp. 796–805, 2014.

[41] Y. Y. Chang, D. Y. Wang, and C. Y. Hung, “Structural and mechanical properties of nanolayered TiAlN/CrN coatings synthesized by a cathodic arc deposition process,” *Surf. Coatings Technol.*, vol. 200, no. 5–6, pp. 1702–1708, 2005.

[42] M. K. Samani *et al.*, “Thermal conductivity of titanium nitride/titanium aluminum nitride multilayer coatings deposited by lateral rotating cathode arc,” *Thin Solid Films*, vol. 578, pp. 133–138, 2015.

[43] J. Liu *et al.*, “Transition of failure mode in hot stamping of AA6082 tailor welded blanks,” *J. Mater. Process. Technol.*, vol. 257, pp. 33–44, 2018.

[44] E. Caron, K. J. Daun, and M. A. Wells, “Experimental characterization of heat transfer coefficients during hot forming die quenching of boron steel,” *Metall. Mater. Trans. B Process Metall. Mater. Process. Sci.*, vol. 44, pp. 332–343, 2013.

[45] A. Vadiraj, M. Kamaraj, and V. S. Sreenivasan, “Wear and friction behavior of alloyed gray cast iron with solid lubricants under boundary lubrication,” *Tribol. Int.*, vol. 44, no. 10, pp. 1168–1173, 2011.

[46] A. D. Foster, M. S. Mohamed, J. Lin, T. A. Dean, and S. Kensington, “An investigation of lubricant and heat transfer for a sheet aluminium heat, form-quench (HFQ) process,”

in *12th International Conference on Metal Forming*, 2008, pp. 113–120.

[47] V. K. Jain, “Determination of heat transfer coefficient for forging applications,” *J. Mater. Shap. Technol.*, vol. 8, pp. 193–202, 1990.

[48] Z. Zhu, L.-W. Zhang, Q.-K. Wu, and S.-D. Gu, “An experimental investigation of thermal contact conductance of Hastelloy C-276 based on steady-state heat flux method,” *Int. Commun. Heat Mass Transf.*, vol. 41, pp. 63–67, 2013.

[49] M. Xu, R. Ling, Z. Zhang, and J. Xie, “Study on interfacial heat transfer behavior of TA15 titanium alloy and die materials,” *Int. J. Heat Mass Transf.*, vol. 108, pp. 1573–1578, 2017.

[50] T. N. Çetinkale and M. Fishenden, “Thermal conductance of metal surfaces in contact,” *Proc. Int. Conf. Heat Transf. Inst. Mech. Eng.*, pp. 271–275, 1951.

[51] M. G. Cooper, B. B. Mikic, and M. M. Yovanovich, “Thermal contact conductance,” *Int J. Heat Mass Transf.*, vol. 153, pp. 317–23, 1969.

[52] J. P. Shlykov, E. A. Ganin, and S. N. Tsarevskiy, “Thermal contact resistance,” *M. Energy*, p. 328, 1977.

[53] V. W. Antonetti and M. M. Yovanovich, “Using metallic coatings to enhance thermal contact conductance of electronic packages,” *Heat Transf. Eng.*, vol. 9, no. 3, pp. 85–92, 1988.

[54] V. W. Antonetti and M. M. Yovanovich, “Enhancement of thermal contact conductance by metallic coatings: theory and experiment.,” *J. Heat Transfer*, vol. 107, no. 3, pp. 513–519, 1985.

[55] G. P. Peterson and L. S. Fletcher, “Measurement of the Thermal Contact Conductance and Thermal-Conductivity of Anodized Aluminum Coatings,” *J. Heat Transf. Asme*, vol. 112, no. 3, pp. 579–585, 1990.

[56] T. K. Kang, G. P. Peterson, and L. S. Fletcher, “Effect of metallic coatings on the thermal contact conductance of turned surfaces,” *J. Heat Transfer*, vol. 112, no. 4, pp. 864–871, 1990.

[57] M. P. Pereira, W. Yan, and B. F. Rolfe, “Sliding distance, contact pressure and wear in sheet metal stamping,” *Wear*, vol. 268, no. 11–12, pp. 1275–1284, 2010.

[58] A. Wang, O. El Fakir, J. Liu, Q. Zhang, Y. Zheng, and L. Wang, “Multi-objective finite element simulations of a sheet metal-forming process via a cloud-based platform,” *Int. J. Adv. Manuf. Technol.*, vol. 100, pp. 2753–2765, 2018.

[59] A. Wang, Y. Zheng, J. Liu, O. El Fakir, M. Masen, and L. Wang, “Knowledge Based Cloud FE simulation - data-driven material characterization guidelines for the hot stamping of aluminium alloys,” in *Journal of Physics: Conference Series*, 2016, vol. 734, p. 032042.

[60] “Smart forming technology platform,” 2018. [Online]. Available: http://techtiqdemo.co.uk/demonodes/smart-forming/. [Accessed: 05-Feb-2019].

[61] P. Bosetti, S. Bruschi, T. Stoehr, J. Lechler, and M. Merklein, “Interlaboratory comparison for heat transfer coefficient identification in hot stamping of high strength steels,” *Int. J. Mater. Form.*, vol. 3, pp. 817–820, 2010.

[62] “Gleeble Systems,” *Dynamic Systems Inc.*, 2015. [Online]. Available: http://gleeble.com/products/products-overview.html.

[63] "MatWeb material property data," 2011. [Online]. Available: http://www.matweb.com/index.aspx. [Accessed: 05-Jun-2018].

[64] Schuler, "Tool material properties," 2017.

[65] Schuler, "Coating technology," 2017.

[66] MatWeb. LLC., "Aluminum 7075-T6." [Online]. Available: http://www.matweb.com/search/DataSheet.aspx?MatGUID=4f19a42be94546b686bbf43f79c51b7d&ckck=1. [Accessed: 20-Apr-2019].

[67] Austria Metal AG, "Material certificate," 2016.

[68] B. Johnson, "Residual stress reduction during quenching of wrought 7075 aluminum alloy," Worchster Polytechnic Institute, 2004.

[69] M. S. Mohamed, A. D. Foster, J. Lin, D. S. Balint, and T. A. Dean, "Investigation of deformation and failure features in hot stamping of AA6082: Experimentation and modelling," *Int. J. Mach. Tools Manuf.*, vol. 53, pp. 27–38, 2012.

[70] H. Karbasian and A. E. Tekkaya, "A review on hot stamping," *J. Mater. Process. Technol.*, vol. 210, pp. 2103–2118, 2010.

[71] B. B. Mikic, "Thermal contact conductance; theoretical considerations," *Int. J. Heat Mass Transf.*, vol. 17, pp. 205–214, 1974.

[72] B. Buchner, M. Buchner, and B. Buchmayr, "Determination of the real contact area for numerical simulation," *Tribol. Int.*, vol. 42, pp. 897–901, 2009.

[73] B. Bhushan, *Surface roughness analysis and measurement techniques*. CRC Press LLC, 2001.

[74] G. E. Totten and D. S. Mackenzie, "Handbook of aluminum. Vol. 1. Physical metallurgy and processes," New York: Marcel Dekker, Inc., 2003, pp. 895–907.

[75] N. Saunders, "The modelling of stable and metastable phase formation in multi-component al-alloys," *Mater. Forum*, vol. 28, pp. 96–106, 2004.

[76] M. A. Masen and M. B. de Rooij, "Abrasive wear between rough surfaces in deep drawing," *Wear*, vol. 256, no. 6, pp. 639–646, 2004.

[77] S.-W. Lo and T.-S. Yang, "A new mechanism of asperity flattening in sliding contact—The role of tool elastic microwedge," *J. Tribol.*, vol. 125, no. 4, p. 713, 2003.

[78] H. Li, L. He, G. Zhao, and L. Zhang, "Constitutive relationships of hot stamping boron steel B1500HS based on the modified Arrhenius and Johnson-Cook model," *Mater. Sci. Eng. A*, vol. 580, pp. 330–348, 2013.

[79] Y. Hu, L. Wang, D. J. Politis, and M. A. Masen, "Development of an interactive friction model for the prediction of lubricant breakdown behaviour during sliding wear," *Tribol. Int.*, vol. 110, pp. 370–377, 2017.

[80] A. Begelinger and A. W. J. De Gee, "Failure of thin film lubrication - A detailed study of the lubricant film breakdown mechanism," *Wear*, vol. 77, no. 1, pp. 57–63, 1982.

[81] D. Dowson and T. L. Whomes, "Paper 8: Side-leakage factors for a rigid cylinder lubricated by an isoviscous fluid," *Proc. Inst. Mech. Eng. Conf. Proc.*, vol. 181, pp. 165–176, 1966.

[82] W. R. D. Wilson, T.-C. Hsu, and X.-B. Huang, "A realistic friction model for computer simulation of sheet metal forming processes," *J. Eng. Ind.*, vol. 117, no. 2, pp. 202–209,

1995.

[83] R. Larsson and O. Andersson, “Lubricant thermal conductivity and heat capacity under high pressure,” *Proc. Inst. Mech. Eng. Part J J. Eng. Tribol.*, vol. 214, no. 4, pp. 337–342, 2000.

[84] V. Norouzifard and M. Hamedi, “Experimental determination of the tool–chip thermal contact conductance in machining process,” *Int. J. Mach. Tools Manuf.*, vol. 84, pp. 45–57, 2014.

[85] I. Valls and A. Hamasaiid, “High thermal conductivity and high wear resistance tool steels for cost-effective hot stamping tools,” *J. Phys. Conf. Ser.*, vol. 896, p. 012046, 2017.

[86] O. El Fakir, L. Wang, D. Balint, J. P. Dear, and J. Lin, “Predicting effect of temperature, strain rate and strain path changes on forming limit of lightweight sheet metal alloys,” *Procedia Eng.*, vol. 81, pp. 736–741, 2014.

[87] J. Lin and T. A. Dean, “Modelling of microstructure evolution in hot forming using unified constitutive equations,” *J. Mater. Process. Technol.*, vol. 167, no. 2–3, pp. 354–362, 2005.

[88] B. M. Dariani, G. H. Liaghat, and M. Gerdooei, “Experimental investigation of sheet metal formability under various strain rates,” *Proc. Inst. Mech. Eng. Part B J. Eng. Manuf.*, vol. 223, no. 6, pp. 703–712, 2009.

[89] F. Abu-Farha, R. Verma, and L. G. Hector, “High temperature composite forming limit diagrams of four magnesium AZ31B sheets obtained by pneumatic stretching,” *J. Mater. Process. Technol.*, vol. 212, no. 6, pp. 1414–1429, 2012.

[90] Z. Marciniak and K. Kuczyński, “Limit strains in the processes of stretch-forming sheet metal,” *Int. J. Mech. Sci.*, vol. 9, no. 9, pp. 609–620, 1967.

[91] A. Barata da Rocha, A. D. Santos, P. Teixeira, and M. C. Butuc, “Analysis of plastic flow localization under strain paths changes and its coupling with finite element simulation in sheet metal forming,” *J. Mater. Process. Technol.*, vol. 209, no. 11, pp. 5097–5109, 2009.

[92] A. Graf and W. F. Hosford, “Calculations of forming limit diagrams,” *Metall. Trans. A*, vol. 21, pp. 87–94, 1990.

[93] J. Cao, H. Yao, A. Karafillis, and M. C. Boyce, “Prediction of localized thinning in sheet metal using a general anisotropic yield criterion,” *Int. J. Plast.*, vol. 16, no. 9, pp. 1105–1129, 2000.

[94] E. Gelinck and D. J. Schipper, “Calculation of Stribeck curves for line contacts,” *Tribol. Int.*, vol. 33, pp. 175–181, 2000.